# Turbulent transport in a multi-ion drift fluid model

Thesis submitted for the degree of
Doctor of Philosophy

Department of Physics
Technical University of Denmark

Technical University of Denmark

Aslak Sindbjerg Poulsen

# Turbulent transport in a multi-ion drift fluid model

Supervisor: Prof. Volker Naulin

Co-supervisors: Prof. Jens Juul Rasmussen
Dr Matthias Wiesenberger
*Technical University of Denmark*

Academician Jiangang Li
*Hefei Institute of Physical Science*

Examiners: Dr hab. Roman Zagorski
*National Centre for Nuclear Research, Poland*
Dr Patrick Tamain
*Institute for Magnetic Fusion Research, CEA, France*

Chairman: Dr.techn. Mirko Salewski
*Technical University of Denmark*

Submitted to the Technical University of Denmark
on February 7<sup>rd</sup> 2020.

# Abstract

To meet the future energy demands of the World, fusion energy has been proposed as a possible energy solution as it provides clean, sustainable and reliable means of energy production. However, a working fusion power plant has yet to be realised. Currently, the most promising reactor design is a magnetic confinement device to called a Tokamak. One of the problems this concept is facing is turbulent transport of particles and energy from the region of closed magnetic field lines to that of open magnetic field lines and onto plasma-facing materials of the reactor. Future reactors inherently contain multiple ion species due to fusing of deuterium and tritium. Consequently, understanding the influence of the multiple ion species on turbulent transport is of utmost importance.

In this work, a drift fluid model is derived that consistently incorporates multiple ion species and collisional interactions between species. The model is derived from the Boltzmann equation and uses the Zhdanov closure to obtain a closed set of equations from which the drift fluid expansion can be performed.

The model equations are solved numerically using the discontinuous Galerkin method and the numerical implementation of the equations is discussed in detail.

With the numerical implementation of the equations, two topics are studied, seeded plasma blobs and turbulent transport. For the seeded blobs, the influence of different ion mixes on the propagation of the blobs is examined through scaling of the blob velocity. The mixes that are studied are deuterium-tritium mixtures as well as deuterium and doubly ionized helium mixes. Finally, fully developed turbulence is investigated. In particular, the impact of multiple ion species on the particle and energy fluxes across the last closed flux surface is examined. For the blobs, it was found that when the mixture is of deuterium and tritium, the velocity of the radial motion decreases as the amount of tritium increases. From the deuterium helium simulations, it is found that the higher mass of the helium is counteracted by being doubly charged and results in similar blob velocities for deuterium and helium dominated blobs respectively. For the turbulent transport the results indicated that the increased presence of tritium yielded higher flux of particles and energy from the edge to the scrape-off-layer.

**Keywords:** Isotopes, Multiple ion species, Drift-fluid equations, Plasma blobs, Plasma turbulence, Numerical modelling

# Resumé

For at imødekomme fremtidens energiforbrug er fusionsenergi blevet foreslået som en mulig løsning, der kan levere ren, vedvarende og pålidelig energi. Desværre er et fungerende fusionskraftværk endnu ikke realiseret. Det, for øjeblikket, mest lovende reaktor design er et magnetisk indeslutningapparet kaldet en Tokamak. Et af problemerne konceptet står over for, er transporten af partikler og energi fra regionen med lukkede magnetfeltsliner til regionen med åbne magnetfeltslineir og videre ud på reaktorens vægge. Fremtidige kraftværker vil i sagens natur indeholde flere forskellige ion isotoper, da fusionen sker mellem deuterium og tritium. Som følge heraf, er det yderst vigtig at forstå indflydelsen af flere ion isotoper på den turbulente transport.

I denne afhandling udledes en drift-fluid model, der konsistent inkorporerer flere ion isotoper og deres indbyrdes kollisionelle interactioner. Model er udledt fra Botlzmannligningen og bruger Zhdanov lukning til at opnå et lukket sæt af ligninger, hvorfra drift-fluid udvidelsen kan udføres.

Modelligningerne løses numerisk ved brug den ikke-kontinuerte Galerkin metode, og implementeringen af ligningerne diskuteres i detaljer.

Med den numeriske implementering af ligningerne, undersøges to emner; plasma blobs og turbulent transport. For plasma blobs undersøges effekten af forskellige ion blandinger på udbredelsen gennem en skalering af blobhastigheden. Blandingerne der undersøges er deuterium tritium samt deuterium og dobbelt ioniseret helium blandinger. Til sidst undersøges fuldt udviklet turbulent transport. Her undersøges ion blandingens inflydelse på partikel- og energifluxen over sidste lukkede feltlinie. For blobene findes det, at for deuterium tritium blandinger falder den radiale hastighed, når mængden af tritium øges i forhold til deuterium. For deuterium helium simuleringerne findes det, at effekten af den større masse af helium bliver modvirket af dobbeltioniseringen. Dette resulterer i lignende hastigheder for hhv. deuterium og tritium dominerede blobs. For den turbulente transport indikerer resultaterne, at en øget tilstedeværelse af tritium fører til højere partikel- og energifluxer fra de lukkede til de åben feltlinier.

# Acknowledgements

Throughout the last three years, I have had the pleasure of performing my PhD studies in the dedicated Plasma Physics and Fusion Energy group at DTU.

I would like to thank my supervisors Prof. Volker Naulin and Prof. Jiangang Li for providing me with the guidance and opportunity to perform my PhD studies in what I believe to be one of the most interesting branches of physics. In addition, I would like to thank Prof. Jens Juul Rasmussen and Dr Matthias Wiesenberger for engaging in many discussions and showing patience with my endless stream of questions on the physics and numerical methods necessary to carry out this work.

During my studies, I had the pleasure of working in Hefei, China at the Chinese Academy of Science Institute of Plasma Physics. Here I was warmly welcomed by Xiang Liu, Wu Xingquan and Dongrui Zhang who introduced me to Chinese culture and took me into their group. This I truly appreciate.

Many laughs, ups and downs have been shared with my office mates, Michael Løiten Magnussen, Alexander Thrysøe, Jeppe Miki Busk Olsen, Galina Avdeeva, Mads Givskov Senstius and Raul Gerru. Likewise, many good moments have been shared with Andrea Tancetti, Raheesty Devi Nem, Henrik Järleblad, Heidi Espinoza, Axel Larsen and Birgitte Madsen who was also in China alongside me and made the trip much more enjoyable. All of you deserve many thanks for making the past three years as good as they have been.

I would also like to thank Volker Naulin, Matthias Wiesenberger, Jens Juul Rasmussen and Alexander Thrysøe for proofreading and commenting on the manuscript in the final hour.

Lastly, I would like to thank friends and family for always supporting me throughout this period of my life. In particular, I would like to thank my girlfriend Mia Høj Mathiasson for her everlasting support and encouragement throughout this work and for taking care of our two daughters when I had to work late or go abroad for long periods of time. With you, no mountain is too high.

# Contents

# Chapter 1

# Introdution and Motivation

No field of study exists without some form of motivation. This can be either of pure interest for the sake of knowledge or from a more practical point of view in order to achieve some goal. Naturally neither are mutually exclusive and often one leads to the other. Plasma physics has for a long time been the subject of study, in regards to understanding the heavens above us. However, with the dawn of the nuclear age, the use of plasma physics for energy-related topics, both destructive and peaceful, has become relevant.

## 1.1 A practical application - Fusion Energy

Harnessing energy from all kinds of sources is arguably the foundation of mankind. From the first bonfire, millions of years ago [1] to prepare food and stay warm, over harnessing natures kinematics for labour such as wind- and watermills to mill flour and saw wood to today's production of electricity in modern adaptions of the aforementioned such as power plants. Much of the power produced today is done with the burning of fossil fuels either for electricity production, the transport sector or heating. A byproduct of the consumption of fossil fuels is the release $CO_2$ into the atmosphere. This gas is quite good a trapping long wavelength radiation emanating from the earth, but not as good at keeping out short wavelength radiation coming from the Sun. The continued release of $C0_2$ upsets earths energy balance and will eventually lead to a global warming of the planet until a new balance is found. While $CO_2$ free renewable energy sources are gaining traction, they still suffer from not being an on-demand power source. A backup system is needed in the cases when the wind is not blowing and the sun not shining. One such future backup or main energy source could be fusion energy.

### 1.1.1 Fusion Energy

In the early 20'th century it was discovered that when combining light particles into the mass of the resulting particles was less than the sum of the individual masses before the combination, or *fusion*, of the particles. From Einstein's theory of relativity, it was inferred that the small loss of mass could result in large amounts of energy being released. The fusion of light protons into helium is what powers the sun. However, this fusion process has a very small reaction cross-section [2] and so is not viable for energy production on Earth. The most achievable reaction is the deuterium-tritium (DT) reaction which occurs as:

$$D + T \rightarrow {}^{4}He(3.5MeV) + n(14.1MeV) \tag{1.1}$$

This means that for each reaction there is a total of $17.6MeV$ released. The energy of the alpha particles goes in to heating the DT mix to fusion temperatures (and later to the divortors) while neutron energy is radiated onto the vessel walls. If it assume that, e.g., 80% of the energy is captured and used for power production, then the reaction of 0.4g of deuterium and 0.6g tritium (a total of 1g of fuel) produces around the same amount of energy as burning 4-6 tonnes of crude oil or roughly 6-8 tonnes of coal. With such an energy density, a fusion power plant at 1000MW would need approximately 250kg of fuel for a years operation which is significantly less than the 2-3 million tons of coal needed to produce the same output. Deuterium can be obtained directly from seawater while tritium can be bred by irradiating lithium with neutrons which is common in the earth crust [3]. It is estimated that with proven resources of deuterium and lithium, the worlds energy demand could be met for the next six million years based on current estimates [4].

## 1.2 Plasma Physics and the Tokamak

Producing and harnessing the energy of fusion reactions requires a machine capable of doing so. Naturally, with reaction temperatures well into the millions of degrees Kelvin, creating a box that can contain it poses quite a problem, especially since all known materials have far lower melting points. At such high temperatures, the fuel attains the fourth state of matter, namely the form of a plasma. Many concepts to build a container have been considered throughout the history of fusion energy research, with the most prominent being a magnetic confinement device called a tokamak[5]. To understand how this works and confines particles one first needs to know how charged particles behave under the influence of electromagnetic fields.

### 1.2.1 The Tokamak

From first-year electromagnetism, a typical physics student learns how a charged particle, under the influence of electric and magnetic fields, behaves. So if the particle has a charge $q$, the force acting upon the particle is then the Lorentz force:

$$\frac{d}{dt} m_0 \boldsymbol{v} = q\left(\boldsymbol{E} + \boldsymbol{v} \times \boldsymbol{B}\right) \tag{1.2}$$

Where $m_0$ is the rest mass, $\boldsymbol{v}$ is the velocity of the particle, $\boldsymbol{E}$ and $\boldsymbol{B}$ are the electric and magnetic field respectively. The electromagnetic forces are known to be much stronger than the gravitational forces meaning the latter can be neglected. Also, nuclear forces are not considered here. From the Lorentz force equation, it is evident from the cross product of the velocity with the magnetic field, that a charged particle in a magnetic field will gyrate around and along the magnetic field lines as long as the magnetic field is present. Hence the particle is confined in the perpendicular direction. The parallel component is unaffected by the magnetic field and the particle would keep going along the magnetic field assuming it has a non-zero parallel component. This is, of course, no problem if the container with the magnetic field is infinitely long which is of course not possible. A ring, however, can in a sense be considered an infinite loop and so taking a finite solenoid and bending it into a doughnut shape creates a torus-shaped magnetic chamber. While ingenious, it suffers from one major problem. Due to the bending, the wires on the inside of the torus are more closely wound than the ones of the outer part of the torus. This creates an inhomogeneous magnetic field of the form

$$B(r) \propto \frac{1}{r} \tag{1.3}$$

where $r$ is the radial distance from the centre of the torus. The radius of the gyrating motion, commonly referred to as the Larmor radius or gyro-radius, is given as:

$$\rho = \frac{\sqrt{Tm}}{qB} \tag{1.4}$$

where $m$ is the mass of the particle, $T$ is the temperature and $q$ the charge. Upon inspection, it is evident the size of the radius depends on the position of the particle in the inhomogeneous magnetic field, and in fact in the course one gyration, the particle will experience a changing magnetic field. The leads to the particle drifting since it travels a longer distance on the low field part of the trajectory compared to the high field side. Such a drift is called the *gradient-B drift.* Due to the charge dependence in the Lorentz force, two particles of opposite charge will drift in opposite directions, giving rise to an electric field. When a gyrating particle experiences an electric field, the particle will be accelerated when moving along the field and decelerated when moving against the field or vice versa, depending on the charge of the particle. This means that at one part of the trajectory perpendicular to the electric field the particle will move faster than at the opposite part of the trajectory perpendicular. Consequently, a second drift occurs, namely the $\boldsymbol{E} \times \boldsymbol{B}$, or electric drift. The direction of the drift is independent of the charge and so the whole plasma will move radially outward, making this configuration inherently unstable. The solution to this problem is then to make the particles go back into the inner part of the reactor when they are on the outer. This is done by adding a magnetic field in the poloidal (around the torus cross-section) which together with the toroidal creates a twisted magnetic field. The poloidal field is produced by ramping up a current in a large central solenoid that induces a toroidal current in the plasma which then creates a poloidal magnetic field. The tokamak was initially conceived in the early '50s in the Soviet Union along with the construction of the first tokamak, the T-1 in 58[6]. Since then, a large number of tokamaks have been constructed, but a tokamak that produces surplus energy has yet to be made. The record for highest fusion gain was by the Joint European Torus with a Q-factor of 0.67[7]. Early versions of the tokamak used a circular cross-section of the torus while modern ones have a triangular-shaped (or D-shaped) cross-section. A schematic of a modern machine is shown in Fig. 1.1 along with a cross-section of the vessel.

Here it is seen that the magnetic field lines can be divided into two regions: one with closed field lines ending on themselves and one with open field lines ending on the divertor plates[1]. The closed region is often referred to as the confined region while the open region is the scrape-off-layer (SOL) where particles are carried towards to divertors and disposed of. The size of the tokamak can be expressed in terms of the radius of the torus called the major radius $R$, and the radius of the tube called the minor radius $r$. From these quantities, it is common to define the parameter known as the aspect ratio $R/r$.

---

[1] Naturally the field lines are not actually open since magnetic monopoles do not exist. The use of 'open' is to emphasize the interaction of the field lines with the vessel materials.

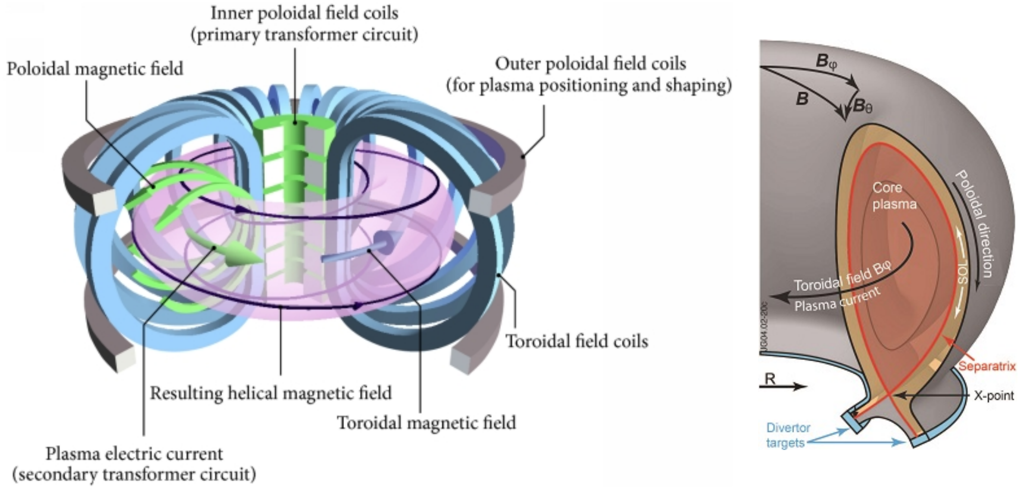

Figure 1.1: Left: Schematic of a tokamak (taken from [8]). Right: Cross-section of tokamak (taken from [9]).

### 1.2.2 Plasma Physics

In the preceding section, the principle of the tokamak was outlaid with an offset in how a particle acts in a magnetic field. Having a single particle within a machine is not quite enough to make fusion happen but instead, a large number of particles will be present. The presence of a large number of interacting particles is a fundamental problem in physics and the question is now how to deal with such a system. In the field of plasma physics, the particles are characterised by the fact that they emanate and interact with electric and magnetic fields. This is the main focus of Chapter 2. What can now be done is to try to get an idea of the kind of plasma that can be expected within a tokamak. Whether it is a relativistic, a quantum mechanical or a collision dominated system presents a path for studying the system. The density and temperature of the plasma can be used to classify the different plasma regimes and one such diagram is shown in Fig. 1.2. At above $10^9 K$ the plasma begins to exhibit relativistic behaviour.

### 1.2.3 Turbulent transport

While the concept of the tokamak is very clear, bringing the machine to fruition in terms of producing surplus energy has yet to be realised. One problem is the high losses of particles and energy from the edge and the core into the SOL. In classical theory, transport is carried through the diffusion

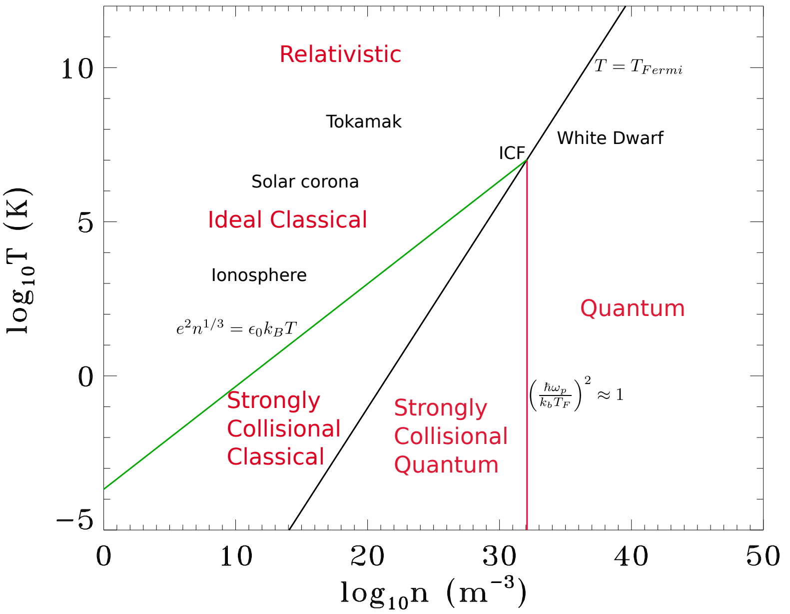

Figure 1.2: Classification of plasmas according to temperature and density where $\omega_p = (e^2 n / m\epsilon_0)^{1/2}$ is the plasma frequency. Figure modified from [10].

.

of particles and energy, but it is insufficient in describing the full loss. It was later found that a correction to the classical transport due to the geometrical shape of the magnetic field was needed which resulted in the theory of neoclassical transport [11]. This too, however, is insufficient in describing the full loss and one also needs to consider what is commonly referred to as anomalous transport [12]. Consider a plasma with fluctuations in the pressure. Under such circumstances the mechanism described earlier in regards to the instability of a purely toroidal magnetic field confinement presents itself again. A fluctuation, or perturbation, in the pressure, will experience a polarising drift due to the grad-B drift (and curvature drift) and consequently drift radially outward due to the resulting $\boldsymbol{E} \times \boldsymbol{B}$-drift. These perturbations drifting outward stretch along the magnetic field lines and are commonly referred to as filaments or blobs. It has been found that these blobs contribute significantly to the transport from the edge to the SOL [13]–[15]. Blobs entering the SOL can reach either the divertors or wall possibly causing degradation of the vessel materials as well as releasing impurities into the plasma. The introduction of impurities to the main plasma can cause severe cooling of the plasma, preventing fusion conditions from being reached. For these reasons it is important to ensure material travels to the divertors and do so in a steady stream. In order to alleviate this problem, it is necessary to obtain a better knowledge of their characteristics. The approach for doing so in this work is through numerical simulations using conditions similar to those of a typical medium-sized tokamak such as the Experimental Advanced Superconducting Tokamak (EAST) or Asdex Upgrade. The plasma which is found in the edge and scrape-off-layer of a tokamak usually reaches temperatures up to some $100eV$ and densities up to $10^{19}m^{-3}$. From the plasma classification scheme presented in Fig. 1.2 it is clear that this kind of plasma is a typical classical plasma where collisions are not dominant. Luckily, this also means there is no need to worry about relativistic and quantum effects. This is will be very useful in the next chapter when deriving a model well suited for studying transport in this region.

## 1.3 Structure of Thesis

The focus of this work is the study of edge/SOL dynamics in which much of the work done in this topic has only involved pure single species plasma [16]–[20] or some effective particle representing a mix of species [21]–[23]. In this work, a true multi-species model is employed to study the effects the ion mixture has on turbulent transport. This is studied in a 2D slab configuration perpendicular to the magnetic field emulating a small region in the outboard midplane of the tokamak, where the bulk of the transport occurs. As mentioned, the main plasma in energy-producing machines will be composed of a mix of deuterium, tritium and helium as well as some amount of impurities. In this regard, it is known that the transport at the LCFS is significantly influenced by the ion composition of the plasma and in particular that the transition from a low confinement mode to high confinement mode, commonly known as the LH-transition, is affected by the mix [24]. Furthermore, at EAST temperatures have reached a record 100 million degree Kelvin [25] and pulses over 100 second [26] though not at the same time. This has been achieved in part by the use of lithium in SOL which has been shown to reduce transport across the LCFS [27]. The thesis is divided into three main chapters, a theory, a numerical and a result chapter which together contain the bulk of the work. Finally, the results from each chapter are summarised in a conclusion chapter.

In Chapter 2 a theoretical model is derived based on the Boltzmann equation by taking moments to obtain expressions for macroscopic parameters such as density velocity and temperature. From this, a drift fluid model, the multi-ion Hot Edge-Sol Electrostatic or MIHESEL model, is derived similarly to HESEL [17] along with appropriate approximation in order to obtain a model suitable for numerical implementation.

The numerical implementation is discussed in Chapter 3. This includes the choice of the discontinuous Galerkin method as the numerical method, which forms the basis of the FELTOR library [28], as well as an overview of the library. Furthermore, additions to the library in the form of a fully implicit multistep backward differentiation formula (BDF) method along with a non-linear solver to solve the non-linear system equation in the BDF method are discussed.

In Chapter 4, the model is used to study the effects of isotopes on plasma dynamics. The first part of the chapter is concerned with seeded blobs which are studied using various mixtures of D and T, which are included in the first submitted paper, and a mixture of deuterium and doubly ionized helium. Blobs are a widely studied subject in regards to transport the simple setting can provide much insight into the overall transport seen in a tokamak. The second part of the chapter examines edge profiles and the turbulence that evolves in this region. Here each blob in itself is not of much interest as it was for seeded blobs, rather it is the statistical behaviour of the edge transport that is of interest.

Finally, in Chapter 5, a summary of results and discussion hereof are presented. Furthermore, an overview of future improvements and research topics are discussed.

# Chapter 2

# Theory - from micro to macro

The goal of physics is often to make quantitative statements about the evolution of a system of interest, in our case, a collection of charged particles called a plasma. In principle, we know most of the first principles, such as Maxwell's equations, Schroedinger's equation, the relativistic laws of motion etc, and therefore all answers for our question should be right there for the taking. However, this is rarely the case and intricate knowledge of the system you wish to describe is needed to get any useful answers. It is for example overly complicated for us to bring in quantum mechanics when wanting the calculate the trajectory of a ping pong ball. In short, using a sledgehammer to crack a nut is a bit extreme.

## 2.1 From the micro to the macro

In the introduction, the outline of plasma physics was roughly sketched as a collection of charged particles interacting through and with electric and magnetic fields. In the setting of a tokamak plasma located at the edge/SOL region, it was argued that the plasma could be considered using classical theory with a small number of collisions.

### 2.1.1 Fluid moment equations

To work with the system, two components are needed. One that describes the kinematics of the particles and one that describes the evolution of the electric and magnetic fields. For the latter it is known from first-year electromagnetism that the classical evolution of these fields is governed by Maxwell's equations [29]:

$$\nabla \cdot \boldsymbol{D} = qn \tag{2.1}$$

$$\nabla \cdot \boldsymbol{B} = 0 \tag{2.2}$$

$$\nabla \times \boldsymbol{E} = -\frac{\partial}{\partial t}\boldsymbol{B} \tag{2.3}$$

$$\nabla \times \boldsymbol{H} = \boldsymbol{J} + \frac{\partial}{\partial t}\boldsymbol{D} \tag{2.4}$$

where $\boldsymbol{D} = \epsilon_0 \boldsymbol{E} + \boldsymbol{P}$ is the electric displacement field with polarisation density $\boldsymbol{P}$, $\boldsymbol{H} = \mu_0^{-1}\boldsymbol{B} - \boldsymbol{M}$ is the magnetic field with strength with magnetisation field $\boldsymbol{M}$, $\epsilon_0$ and $\mu_0$ are the vacuum permittivity and permeability and $\boldsymbol{J}$ is the current density. These equations contain all classical electromagnetic phenomena and are a bid overkill for the purpose of studying the edge/SOL region. In this case, it is common to employ the electrostatic approximation and assume the magnetic field perturbations to be negligible [30]. The result is that the electric field can be expressed in terms of an electric potential $\phi$

$$\boldsymbol{E} = \nabla\phi \tag{2.5}$$

This lessens the complexity of the problem quite substantially. Returning to the problem of solving for $10^{19}$ individual particles using the Lorentz force equation is of course not possible either analytically or numerically. Analytically, a three-body problem remains unsolved for an arbitrary system, and n-body problems even more so. Numerically such problems are solvable in discrete space, but tracking each particle quickly becomes unmanageable as each particle interacts with each other creating an $N^2$ problem, where $N$ is the number of particles[1]. What can be exploited on the other hand is that when the number of particles in the system is enormous the individual behaviour of each particle is of little interest. Instead it is more interesting to study the collective behaviour of the system and seek a way to describe this. The method going forward is a statistical approach where the plasma can be described through a single-particle distribution function $f_s(\boldsymbol{x}, \boldsymbol{v}, t)$ defined as the number density of particles of species $s$ within phase space volume element dxdv at a time $t$ [32]. The variables $\boldsymbol{x}$ and $\boldsymbol{v}$ are considered independent. From this distribution function, global parameters such as

---

[1] Less expensive particle approaches exits such as particle-in-cell, but even this is very computationally demanding for such a big system of particles[31].

particle density $n_s$, velocity and pressure $p_s = n_s T_s$ can be obtained:

$$n_s(\boldsymbol{x},t) = \int f_s(\boldsymbol{x},\boldsymbol{v},t)\mathrm{d}\boldsymbol{v} \tag{2.6}$$

$$n_s\boldsymbol{u}_s(\boldsymbol{x},t) = \int \boldsymbol{v} f_s(\boldsymbol{x},\boldsymbol{v},t)\mathrm{d}\boldsymbol{v} \tag{2.7}$$

$$\frac{3}{2}p_s(\boldsymbol{x},t) = \frac{3}{2}n_s(\boldsymbol{x},t)T_s(\boldsymbol{x},t) = \int (\boldsymbol{v}-\boldsymbol{u}_s)^2 f_s(\boldsymbol{x},\boldsymbol{v},t)\mathrm{d}\boldsymbol{v} \tag{2.8}$$

To find how these evolve in time, the evolution of the distribution function $f_s$ must be know. In this regard the procedure is very similar to what is used to solve typical gas problems. In quick terms, the process is to assume all particles to be identical and integrate out other particles and find an equation for a single particle, but since all particles are identical, it can be used to find global variables. If the plasma is relatively dilute the single particle distribution function is governed by the Boltzmann equation, which can be derived from the many particle Liouville equation. A thorough derivation can be found in, e.g, [32], [33]. The Boltzmann equation is then given as

$$\left(\frac{\partial}{\partial t} + \boldsymbol{v}\cdot\frac{\partial}{\partial \boldsymbol{x}} + \frac{\boldsymbol{F}_s}{m_s}\cdot\frac{\partial}{\partial \boldsymbol{v}}\right) f_s = \left(\frac{\partial}{\partial t} f_s\right)_{col} + \left(\frac{\partial}{\partial t} f_s\right)_{src} \tag{2.9}$$

where $\boldsymbol{F}_s(\boldsymbol{x},t)$ is the force acting on the species $s$. In the case of a plasma, this will typically be comprised of the electric and magnetic field and as such the force is given by the Lorentz force stated in Eq. (1.2). The right hand side represents the changes to the distribution function due binary collisions between particles of all species as well as some source/sink term. The source/sink term could be in either added/removed energy, momentum, particles or all three and the source terms thus accounts for inelastic collisions such as ionization of neutral particles. In the case where the collisions are negligible in comparison to long range Coulomb interactions and there are no sources, the right hand side is set to zero giving the Vlasov equation. In principle, with the correct collision operator (and neglecting non-binary collisions) the plasma system is fully described by the combination of the kinetic Boltzmann equation (2.9) and Maxwell's equations with all length and time scales resolved. However, this system of equations is practically impossible to solve. The aim is therefore to reduce the complexity of the system to illuminate the relevant physics. Since turbulent transport occurring in the edge and scrape-off-layer is of interest in this work, the system of equations will be tuned such that this behaviour is highlighted without being overly complicated. Before doing so we take a slight pause to consider the collision operator.

**Collision Operator** The origin of the Boltzmann equation is in the study of dilute gasses. In such a case the collisions between particles are that of two hard spheres. This means that the interaction is an 'instantaneous' short-range scattering of the two colliding particles that had no prior interaction. Since particles don't interact, except for during collisions, this also means that limiting the interactions to two-particle interactions, as opposed to multi-particle collisions, is a very good approximation. In a plasma physics this is not the case as charged particles interact through long range (Coulomb) interactions and so it is not only long term collisions while also being many body interactions. Luckily however, two particle interactions are effectively screened by the Debye length and so it is only relevant when the distance between the two is smaller than the Debye length while the many body interactions are dealt with in the collective electric field. Considering this the collisions can be assumed similar to that of dilute gasses and as such described as binary collisions. In that case the operator is bilinear in form:

$$\left(\frac{\partial}{\partial t} f_s\right)_{col} = C_s(f_s) = \sum_{s'} C_{ss'}(f_s, f_{s'}) \tag{2.10}$$

A commonly used collision operator is the Landau collisions operator given as [34]–[36]

$$C_{ss'}(f_s, f_{s'}) = \frac{2\pi}{m_s}\left(\frac{q_s q_{s'}}{4\pi\epsilon_0}\right)^2 \ln\Lambda_{ss'} \nabla_{\boldsymbol{v}} \cdot$$
$$\left[\int \mathrm{d}\boldsymbol{v}' \boldsymbol{U} \cdot \left(\frac{f_{s'}(\boldsymbol{v}')}{m_s} \nabla_{\boldsymbol{v}} f_s(v) - \frac{f_s(\boldsymbol{v})}{m_{s'}} \nabla_{\boldsymbol{v}'} f_{s'}(\boldsymbol{v}')\right)\right] \tag{2.11}$$

where $\ln\Lambda_{ss'}$ is the Coulomb logarithm and

$$\Lambda_{ss'} = \frac{12\pi\epsilon_0}{|q_s q_{s'}|} \frac{\mu_{ss'}}{\gamma_{ss'}} \lambda_d. \tag{2.12}$$

Here $\mu_{ss'} = m_s m_{s'}/(m_s + m_{s'})$ is the reduced mass, $\gamma_{ss'} = \gamma_s \gamma_{s'}/(\gamma_s + \gamma_{s'})$ with $\gamma_s = m_s/T_s$ and the Debye length for the plasma is given as:

$$\lambda_d = \left(\sum_s \frac{n_s q_s^2}{\epsilon_0 T_s}\right)^{-\frac{1}{2}} \tag{2.13}$$

Lastly, the rank two tensor $\boldsymbol{U}$ is expressed in terms of $\boldsymbol{u} = \boldsymbol{v} - \boldsymbol{v}'$ as:

$$\boldsymbol{U} = \frac{u^2 \boldsymbol{I} - \boldsymbol{u}\boldsymbol{u}}{u^3} \tag{2.14}$$

As stated earlier, the desire is for an equation that describes the evolution of the system which involves some form of averaged quantities, $n_s$, $\boldsymbol{u}_s$ and $T_s$. From the Boltzmann equation, this can be done by taking moments in velocity space. The simple straight forward approach would be to multiply the equation with $k\boldsymbol{v} \otimes \boldsymbol{v}...$, where k is some factor like the mass $m$ and the outer product is performed $i$ times with $i$ being the number of the moment. Performing this operation would result in a large system of equations. E.g. the second moment would result in six individual equations etc. Instead, expressions for the variables given in Eqs. (2.6) to (2.8) are sought. The process is very similar to the naive approach stated above. This is rather fundamental and can be found in a variety of textbooks [34], [37].

**Density** The zeroth order moment with $k = 1$ describing the evolution of the density is:

$$\int \mathrm{d}\boldsymbol{v}\frac{\partial}{\partial t}f_s + \boldsymbol{v}\cdot\nabla_{\boldsymbol{x}} f_s + \frac{\boldsymbol{F}_s}{m_s}\cdot\frac{\partial}{\partial \boldsymbol{v}} f_s = \int \mathrm{d}\boldsymbol{v}\left[\left(\frac{\partial f_s}{\partial t}\right)_{col} + \left(\frac{\partial f_s}{\partial t}\right)_{Src}\right] \tag{2.15}$$

The first term is already given from 2.6 by using that the time derivative and the integral variables are independent and hence the operations can be interchanged giving $\partial_t n_s$. Using the independence of $\boldsymbol{x}$ and $\boldsymbol{v}$ the second term is found to be:

$$\begin{aligned}\int \mathrm{d}\boldsymbol{v}\boldsymbol{v}\cdot\nabla_{\boldsymbol{x}} f_s &= \int \mathrm{d}\boldsymbol{v}\nabla_{\boldsymbol{x}}\cdot(\boldsymbol{v}f_s) - \cancelto{0}{\int \mathrm{d}\boldsymbol{v} f_s \nabla_{\boldsymbol{x}}\cdot\boldsymbol{v}} \\ &= \nabla_{\boldsymbol{x}}\cdot\int \mathrm{d}\boldsymbol{v}\boldsymbol{v}f_s = \nabla_{\boldsymbol{x}}\cdot(n_s\boldsymbol{u}_s) \end{aligned} \tag{2.16}$$

When using the Lorentz force in the last term in the left hand side gives:

$$\int \mathrm{d}\boldsymbol{v}\boldsymbol{F}_s\cdot\nabla_{\boldsymbol{v}} f_s = \int \mathrm{d}\boldsymbol{v}\nabla_{\boldsymbol{v}}\cdot(\boldsymbol{F}_s f_s) = 0 \tag{2.17}$$

For the collisional part of the right hand side it can be shown using the divergence theorem and that $f_s \to 0$ as $v \to \pm\infty$ that the Landau collision operator conserves particles:

$$\int \mathrm{d}\boldsymbol{v}C_s = 0 \tag{2.18}$$

This is a rather fundamental requirement as it would be very unphysical to have a species creating particles simply by interaction with itself or another species. Naturally, this excludes ionizing collisions which fall under the source term. For the source term, there is no a priori knowledge, as it depends on the physical setup, and so it is simply defined as:

$$\int \mathrm{d}\boldsymbol{v} S_s \equiv S_{s,n} \tag{2.19}$$

$$\tag{2.20}$$

The source might be by, e.g., injection of particles or by ionization of neutral atoms. Adding it all together gives the fluid continuity equation for the evolution of the density of species $s$:

$$\frac{\partial}{\partial t} n_s + \nabla_{\boldsymbol{x}} \cdot (n_s \boldsymbol{u}_s) = S_{s,n} \tag{2.21}$$

**Fluid velocity** For the next moment, with $i = 1$ and $k = m_s$, where $m_s$ is the species particle mass, one has:

$$\begin{aligned} &m_s \int \mathrm{d}\boldsymbol{v}\boldsymbol{v} \left[ \frac{\partial}{\partial t} f_s + \boldsymbol{v} \cdot \nabla_{\boldsymbol{x}} f_s + \frac{\boldsymbol{F}_s}{m_s} \cdot \nabla_{\boldsymbol{v}} f_s \right] \\ &= m_s \int \mathrm{d}\boldsymbol{v} \left[ \left( \boldsymbol{v} \frac{\partial f_s}{\partial t} \right)_{col} + \left( \boldsymbol{v} \frac{\partial f_s}{\partial t} \right)_{Src} \right]. \end{aligned} \tag{2.22}$$

For the first term the same procedure used for the zeroth order moment to exchange integral and time derivative is used here. Using (2.7) one arrives at:

$$m_s \int \mathrm{d}\boldsymbol{v}\boldsymbol{v} \frac{\partial}{\partial t} f_s = m_s \frac{\partial}{\partial t} (n_s \boldsymbol{u}_s) \tag{2.23}$$

For the next term one starts with employing the product rule and spatial independence of the velocity variable to write:

$$\begin{aligned} &m_s \int \mathrm{d}\boldsymbol{v} \left( \nabla_{\boldsymbol{x}} \cdot (\boldsymbol{v}\boldsymbol{v} f_s) - \cancelto{0}{f_s \nabla_{\boldsymbol{x}} \cdot (\boldsymbol{v}\boldsymbol{v})} \right) \\ &= m_s \nabla_{\boldsymbol{x}} \cdot \int \mathrm{d}\boldsymbol{v} \, (\boldsymbol{v}\boldsymbol{v} f_s) \equiv m_s \nabla_{\boldsymbol{x}} \cdot \langle \boldsymbol{v}\boldsymbol{v} \rangle_{f_s} \equiv \nabla_{\boldsymbol{x}} \cdot \boldsymbol{\Pi}_s \end{aligned} \tag{2.24}$$

This is just the next order moment which at the moment there is little information about. What can be seen is that since $\boldsymbol{v}$ is a rank one tensor (vector) the outer product $\boldsymbol{v}\boldsymbol{v}$ results in a rank two tensor meaning $\boldsymbol{\Pi}_s$ is a rank two tensor. What to do is to write the velocities as the sum of the species average fluid velocity and the thermal velocity in that rest frame $\boldsymbol{v} = \boldsymbol{u}_s + \boldsymbol{w}_s$. Inserting this into 2.24 yields:

$$\begin{aligned} \langle \boldsymbol{v}\boldsymbol{v} \rangle_{f_s} &= \langle (\boldsymbol{u}_s + \boldsymbol{w}_s)(\boldsymbol{u}_s + \boldsymbol{w}_s) \rangle_{f_s} \\ &= \langle \boldsymbol{u}_s \boldsymbol{u}_s \rangle_{f_s} + \langle \boldsymbol{w}_s \boldsymbol{w}_s \rangle_{f_s} + \langle \boldsymbol{u}_s \boldsymbol{w}_s \rangle_{f_s} + \langle \boldsymbol{w}_s \boldsymbol{u}_s \rangle_{f_s} \end{aligned} \tag{2.25}$$

Since $\boldsymbol{u}_s$ is already the mean velocity its one gets $\langle \boldsymbol{u}_s\boldsymbol{u}_s\rangle_{f_s} = \boldsymbol{u}_s\boldsymbol{u}_s\langle 1\rangle_{f_s} = \boldsymbol{u}_s\boldsymbol{u}_s n_s$. Similar one gets $\langle \boldsymbol{u}_s\boldsymbol{w}_s\rangle_{f_s} = \boldsymbol{u}_s\langle \boldsymbol{w}_s\rangle_{f_s} = 0$ which is also the case for $\langle \boldsymbol{w}_s\boldsymbol{u}_s\rangle_{f_s} = 0$ where it was used that $\langle \boldsymbol{w}_s\rangle_{f_s} = \langle \boldsymbol{v}\rangle_{f_s} - \langle \boldsymbol{u}_s\rangle_{f_s} = n_s(\boldsymbol{u}_s - \boldsymbol{u}_s) = 0$. The remaining term $\langle \boldsymbol{w}_s\boldsymbol{w}_s\rangle_{f_s}$ gives the pressure tensor $\boldsymbol{P}_s$ which as mentioned is a rank two tensor. The trace of the pressure tensor gives the scalar pressure:

$$p_s = \frac{1}{3}\mathrm{Tr}(\boldsymbol{P}_s) = \frac{1}{3}m_s\int \mathrm{d}\boldsymbol{v} w_s^2 f_s \tag{2.26}$$

In total one arrives at:

$$\begin{aligned}\nabla_{\boldsymbol{x}}\cdot\boldsymbol{\Pi}_s &= \nabla_{\boldsymbol{x}}\cdot\boldsymbol{P}_s + \nabla_{\boldsymbol{x}}\cdot(m_s n_s\boldsymbol{u}_s\boldsymbol{u}_s)\\ &= \nabla_{\boldsymbol{x}}\cdot\boldsymbol{\pi}_s + \nabla_{\boldsymbol{x}}\cdot\boldsymbol{I}p_s + \nabla_{\boldsymbol{x}}\cdot(m_s n_s\boldsymbol{u}_s\boldsymbol{u}_s)\end{aligned} \tag{2.27}$$

Where $\boldsymbol{I}$ is the identity tensor and $\boldsymbol{\pi}$ is the viscous stress tensor which at the moment there is no information about. Lastly for the left hand side the force term remains:

$$\begin{aligned}m_s\int \mathrm{d}\boldsymbol{v}\frac{q_s}{m_s}\boldsymbol{v}(\boldsymbol{E}+\boldsymbol{v}\times\boldsymbol{B})\cdot\nabla_{\boldsymbol{v}}f_s &= \int \mathrm{d}\boldsymbol{v}q_s\nabla_{\boldsymbol{v}}\cdot(\boldsymbol{v}(\boldsymbol{E}+\boldsymbol{v}\times\boldsymbol{B})f_s)\\ -\int \mathrm{d}\boldsymbol{v}q_s\boldsymbol{v}\nabla_{\boldsymbol{v}}\cdot(\boldsymbol{E}+\boldsymbol{v}\times\boldsymbol{B})f_s &- \int \mathrm{d}\boldsymbol{v}q_s\nabla_{\boldsymbol{v}}\cdot(\boldsymbol{v})(\boldsymbol{E}+\boldsymbol{v}\times\boldsymbol{B})f_s\\ &= -m_s q_s n_s(\boldsymbol{E}+\boldsymbol{u}_s\times\boldsymbol{B})\end{aligned} \tag{2.28}$$

The first term after the first equality term vanishes as it is a surface term (Gauss' Theorem). The second term vanishes since $\boldsymbol{E}$ is independent of velocity and $\boldsymbol{v}\times\boldsymbol{B}$ is perpendicular to $\nabla_{\boldsymbol{v}}$. This leaves only the last term giving the above result. For the collisional part of the right hand side the lowest order expression for the moment of the collision operator can be found by using the bi-linearity expressed in Eq. (2.10). Expanding the distribution function around a Maxwellian [2] $f_s^0$ it can be shown that the frictional resistive force of a species $s'$ acting on a species $s$ yields [34], [38]:

$$\boldsymbol{R}_{s'\to s,u} = -m_s n_s \nu_{s'\to s}(\boldsymbol{u}_s - \boldsymbol{u}_{s'}) \tag{2.29}$$

where the collision frequency is given by [34], [39]:

$$\nu_{s'\to\alpha} = \frac{2^{1/2} n_{s'} Z_s^2 Z_{s'}^2 e^4 \ln\Lambda_{ss'}\left(1+\frac{m_s}{m_{s'}}\right)}{12\pi^{3/2}\epsilon_0^2 m_s^2\left(\frac{T_s}{m_s}+\frac{T_{s'}}{m_{s'}}\right)^{3/2}}. \tag{2.30}$$

---

[2] The Maxwellian is expanded to first order in the relative mean velocity of the two species assuming $|\boldsymbol{u}_s - \boldsymbol{u}_{s'}| \ll v_s$.

Rewriting $m_s\nabla_{\boldsymbol{x}}\cdot(n_s\boldsymbol{u}_s\boldsymbol{u}_s)=m_sn_s\boldsymbol{u}_s\nabla_{\boldsymbol{x}}\cdot\boldsymbol{u}_s+m_s\boldsymbol{u}_s\nabla_{\boldsymbol{x}}\cdot(n_s\boldsymbol{u}_s)$ and invoking the continuity equation (Eq. (2.21)), the density can be pulled out of the time derivative in the momentum equation giving the fluid velocity equation as

$$\begin{aligned} m_sn_s\left(\frac{\partial}{\partial t}+\boldsymbol{u}_s\cdot\nabla_{\boldsymbol{x}}\right)\boldsymbol{u}_s= \\ -\nabla_{\boldsymbol{x}}\cdot\boldsymbol{\pi}_s-\nabla_{\boldsymbol{x}}p_s+q_sn_s\left(\boldsymbol{E}+\boldsymbol{u}_s\times\boldsymbol{B}\right)+\boldsymbol{R}_s+\boldsymbol{S}_\Gamma-m_s\boldsymbol{u}_sS_{n,s} \end{aligned} \tag{2.31}$$

Where the $\boldsymbol{S}_\Gamma$ is the momentum source defined as

$$\boldsymbol{S}_\Gamma\equiv m_s\int \mathrm{d}\boldsymbol{v}\left(\boldsymbol{v}\frac{\partial f_s}{\partial t}\right)_{Src} \tag{2.32}$$

**Pressure** For the next moment, an expression for the pressure evolution is sought. The starting procedure is by taking $k=\frac{1}{2}m_s$, multiplying with $v^2$ and performing the integration. This moment corresponds to the energy equation for the total energy $1/2mn\boldsymbol{u}^2$, but with the help of the continuity and velocity equation, an equation for the pressure can be obtained. It should be noted that one could have taken the 'full' moment and multiplied by $\boldsymbol{v}\otimes\boldsymbol{v}$ which would give an equation for the full rank two pressure tensor, which also encompasses the scalar pressure. The reason for not doing so is that it would result in an additional six equations per species when the scalar pressure is what is interesting. For the first term in the Boltzmann equation the procedure is very similar to the other two moments:

$$\begin{aligned} &\frac{1}{2}\int \mathrm{d}\boldsymbol{v}v_s^2\frac{\partial}{\partial t}f_s \\ =&\frac{1}{2}\int \mathrm{d}\boldsymbol{v}w_s^2\frac{\partial}{\partial t}f_s+\frac{1}{2}\int \mathrm{d}\boldsymbol{v}u_s^2\frac{\partial}{\partial t}f_s=\frac{\partial}{\partial t}\left(\frac{3}{2}p_s+\frac{1}{2}m_sn_su_s^2\right) \end{aligned} \tag{2.33}$$

This is the change in the total energy of the species. Here it was used that $\boldsymbol{v}=\boldsymbol{u}_s+\boldsymbol{w}_s$ giving $v^2=(\boldsymbol{u}_s+\boldsymbol{w}_s)\cdot(\boldsymbol{u}_s+\boldsymbol{w}_s)=u_s^2+w_s^2+2\boldsymbol{u}_s\cdot\boldsymbol{w}_s$ and that $\langle\boldsymbol{u}_s\cdot w_s\rangle=\boldsymbol{u}_s\cdot\langle w_s\rangle=0$. Also to get the pressure, Eq. (2.8) was used. Using the same again and that $\nabla_{\boldsymbol{x}}v=0$ the next terms can be written as:

$$\begin{aligned} \frac{1}{2}m_s\int \mathrm{d}\boldsymbol{v}v^2\boldsymbol{v}\nabla_{\boldsymbol{x}}f_s=&\frac{1}{2}m_s\int \mathrm{d}\boldsymbol{v}\nabla_{\boldsymbol{x}}\cdot\left(v^2\boldsymbol{v}f_s\right)-\cancelto{0}{\nabla_{\boldsymbol{x}}\cdot\left(v^2\boldsymbol{v}\right)f_s} \\ =&\frac{1}{2}m_s\int \mathrm{d}\boldsymbol{v}\nabla_{\boldsymbol{x}}\cdot\left(\left(u_s^2+w_s^2+2\boldsymbol{u}_s\cdot\boldsymbol{w}_s\right)(\boldsymbol{u}_s+\boldsymbol{w}_s)f_s\right) \\ =&\frac{1}{2}m_s\nabla_{\boldsymbol{x}}\Bigg(\left\langle w_s^2\boldsymbol{w}_s\right\rangle+u_s^2\cancelto{0}{\langle\boldsymbol{w}_s\rangle}+2\left\langle(\boldsymbol{w}_s\cdot\boldsymbol{u}_s)\boldsymbol{w}_s\right\rangle \\ &+\left\langle w_s^2\right\rangle\boldsymbol{u}_s+u_s^2\boldsymbol{u}_s\langle 1\rangle+2\cancelto{0}{\left\langle(\boldsymbol{w}_s\cdot\boldsymbol{u}_s)\boldsymbol{u}_s\right\rangle}\Bigg) \end{aligned} \tag{2.34}$$

The first non-zero term on the last line involves the next order moment and is the heat flux $\boldsymbol{q}_s = \frac{1}{2} m_s \left\langle w_s^2 \boldsymbol{w}_s \right\rangle$. For the second non-zero term, the integral is independent of $\boldsymbol{u}_s$ and so the term is proportional to the pressure tensor introduced earlier. The third non-zero term is recognised as the scalar pressure $\left\langle w_s^2 \right\rangle = p_s$ and the last term is $\langle 1 \rangle = n_s$. Putting it together gives:

$$\frac{1}{2} m_s \int \mathrm{d}\boldsymbol{v} v^2 \boldsymbol{v} \nabla_{\boldsymbol{x}} f_s = \nabla_{\boldsymbol{x}} \cdot \left( \boldsymbol{q}_s + \boldsymbol{P}_s \cdot \boldsymbol{u}_s + \frac{3}{2} \boldsymbol{u}_s p_s + \frac{1}{2} u_s^2 \boldsymbol{u}_s n_s \right) \tag{2.35}$$

Using the same approach as for the momentum equation, the last term on the left hand side of the Boltzmann equation yields:

$$\begin{aligned} &\frac{1}{2} m_s \int \mathrm{d}\boldsymbol{v} v^2 \frac{q_s}{m_s} (\boldsymbol{E} + \boldsymbol{v} \times \boldsymbol{B}) \cdot \nabla_{\boldsymbol{v}} f_s \\ = \frac{1}{2} \int \mathrm{d}\boldsymbol{v} \nabla_{\boldsymbol{v}} \cdot \left( v^2 q_s (\boldsymbol{E} + \boldsymbol{v} \times \boldsymbol{B}) f_s \right) - &\nabla_{\boldsymbol{v}} \cdot \left( v^2 q_s (\boldsymbol{E} + \boldsymbol{v} \times \boldsymbol{B}) \right) f_s \\ = -\frac{1}{2} \int \mathrm{d}\boldsymbol{v} 2\boldsymbol{v} \cdot q_s (\boldsymbol{E} + \boldsymbol{v} \times \boldsymbol{B}) f_s + &v^2 \nabla_{\boldsymbol{v}} \cdot q_s (\boldsymbol{E} + \boldsymbol{v} \times \boldsymbol{B}) f_s \\ = -\int \mathrm{d}\boldsymbol{v} \boldsymbol{v} \cdot q_s (\boldsymbol{E} + \boldsymbol{v} \times \boldsymbol{B}) f_s = -&\int \mathrm{d}\boldsymbol{v} \boldsymbol{v} \cdot \boldsymbol{E} f_s = -n_s \boldsymbol{u}_s \cdot \boldsymbol{E} \end{aligned} \tag{2.36}$$

Similar to the calculation for the resistive force in Eq. (2.29), the right hand side can be evaluated to give:

$$Q_s = \sum_{s'} \frac{1}{m} \int \mathrm{d}\boldsymbol{v} v^2 C(f_s, f_{s'}) = \sum_{s'} \frac{3 n_s m_s \nu_{s' \to s} (T_s - T_{s'})}{m_s + m_{s'}} \tag{2.37}$$

This is be recognised as the collisional thermal energy exchange between a species $s$ and all other species $s'$. Upon inspection it can be seen that $Q_{s' \to s} = Q_{s \to s'}$ as would be expected in terms of energy conservation. Adding it all together yields:

$$\begin{aligned} &\frac{\partial}{\partial t} \left( \frac{3}{2} m_s p_s + \frac{1}{2} m_s n_s u_s^2 \right) \\ &+ \nabla_{\boldsymbol{x}} \cdot \left( \boldsymbol{q}_s + \boldsymbol{P}_s \cdot \boldsymbol{u}_s + \frac{3}{2} \boldsymbol{u}_s p_s + \frac{1}{2} u_s^2 \boldsymbol{u}_s n_s \right) \\ &- n_s \boldsymbol{u}_s \cdot \boldsymbol{E} = Q_s + S_{E,s} \end{aligned} \tag{2.38}$$

The source term was simply defined as

$$S_{E,s} \equiv m_s \int \mathrm{d}\boldsymbol{v} v^2 \left( \frac{\partial f_s}{\partial t} \right)_{Src} \tag{2.39}$$

and its exact composition will be discussed later in Section 2.1.3. This is the total energy moment equation. Using the continuity equation multiplied by

$1/2m_s u_s^2$ and taking the dot product of the momentum equation with $\boldsymbol{u}_s$ the pressure momentum equation can then be obtained:

$$\begin{aligned} &\frac{3}{2}\frac{\partial}{\partial t}p_s + \frac{3}{2}\nabla_{\boldsymbol{x}} \cdot (p_s \boldsymbol{u}_s) + \boldsymbol{P}_s : \nabla_{\boldsymbol{x}} \boldsymbol{u}_s + \nabla_{\boldsymbol{x}} \cdot \boldsymbol{q}_s \\ &= Q_s - \boldsymbol{u} \cdot \boldsymbol{R}_s + S_{E,s} - \boldsymbol{u}_s \cdot \boldsymbol{S}_{\Gamma,s} + \frac{1}{2} m_s u_s^2 S_{n,s} \end{aligned} \tag{2.40}$$

To summarise, an equation for the density, fluid velocity and pressure are now at hand. These are however not usable at this time as it has been noticed that each equation required part of the next order moment. One could go on and find further moments and hope for the best, however the $\boldsymbol{v} \cdot \nabla_{\boldsymbol{x}} f_s$ terms naturally introduces the need for the next moment. This means one would have to go on for infinity, which is of course quite time consuming. In the end this leaves undefined quantities, namely the viscous stress tensor $\boldsymbol{\pi}_s$ and the heat flux $\boldsymbol{q}_s$. Due to these unknown parameters, the density, velocity and pressure equations are for the moment unsolvable. Therefore, some method is needed to *close* the system of equations such that they can actually be solved.

**Closure** The method of closing the system is referred to as a *closure scheme*. An example of a simple closure scheme could be by simply fixing the fluid velocity and only solve the continuity/density equation. This kind of closure is termed a truncation scheme [35], [40]. For the equations derived above, one could also set the pressure tensor and heat flux to zero, this would, however, leave out interesting physical behaviour. For this reason, this closure scheme is not used. Another closure approach is the so-called asymptotic scheme in which scales of the kinetic equations are exploited to arrive at equations for the higher moments. The downside of this approach is a vastly increased amount of complexity and mathematical rigour. One such approach, and in plasma physics the most common approach, is to use the so-called Chapman-Enskog procedure which expands the distribution function in some small parameter $\varepsilon$ [41]:

$$f_s = f_{s,0} + \varepsilon f_{s,1} + \varepsilon^2 f_{s,2} + \dots \tag{2.41}$$

This is done under the assumption that the mean free path $\lambda$ and the mean gyro-radius $\rho_s$ is much smaller than characteristic parallel and perpendicular length scales, $L_\parallel$ and $L_\perp$ respectively

$$\epsilon \approx \frac{\lambda}{L_\parallel} \sim \frac{\rho_s}{L_\perp} \tag{2.42}$$

This method is used by Braginskii [37] to derive the famous Braginskii fluid equations for density, fluid velocity and temperature. It is these equations that form the basis of many single species drift fluid models, including the HESEL equations. However, it turns out that when multiple ion species are introduced the Chapman-Enskog procedure can become mathematically overly complicated. Luckily there is another procedure which has proven useful when dealing with multiple species. This method is the Grad's moment method [42] and is employed to form the Zhdanov closure which will be used here[34]]. The main idea is to expand the distribution function in terms of orthogonal tensorial Hermite polynomials as

$$f_s = f_{s,0} \sum_n \sum_m \frac{(2m+1)!(m+n)!}{n!(m!)^2(2n+2m+1)!} a_s^{mn} H^{mn} \left( \boldsymbol{w}_s \sqrt{\frac{m_s}{T_s}} \right) \tag{2.43}$$

where $H^{mn}$ is the Hermite polynomials expressed in terms of Sonine polynomials $S$ and irreducible harmonic polynomials $P$:

$$H^{mn} = (-2)^{-1} n! S^n_{m+1/2} \left( \left( c_s \sqrt{\frac{m_s}{T_s}} \right)^2 /2 \right) P^{(m)} \left( \boldsymbol{w}_s \sqrt{\frac{m_s}{T_s}} \right) \tag{2.44}$$

and the coefficients $a_{mn}$ are given by:

$$n_s a_s^{mn} = \int \mathrm{d}\boldsymbol{c} H^{mn} f_s \tag{2.45}$$

Doing ample amounts of algebra and arithmetic will yield explicit expressions for the polynomials and consequently the coefficients. Once an explicit form of the distribution function is found, the unknown moments can be evaluated and in this case give expressions for the pressure tensor and heat flux in terms of density, fluid velocity and temperature to make a closed system of equations. A thorough discussion on the difference between the Chapman-Enskog closure scheme and Grad's moment method can be found in [33], [34], [43], [44].

### 2.1.2 Zhdanov Closure

The polynomials and coefficients discussed can be calculated explicitly to form the distribution function $f_s$ and consequently evaluate the pressure tensor and heat flux. The lowest moment approximation is the 13-moment approximations which include all interesting physically meaningful quantities. Unfortunately, this does not provide sufficient accuracy [33], [34]. The next moment approximation is the 21-moment approximation which gives a good accuracy while going higher the 29-moment approximation does not yield much increase in accuracy [33]. In the 21-moment closure used by Zhdanov, the complexity of solving the system is such that the ion temperatures are assumed nearly equal $|T_\alpha - T_\beta| \ll T_\alpha$. This limitation does not apply to electrons as the mass is much smaller. For future reference, the subscripts $\alpha$ and $\beta$ will be used for ions while the subscripts $s$ and $s'$ denote both ions and electrons. It should be noted that for the single ion species case, the Chapman-Enskog procedure and Grad's method yield identical results and so the results obtained by Braginskii, which correspond to the 21-moment method, are identical to the Zhdanov closure for a single ion species [34]. Furthermore, while cumbersome, the Chapman-Enskog method has been applied to multispecies as seen in [38], [45], albeit without expressions for the viscous stress tensor. The two remaining terms in the moment equations, disregarding the source terms, are the heat flux $\boldsymbol{q}_s$ and the viscous stress tensor $\boldsymbol{\pi}_s$. This closure has also been used for other fluid models to model impurity transport in the edge [46], [47].

**Heat flux** To lowest order in the expansion of the distribution function, where collisions are neglected, the ion and electron heat fluxes are given as:

$$\boldsymbol{q}_{\times,\alpha} = \frac{5}{2}\frac{p_\alpha}{q_\alpha B}\boldsymbol{b}\times\nabla T_\alpha, \tag{2.46}$$

$$\boldsymbol{q}_{\times,e} = -\frac{5}{2}\frac{p_e}{eB}\boldsymbol{b}\times\nabla T_e \tag{2.47}$$

where $\boldsymbol{b} = \boldsymbol{B}/B$ is the magnetic unit vector. These fluxes are commonly referred to as the diamagnetic heat flux [48]. Going to next order, the collisional contributions to the heat fluxes perpendicular to magnetic field are:

$$\begin{aligned}\boldsymbol{q}_{\perp,\alpha} = {}& \frac{p_\alpha}{m_\alpha^2\Omega_{c,\alpha}^2}\sum_\beta \mu_{\alpha\beta}\nu_{\beta\to\alpha}\left(\frac{3}{2}\left[\frac{\nabla p_\alpha}{n_\alpha} - \frac{Z_\alpha \nabla p_\beta}{Z_\beta n_\beta}\right]\right. \\ & \left. - \frac{m_\alpha}{m_\alpha + m_\beta}\left[\left(\frac{13}{4}\frac{m_\beta}{m_\alpha} + 4 + \frac{15}{2}\frac{m_\alpha}{m_\beta}\right)\nabla T_\alpha - \frac{27}{4}\frac{Z_\alpha}{Z_\beta}\nabla T_\beta\right]\right). \end{aligned} \tag{2.48}$$

$$\begin{aligned}\boldsymbol{q}_{\perp,e} = {}& \frac{p_e}{m_e\Omega_{c,e}^2}\sum_\alpha \nu_{\alpha\to e}\left(\frac{3}{2}\left[\frac{\nabla p_e}{n_e} + \frac{\nabla p_\alpha}{Z_\alpha n_\alpha}\right]\right. \\ & \left. - \left[\left(\frac{13}{4} + \frac{\sqrt{2}}{Z_\alpha}\right)\nabla T_e\right]\right). \end{aligned} \tag{2.49}$$

In this last expression, the collisional electron heat flux was reduced in complexity following [38].

**Viscous stress tensor** To express the viscous stress tensor is it useful to first write the rate of stress tensor [34]:

$$\boldsymbol{W} = \nabla \boldsymbol{u}_\alpha + (\nabla \boldsymbol{u}_\alpha)^T - \frac{2}{3}\boldsymbol{I}\nabla \cdot u_\alpha \tag{2.50}$$

It is further useful to split the tensor into a parallel part, a perpendicular non-collisional gyroviscous part and a pependicular collisional part [49]:

$$\boldsymbol{\pi} = \boldsymbol{\pi}_{\|} + \boldsymbol{\pi}_{gy} + \boldsymbol{\pi}_{\perp} \tag{2.51}$$

As before, the parallel term is neglected as only the perpendicular parts are of interest. With the rate of stress tensor, the perpendicular components can be written as [34]:

$$\begin{aligned}\boldsymbol{\pi}_{s,gy} =& \frac{\eta_{s,gy}}{2}\left[\boldsymbol{b}\times\boldsymbol{W}\cdot(\boldsymbol{I}-\boldsymbol{bb}) - (\boldsymbol{I}-\boldsymbol{bb})\cdot\boldsymbol{W}\times\boldsymbol{b}\right] \\ &+ 2\eta_{s,gy}\left[\boldsymbol{b}\times\boldsymbol{W}\cdot\boldsymbol{bb} - \boldsymbol{bb}\cdot\boldsymbol{W}\times\boldsymbol{b}\right] \qquad (2.52) \\ \boldsymbol{\pi}_{s,\perp} =& -\eta_{s,\perp}\left[(\boldsymbol{I}-\boldsymbol{bb})\cdot\boldsymbol{W}\cdot(\boldsymbol{I}-\boldsymbol{bb}) + \frac{1}{2}(\boldsymbol{I}-\boldsymbol{bb})(\boldsymbol{b}\cdot\boldsymbol{W}\cdot\boldsymbol{b})\right] \\ &- 4\eta_{s,\perp}\left[(\boldsymbol{I}-\boldsymbol{bb})\cdot\boldsymbol{W}\cdot\boldsymbol{bb} + \boldsymbol{bb}\cdot\boldsymbol{W}\cdot(\boldsymbol{I}-\boldsymbol{bb})\right] \qquad (2.53)\end{aligned}$$

The coefficients for $\eta_{\alpha,gy}$ and $\eta_{\alpha,\perp}$ are:

$$\eta_{s,gy} = \frac{p_s}{2\Omega_{c,s}} \tag{2.54}$$

$$\eta_{s,\perp} = \sum_\beta \eta_{s'\to s,\perp} = \frac{1}{4}\frac{p_s}{\Omega_{c,s}^2}\sum_{s'}\frac{m_s m_s'}{(m_s+m_{s'})^2}\cdot\nu_{s'\to s}\left(\frac{6}{5}\frac{m_{s'}}{m_\alpha} + 2 - \frac{4}{5}\frac{m_{s'}}{m_s}\frac{Z_s}{Z_{s'}}\right). \tag{2.55}$$

Due to the appearance of the species gyro-frequency in the denominator, the electron version is small compared to ions. Hence it can be neglected.

**Correction to resistive force** While the above expressions closes the system of equations, the closure scheme allows for a correction to the perpendicular resistive force:

$$\boldsymbol{R}_{s'\to s,T,\perp} = \frac{3}{2}m_s n_s \nu_{s'\to s}\mu_{s's}\left(\frac{\boldsymbol{b}\times\nabla T_s}{m_s q_s B} - \frac{\boldsymbol{b}\times\nabla T_{s'}}{m_{s'}q_{s'}B}\right). \tag{2.56}$$

This the thermal resistive force. The physical meaning of this terms is discussed in detail in [37]. Summing over all species $s'$ this together with frictional resistive force in Eq. (2.29) constitutes the total resistive force $\boldsymbol{R}_{s,\perp}$

acting on a species $s$. In this regard it should be noted that the expression yields momentum conservation:

$$\boldsymbol{R}_{s'\to s,\perp} = -\boldsymbol{R}_{s\to s',\perp} \tag{2.57}$$

With this, closed forms of equations for density, fluid velocity and pressure can now be given. These were obtained by taking moments of Boltzmann equation and using the Zhdanov closure scheme. Lastly remains the source terms.

### 2.1.3 Source terms

The sources were not explicitly given in the moment equations for density, fluid velocity and pressure. Working in the fluid picture one can define fundamental sources $\Sigma_f$ where $f$ denotes one of the fundamental fluid variables, $n$, $\boldsymbol{u}$, $T$ etc. Physically, these sources could be the addition of particles, application of an external field that accelerates the plasma fluid or the heating, by e.g. ICRH. The function $\Sigma_f$ can be any function describing a desired physical situation. It is instructive to write the general sources appearing in the density, velocity and pressure equations denoted $S_f$ in terms of these fundamental sources [50]. The general source terms were again a function of the energy source $S_E$ and flux source $S_\Gamma$. Beginning with the density there is not much new. It is a rather fundamental quantity so one simply has:

$$S_n = \Sigma_n \tag{2.58}$$

For the fluid source:

$$\boldsymbol{S}_\Gamma = m\boldsymbol{u}'\Sigma_n + mn\boldsymbol{\Sigma}_u \tag{2.59}$$

where $\boldsymbol{u}'$ is the flow velocity of the added particles. The exact nature of $\boldsymbol{\Sigma}_u$ depends on the situation, but could be e.g. an external electrical field or something similar. Finally the source for the total energy is comprised as:

$$S_E = \frac{1}{2}m\boldsymbol{u}'^2\Sigma_n + mn\boldsymbol{u}\cdot\Sigma_u + \frac{3}{2}\left(T'\Sigma_n + n\Sigma_T\right) \tag{2.60}$$

The first term here corresponds to the addition of the fluid kinetic energy of newly added particles, while the second corresponds to the increase in fluid kinetic energy brought about by acceleration of the fluid due to some fluid velocity source. The last term is the increase in total energy by the addition of new particles with a temperature $T'$ or by a thermal heating of existing particles. In $T'$ care must be taken, in the sense that the particle may be newly formed, possibly in the form of an atomic process such as ionisation [51]. Here the temperature of the electron is not the same as the temperature of the neutral particle, instead one has $T'_e = m_e/m_n T'_n$. It appears that for all moment sources, there is a need for all lower moment sources. In the expressions for the density, momentum and pressure the total source terms can now be expressed in terms of fundamental sources [50]:

$$S_n = \Sigma_n \tag{2.61}$$

$$mn\boldsymbol{S}_u = \boldsymbol{S}_\Gamma - m\boldsymbol{u}S_n = m\left(\boldsymbol{u}' - \boldsymbol{u}\right)\Sigma_n + mn\boldsymbol{\Sigma}_u \tag{2.62}$$

$$S_p = S_E - \boldsymbol{u}\cdot S_\Gamma + \frac{1}{2}mu^2 S_n = \frac{1}{2}m\left(\boldsymbol{u}' - \boldsymbol{u}\right)^2\Sigma_n + \frac{3}{2}\left(T'\Sigma_n + n\Sigma_T\right) \tag{2.63}$$

It should be noted that the pressure source is unaffected by the acceleration. Naturally this is to be expected as pressure is related to the particles and their thermal motion, to which the fluid velocity source adds nothing.

With this, there is now a complete closed set of equations for the fluid variables, density, fluid velocity and pressure (or temperature).

## 2.2 Drift fluid expansion

Even though the equations of the macroscopic values $n_\alpha$, $\boldsymbol{u}_\alpha$ and $p_\alpha$ along with expressions for $\boldsymbol{q}_\alpha$, $\boldsymbol{\pi}_\alpha$ and $R_\alpha$ form a closed set of equations, they are still too tedious to work with. First, the number of equations for each species is four (or five for 3D). Second, the equations allow for high-resolution length and time scales. To overcome both problems a common procedure used in plasma physics is the so-called drift fluid approximation. The idea is to make an order of magnitude expansion of the velocity and then use characteristic length and time scales of the physical phenomena of interest to order the terms in the velocity equation [38], [52], [53]. Concerning this work, the interesting physical phenomena are turbulent transport occurring at the outboard midplane.

**A note on the magnetic field** Before deriving the drift fluid model, it is worthwhile to consider the magnetic field composition. As mentioned in the introduction the domain of the study is a 2D slab located at the outboard mid-plane of the tokamak. If the poloidal contribution to the magnetic field is assumed to be negligible or slowly varying over the domain, the changes in the magnetic direction are small from flux surface to flux surface, meaning the magnetic shear is negligible [5]. In such a case, the magnetic field perpendicular to the 2D slab can be considered parallel everywhere. If the major radius of the tokamak $R$ is much bigger than the minor radius $r$, the aspect is large meaning the magnetic curvature is small. In such a case the magnetic field can be assumed straight, which means it can be in a Cartesian coordinate system as represented as:

$$\boldsymbol{B}(x) = \frac{B_0 R}{R+r+x}\hat{\boldsymbol{z}} \tag{2.64}$$

where $B_0$ is the field strength at the major radius $R$ and $r$ is the minor radius. $x=0$ is the last closed flux surface and as such positive $x$ from the last closed flux surface into the scrape-off-layer. This constitutes the form of the magnetic field that is used in this work. It should be noted that the zero-curvature assumption is not necessary for the derivation of the drift fluid model in a slab geometry, but the low shear is.

### 2.2.1 Drift fluid velocities

For turbulent transport it is assumed that the dynamics evolve on time scales much slower than the ion gyro-frequency time scale and that the perpendicular gradient length scales are much longer than the ion gyro-radius length scales:

$$\frac{\omega}{\Omega_{c,s}} \sim \epsilon \quad \text{and} \quad \frac{\nabla\cdot\boldsymbol{u}_\perp}{\Omega_{c,s}} \sim \epsilon \tag{2.65}$$

where $\epsilon \ll 1$ and $\omega$ is some characteristic frequency. This means that $\omega \sim \partial_t \sim \epsilon$. Furthermore, the system is assumed weakly collisional meaning the resistive force is small $|\boldsymbol{R}_{s'\to s}| \sim \epsilon$. The viscosity is also taken to be of order $\epsilon$ [37], [54]. Additionally, the pressure is assumed to be order 1 and the same goes for $\boldsymbol{E}/B$. Expanding the perpendicular fluid velocity in terms of order of $\epsilon$ yields:

$$\boldsymbol{u}_{s,\perp} = \boldsymbol{u}_{s,0,\perp} + \epsilon\boldsymbol{u}_{s,1,\perp} + \epsilon^2\boldsymbol{u}_{s,2,\perp} + \ddots. \tag{2.66}$$

With the above orderings the momentum equation can then be expanded as:

$$\begin{aligned}
0 = \epsilon^0 q_s n_s &\left(\boldsymbol{E} + \left[\epsilon^0\boldsymbol{u}_{s,0,\perp} + \epsilon^1\boldsymbol{u}_{s,1,\perp} + \cdots\right]\times\boldsymbol{B} - \frac{\nabla p_s}{q_s n_s}\right)\\
+\epsilon^1&\left(-m_s n_s\left[\frac{\partial}{\partial t} + \left(\epsilon^0\boldsymbol{u}_{s,0,\perp} + \epsilon^1\boldsymbol{u}_{s,1,\perp} + \cdots\right)\cdot\nabla\right]\left(\epsilon^0\boldsymbol{u}_{s,0} + \epsilon^1\boldsymbol{u}_{s,1,\perp} + \cdots\right)\right.\\
&-\nabla\cdot\boldsymbol{\pi}_s(\epsilon^0\boldsymbol{u}_{s,0,\perp} + \epsilon^1\boldsymbol{u}_{s,1,\perp} + \cdots) + \boldsymbol{R}_s(\epsilon^0\boldsymbol{u}_{s,0,\perp} + \epsilon^1\boldsymbol{u}_{s,1,\perp} + \cdots)\\
&\left.+ m_s n_s\boldsymbol{S}_{u,s,\perp}(\epsilon^0\boldsymbol{u}_{s,0,\perp} + \epsilon^1\boldsymbol{u}_{s,1,\perp} + \cdots)\right).
\end{aligned} \tag{2.67}$$

Where is was used that the total derivative in the momentum equation (Eq. (2.31)) is given as

$$\frac{d}{dt} = \frac{\partial}{\partial t} + (\boldsymbol{u}_s \cdot \nabla)\,. \tag{2.68}$$

Collecting terms of same order gives for $\epsilon^0$:

$$0 = q_s n_s \Big(\boldsymbol{E} + \boldsymbol{u}_{s,0,\perp} \times \boldsymbol{B}\Big) - \nabla p_s \tag{2.69}$$

and for $\epsilon^1$:

$$\begin{aligned} 0 = q_s n_s \boldsymbol{u}_{s,1} \times \boldsymbol{B} - m_s n_s \left(\frac{\partial}{\partial t} + \boldsymbol{u}_{s,0,\perp} \cdot \nabla\right) \boldsymbol{u}_{s,0} - \nabla \cdot \pi_s(\boldsymbol{u}_{s,0,\perp}) \\ + \boldsymbol{R}_s(\boldsymbol{u}_{s,0,\perp}) + m_s n_s \boldsymbol{S}_{u,s,\perp}(\boldsymbol{u}_{s,0,\perp}). \end{aligned} \tag{2.70}$$

Although the expansion has no end, it needs to be truncated at some point. Luckily, the nature of the expansion is such that only velocities of order $\epsilon^n$ and below are needed to evaluate all terms of order $\epsilon^n$. This means a truncation can be done at any stage without any considerations on the higher orders, except that they are assumed negligible. It is common to truncate at $\epsilon^1$, as is done here, since all terms of the fluid velocity equation are present. With this out of the way, it is possible to derive expressions for $\boldsymbol{u}_{s,0}$ and $\boldsymbol{u}_{s,1}$. Since it is perpendicular transport that is of interest, the procedure is to apply $\boldsymbol{b}\times$ to the equation (2.69):

$$\begin{aligned} 0 &= q_s n_s \Big(\boldsymbol{b} \times \boldsymbol{E} + \boldsymbol{b} \times \boldsymbol{u}_{s,0,\perp} \times \boldsymbol{B}\Big) - \boldsymbol{b} \times \nabla p_s \\ &= q_s n_s \Big(\boldsymbol{b} \times \boldsymbol{E} + B \boldsymbol{u}_{s,0,\perp}\Big) - \boldsymbol{b} \times \nabla p_s \\ \Rightarrow \boldsymbol{u}_{s,0,\perp} &= \frac{\boldsymbol{b} \times \nabla \phi}{B} + \frac{\boldsymbol{b} \times \nabla p_s}{q_s n_s B} \equiv \boldsymbol{u}_{s,E} + \boldsymbol{u}_{s,d} \end{aligned} \tag{2.71}$$

Here it was used that the electric field and potential are related as $\boldsymbol{E} = -\nabla\phi$ in the case of the electrostatic approximation. To get the perpendicular part of the velocity, the triple vector product (or BACCAB) rule is used: $\boldsymbol{b} \times (\boldsymbol{a} \times \boldsymbol{b}) = \boldsymbol{a}(\boldsymbol{b} \cdot \boldsymbol{b}) - \boldsymbol{b}(\boldsymbol{a} \cdot \boldsymbol{b}) = b^2 \boldsymbol{a} - b^2 \boldsymbol{b}/b(\boldsymbol{a} \cdot \boldsymbol{b}/b) = b^2 \boldsymbol{a}_\perp$. The velocity components correspond to the $E \times B$-drift and diamagnetic drift. The $E \times B$-drift is well known from from single particle motion where particles in a magnetic field under the influence of an electric field will drift perpendicular to the two fields. This type of drift is the main driver for transport of particles. The diamagnetic drift on the other hand does not advect particles, rather in the case of pressure gradients more gyrating particles are in the high pressure region compared to low pressure region. This gives the appearance of a flow without any motion of the gyro-centers. It should be noted that while it is not an actual drift, it can be related to the grad-B drift, curvature drift and magnetization drift [55]. Moving on to the next order the same procedure is followed applying $\boldsymbol{b}\times$ to (2.70) and use the BACCAB rule again to obtain:

$$\begin{aligned}
0 =& q_s n_s \boldsymbol{b} \times \boldsymbol{u}_{s,1} \times \boldsymbol{B} - n_s m_s \boldsymbol{b} \times \left(\frac{\partial}{\partial t} + \boldsymbol{u}_{s,0} \cdot \nabla\right) \boldsymbol{u}_{s,0} \\
& - \boldsymbol{b} \times \nabla \cdot \boldsymbol{\pi}_s(\boldsymbol{u}_{s,0}) + \boldsymbol{b} \times \boldsymbol{R}_s(\boldsymbol{u}_{s,0}) + m_s n_s \boldsymbol{b} \times \boldsymbol{S}_u(\boldsymbol{u}_{s,0}) \\
=& q_s n_s \boldsymbol{u}_{s,1,\perp} B - n_s m_s \boldsymbol{b} \times \left(\frac{\partial}{\partial t} + \boldsymbol{u}_{s,0} \cdot \nabla\right) \boldsymbol{u}_{s,0} \\
& - \boldsymbol{b} \times \nabla \cdot \boldsymbol{\pi}_s(\boldsymbol{u}_{s,0}) + \boldsymbol{b} \times \boldsymbol{R}_s(\boldsymbol{u}_{s,0}) + m_s n_s \boldsymbol{b} \times \boldsymbol{S}_u(\boldsymbol{u}_{s,0}) \\
\Rightarrow \boldsymbol{u}_{s,1,\perp} =& \frac{m_s}{q_s B} \boldsymbol{b} \times \left(\frac{\partial}{\partial t} + \boldsymbol{u}_{s,0} \cdot \nabla\right) \boldsymbol{u}_{s,0} + \frac{\nabla \cdot \boldsymbol{\pi}_s(\boldsymbol{u}_{s,0})}{q_s n_s B} \\
& - \frac{\boldsymbol{b} \times \boldsymbol{R}_s(\boldsymbol{u}_{s,0})}{q_s n_s B} - \frac{m_s \boldsymbol{b} \times \boldsymbol{S}_s(\boldsymbol{u}_{s,0})}{q_s B} \\
\equiv& \boldsymbol{u}_{s,p} + \boldsymbol{u}_{s,\pi} + \boldsymbol{u}_{s,R} + \boldsymbol{u}_{S_{u,s}}
\end{aligned} \tag{2.72}$$

The four terms arising here are the polarisation term, which is a correction to the $E \times B$ and diamagnetic drifts [56], the viscosity drift due to the stress tensor, the resistive drift due to collisional interactions with other species and a source/sink drift due to either the contribution of new particles or some source in the velocity. This now gives a closed set of equations for the velocities and so we no longer need to solve the momentum equation. If one in the future wishes to have more terms included, the procedure is very simple as one just does what was done to the two lowest orders, i.e. apply $\boldsymbol{b}\times$ and solve for $u_{\alpha,n}$ in terms of lower order drifts. Above, six drift terms have been defined, where the $E \times B$ and the diamagnetic drift were explicitly given. The $\epsilon^1$ terms are all given through as functions of the $\epsilon^0$ drifts. Proceeding now to write them out explicitly gives for the polarisation drift:

$$\begin{aligned}
\boldsymbol{u}_{s,p} &= \frac{m_s}{q_s B} \boldsymbol{b} \times \left(\frac{\partial}{\partial t} + \boldsymbol{u}_{s,0} \cdot \nabla\right) \boldsymbol{u}_{s,0} \\
&= \frac{m_s}{q_s B} \boldsymbol{b} \times \left(\frac{\partial}{\partial t} + \left[\frac{\boldsymbol{b} \times \nabla \phi}{B} + \frac{\boldsymbol{b} \times \nabla p_s}{q_s n_s B}\right] \cdot \nabla\right) \left[\frac{\boldsymbol{b} \times \nabla \phi}{B} + \frac{\boldsymbol{b} \times \nabla p_s}{q_s n_s B}\right]
\end{aligned} \tag{2.73}$$

In the electrostatic approximations $\partial_t \boldsymbol{b} = 0$. Additionally, it is assumed that the local curvature of the magnetic field is negligible and so $\nabla \boldsymbol{b} = 0$. With this and some vector algebra to move the $\boldsymbol{b}\times$ under the derivative sign yields:

$$\begin{aligned}\boldsymbol{u}_{s,p} &= -\frac{m_s}{q_sB}\left(\frac{\partial}{\partial t}+\left[\frac{\boldsymbol{b}\times\nabla\phi}{B}+\frac{\boldsymbol{b}\times\nabla p_s}{q_sn_sB}\right]\cdot\nabla\right)\left[\frac{\nabla_\perp\phi}{B}+\frac{\nabla_\perp p_s}{q_sn_sB}\right]\\ &= -\frac{m_s}{q_sB}\left(\frac{\partial}{\partial t}+\boldsymbol{u}_{s,0}\cdot\nabla\right)\boldsymbol{u}_{s,0,\perp} \qquad (2.74)\end{aligned}$$

The resistive drift $\boldsymbol{R}_{s'\to s}$ consists of a frictional force and thermal force. Inserting the expression for the lowest order drifts in the frictional force (Eq. (2.29)) yields:

$$\begin{aligned}\boldsymbol{u}_{s,R,u,\perp} &= -\frac{\boldsymbol{b}\times\boldsymbol{R}_{u,s}(\boldsymbol{u}_{s,0})}{q_sn_sB} = -\sum_{s'}\frac{\boldsymbol{b}}{q_sn_sB}\times\left(-m_sn_s\nu_{s'\to s}\left[\boldsymbol{u}_s-\boldsymbol{u}_{s'}\right]\right)\\ &= \sum_{s'}m_s\nu_{s'\to s}\frac{\boldsymbol{b}}{q_sB}\times\left(\cancel{\frac{\boldsymbol{b}\times\nabla\phi}{B}}+\frac{\boldsymbol{b}\times\nabla p_s}{q_sn_sB}-\cancel{\frac{\boldsymbol{b}\times\nabla\phi}{B}}-\frac{\boldsymbol{b}\times\nabla p_s}{q'_sn'_sB}\right)\\ &= -\sum_{s'}\frac{m_s\nu_{s'\to s}}{q_sB}\left(\frac{\nabla_\perp p_s}{q_sn_sB}-\frac{\nabla_\perp p_s}{q'_sn'_sB}\right) \qquad (2.75)\end{aligned}$$

Doing the same for the thermal resistive force in Eq. (2.56) gives:

$$\begin{aligned}\boldsymbol{u}_{s,R,T,\perp} &= -\frac{\boldsymbol{b}\times\boldsymbol{R}_{T,s}(\boldsymbol{u}_{s,0})}{q_sn_sB}\\ &= -\frac{\boldsymbol{b}\times}{q_sn_sB}\left(\frac{3}{2}m_sn_s\nu_{s'\to s}\mu_{s's}\left(\frac{\boldsymbol{b}\times\nabla T_s}{m_sq_sB}-\frac{\boldsymbol{b}\times\nabla T_{s'}}{m_{s'}q_{s'}B}\right)\right)\\ &= \frac{3}{2}\frac{n_s\nu_{s'\to s}\mu_{s's}}{q_sn_sB}\left(\frac{\nabla_\perp T_s}{m_sq_sB}-\frac{\nabla_\perp T_{s'}}{m_{s'}q_{s'}B}\right) \qquad (2.76)\end{aligned}$$

It should here be noted that because $n_sm_s\nu_{s'\to s} = n_{s'}m_{s'}\nu_{s\to s'}$ it can be shown that $Z_sn_s\boldsymbol{u}_{R,s'\to s} = -Z_{s'}n_{s'}\boldsymbol{u}_{R,s\to s'}$.

For the viscous drift, the collisional perpendicular part results in the corresponding drift

$$\begin{aligned}\boldsymbol{u}_{\pi,\perp} = \frac{1}{q_\alpha n_\alpha B}&\left[\begin{matrix}\partial_x\eta_{\alpha,\perp}\left(\partial_x(\frac{\partial_x\phi}{B}+\frac{\partial_xp_\alpha}{q_\alpha n_\alpha B})-\partial_y(\frac{\partial_y\phi}{B}+\frac{\partial_yp_\alpha}{q_\alpha n_\alpha B})\right)\\ \partial_x\eta_{\alpha,\perp}\left(\partial_x(\frac{\partial_y\phi}{B}+\frac{\partial_yp_\alpha}{q_\alpha n_\alpha B})+\partial_y(\frac{\partial_x\phi}{B}+\frac{\partial_xp_\alpha}{q_\alpha n_\alpha B})\right)\\ 0\end{matrix}\right.\\ &\left.\begin{matrix}+\partial_y\eta_{\alpha,\perp}\left(\partial_x(\frac{\partial_y\phi}{B}+\frac{\partial_yp_\alpha}{q_\alpha n_\alpha B})+\partial_y(\frac{\partial_x\phi}{B}+\frac{\partial_xp_\alpha}{q_\alpha n_\alpha B})\right)\\ -\partial_y\eta_{\alpha,\perp}\left(\partial_x(\frac{\partial_x\phi}{B}+\frac{\partial_xp_\alpha}{q_\alpha n_\alpha B})-\partial_y(\frac{\partial_y\phi}{B}+\frac{\partial_yp_\alpha}{q_\alpha n_\alpha B})\right)\\ 0\end{matrix}\right] \qquad (2.77)\end{aligned}$$

Similarly the gyro-viscous contribution to the viscous drift becomes:

$$\begin{aligned}\boldsymbol{u}_{\pi,gy} = \frac{1}{q_\alpha n_\alpha B} & \left[\begin{matrix} \partial_x \eta_{\alpha,gy}\Big(\partial_x(\frac{\partial_y \phi}{B} + \frac{\partial_y p_\alpha}{q_\alpha n_\alpha B}) + \partial_y(\frac{\partial_x \phi}{B} + \frac{\partial_x p_\alpha}{q_\alpha n_\alpha B})\Big) \\ -\partial_x \eta_{\alpha,gy}\Big(\partial_x(\frac{\partial_x \phi}{B} + \frac{\partial_x p_\alpha}{q_\alpha n_\alpha B}) - \partial_y(\frac{\partial_y \phi}{B} + \frac{\partial_y p_\alpha}{q_\alpha n_\alpha B})\Big) \\ 0 \end{matrix}\right. \\ & \left.\begin{matrix} -\partial_y \eta_{\alpha,gy}\Big(\partial_x(\frac{\partial_x \phi}{B} + \frac{\partial_x p_\alpha}{q_\alpha n_\alpha B}) - \partial_y(\frac{\partial_y \phi}{B} + \frac{\partial_y p_\alpha}{q_\alpha n_\alpha B})\Big) \\ -\partial_y \eta_{\alpha,gy}\Big(\partial_x(\frac{\partial_y \phi}{B} + \frac{\partial_y p_\alpha}{q_\alpha n_\alpha B}) + \partial_y(\frac{\partial_x \phi}{B} + \frac{\partial_x p_\alpha}{q_\alpha n_\alpha B})\Big) \\ 0 \end{matrix}\right]\end{aligned} \tag{2.78}$$

Lastly remains the source drifts. With the definitions of $\boldsymbol{S}_u$ and $S_n$ given in Eqs. (2.61) and (2.62) the resulting drift is given by:

$$\boldsymbol{u}_{S_u,s} = -\frac{m_s \boldsymbol{b} \times \boldsymbol{S}_{u,s}}{q_s B} = -\frac{m_s}{q_s B}\left(\left[\boldsymbol{b} \times \boldsymbol{u}'_s + \frac{\nabla \phi}{B} + \frac{\nabla p_s}{q_s n_s B}\right]\frac{\Sigma_{n,s}}{n_s} + \boldsymbol{b} \times \boldsymbol{\Sigma}_{u,s}\right) \tag{2.79}$$

This concludes the individual drifts from the drift fluid expansion.

### 2.2.2 Drift reduced moment equations

With the continuity equation in Eq. (2.21) and the drift velocities derived above, the drift reduced continuity equation can now be written out. Here it is beneficial to split it into ion density equations and electron density equation. The reason for this is that the polarisation drift and viscosity drift both depend on mass and so are much smaller than their ion counterpart meaning they can be neglected. For the ions the density equation becomes:

$$\frac{\partial}{\partial t} n_\alpha + \nabla \cdot \Big(n_\alpha \Big[\boldsymbol{u}_E + \boldsymbol{u}_{D,\alpha} + \boldsymbol{u}_{p,\alpha} + \boldsymbol{u}_{\boldsymbol{R},\alpha} + \boldsymbol{u}_{\pi,\alpha} + \boldsymbol{u}_{S_{u,\alpha}}\Big]\Big) = S_{n_\alpha} \tag{2.80}$$

The electron counterpart with the mass consideration becomes:

$$\frac{\partial}{\partial t} n_e + \nabla \cdot \Big(n_e \Big[\boldsymbol{u}_E + \boldsymbol{u}_{D,e} + \boldsymbol{u}_{\boldsymbol{R},e} + \boldsymbol{u}_{S_{u,e}}\Big]\Big) = S_{n_e} \tag{2.81}$$

Since the drift fluid expansion has been performed there is no need to look at the momentum equation any more and leaving only the pressure equations.

With the drifts, this gives the ion pressure equation:

$$\begin{aligned}
&\frac{3}{2}\frac{\partial}{\partial t}p_\alpha + \frac{3}{2}\nabla\cdot\Big(p_\alpha\Big[\boldsymbol{u}_E + \boldsymbol{u}_{D,\alpha} + \boldsymbol{u}_{p,\alpha} + \boldsymbol{u}_{R,\alpha} + \boldsymbol{u}_{\pi,\alpha}\Big]\Big)\\
&+ p_\alpha\nabla\cdot\Big(\boldsymbol{u}_E + \boldsymbol{u}_{D,\alpha} + \boldsymbol{u}_{p,\alpha} + \boldsymbol{u}_{R,\alpha} + \boldsymbol{u}_{\pi,\alpha}\Big) + \boldsymbol{\pi}_\alpha : \nabla\boldsymbol{u}_{0,\alpha} + \nabla\cdot\boldsymbol{q}_\alpha\\
=&Q_\alpha - \Big(\boldsymbol{u}_E + \boldsymbol{u}_{D,\alpha}\Big)\cdot\boldsymbol{R}_\alpha(\boldsymbol{u}_0)\\
&+ S_{p_\alpha} - \Big(\boldsymbol{u}_E + \boldsymbol{u}_{D,\alpha}\Big)\cdot\boldsymbol{S}_{u_\alpha} + \frac{1}{2}m_\alpha\Big(\boldsymbol{u}_E + \boldsymbol{u}_{D,\alpha}\Big)^2 S_{n_\alpha}
\end{aligned}\tag{2.82}$$

and the electron pressure equation

$$\begin{aligned}
&\frac{3}{2}\frac{\partial}{\partial t}p_e + \frac{3}{2}\nabla\cdot\Big(p_e\Big[\boldsymbol{u}_E + \boldsymbol{u}_{D,e} + \boldsymbol{u}_{R,e}\Big]\Big)\\
&+ p_e\nabla\cdot\Big(\boldsymbol{u}_E + \boldsymbol{u}_{D,\alpha} + \boldsymbol{u}_{R,\alpha}\Big) + \nabla\cdot\boldsymbol{q}_e\\
=&Q_e - \Big(\boldsymbol{u}_E + \boldsymbol{u}_{D,\alpha}\Big)\cdot\boldsymbol{R}_e(\boldsymbol{u}_0)\\
&+ S_{p_e} - \Big(\boldsymbol{u}_E + \boldsymbol{u}_{D,e}\Big)\cdot\boldsymbol{S}_{u,e} + \frac{1}{2}m_e\Big(\boldsymbol{u}_E + \boldsymbol{u}_{D,e}\Big)^2 S_{n,e}
\end{aligned}\tag{2.83}$$

While there are now equations for the density and pressure and the momentum is no longer needed, there is still the need for an equation that updates the electric field. As mentioned the, the electrostatic approximation is used with the magnetic field assumed constant. A common approach to find the electric field and consequently the potential could be to simply find the charge distribution by subtracting the electron charge density $en_e$ from the ion charge distribution $\sum_\alpha Z_\alpha en_\alpha$ and the solve the corresponding Poisson equation:

$$\nabla^2\phi = -\frac{e\left(\sum_\alpha Z_\alpha n_\alpha - n_e\right)}{\epsilon^0}\tag{2.84}$$

While simple, it would involve fast time scales. The trick is to invoke the assumption of quasi-neutrality $n_e \approx \sum_\alpha Z_\alpha n_\alpha$. What is meant with this is that it is assumed that the macroscopic plasma to be neutral[30]. What it does not mean, however, is that there can be no electrical field. The reason for this is that fluctuations on the Debye length scale are allowed which consequently allows for small electric fields. This is needed for the drift wave instability to evolve.

From the ion equation it is seen that it contains the polarisation term which includes the time derivative of the vorticity $\omega = \frac{\nabla^2\phi}{B}$. Subtracting the electron density equation from the sum of ion density equation yields:

$$\frac{\partial}{\partial t}\sum_{\alpha} Z_\alpha n_\alpha - ne + \nabla\cdot\left(\sum_{\alpha} Z_\alpha n_\alpha \left[\boldsymbol{u}_E + \boldsymbol{u}_{D,\alpha} + \boldsymbol{u}_{p,\alpha} + \boldsymbol{u}_{\boldsymbol{R},\alpha} + \boldsymbol{u}_{\pi,\alpha}\right]\right.$$
$$\left. - n_e\left[\boldsymbol{u}_E + \boldsymbol{u}_{D,e} + \boldsymbol{u}_{\boldsymbol{R},e}\right]\right) = \sum_{\alpha} Z_\alpha S_{n_\alpha} - S_{n_e} \qquad (2.85)$$

Due to the quasi-neutrality condition, the $\partial_t n$ terms cancel each other and the same goes for the $\boldsymbol{u}_E$ terms. Furthermore, as noted earlier $Z_s n_s \boldsymbol{u}_{R,s'\to s} = -Z_{s'} n_{s'} \boldsymbol{u}_{R,s\to s'}$ and so all resistive force terms drop out. With these considerations we can now write the vorticity equation as:

$$\sum Z_\alpha \nabla\cdot n_\alpha \frac{m_\alpha}{q_\alpha B}\left(\frac{\partial}{\partial t} + \boldsymbol{u}_{\alpha,0}\cdot\nabla\right)\boldsymbol{u}_{\alpha,0,\perp}$$
$$= \nabla\cdot n_e \boldsymbol{u}_{D,e} \sum_{\alpha} Z_\alpha \nabla\cdot n_\alpha \left(\boldsymbol{u}_{D,\alpha} + \boldsymbol{u}_{\pi,\alpha}\right) - \nabla\cdot\left(n_e \boldsymbol{u}_D\right) \qquad (2.86)$$

This now needs to be solved in regards to $\partial_t\phi$ which unfortunately is rather non-trivial as will be seen in the section on the numerical implementation. This concludes all equations needed for a full system of coupled pde's that can be be used to study turbulent transport.

### 2.2.3 The MIHESEL equations

The equations as they are now are still somewhat computationally unwieldy and so the aim is to reduce the complexity. This is done in two parts, one where the individual expression within the equations is used to reduce the number of terms and simplify. This does not change the physics of the equations. The other part is where a number of approximations are employed to make the model suitable for numerical implementation. The final set of equations after these steps is the Multi-Ion Hot Edge/SOL Electrostatic, abbreviated MIHESEL, model, an update of the HESEL model [17], which does the same, but only for a single ion species.

#### 2.2.3.1 Term reduction

To start, the polarisation drift and gyro-viscous drift terms in the density equation are considered. For these two terms what is commonly referred to as gyro-viscous cancellation is employed [53], [57]–[59]. Omitting the derivation, the consequence of the cancellation is that part of the gyro-viscous stress tensor cancels the diamagnetic advection contribution in the polarisation terms:

$$\nabla\cdot\boldsymbol{\pi}_{gy,\perp,\alpha} + n_\alpha\left(\boldsymbol{u}_{D,\alpha}\cdot\nabla\right)\boldsymbol{u}_{\perp,\alpha,0} = \nabla_\perp\chi. \qquad (2.87)$$

Where $\nabla_\perp \chi$ is the remainder of the gyro-viscous cancellation. As this appears in the density equation it will naturally carry over to the vorticity equation. The exact form of the remainder term is not discussed here as it is dropped due to only contributing when the magnetic field is inhomogeneous in which case the contribution is small. Moving on to the pressure equations, the diamagnetic contributions from the drifts and the heat flux are reduced as follows:

$$\begin{aligned}
&\frac{3}{2}\nabla\cdot p_s\boldsymbol{u}_{D,s} + p_s\nabla\cdot\boldsymbol{u}_{D,s} + \nabla\cdot\boldsymbol{q}_{\times,s} \\
=&\frac{3}{2}\nabla\cdot\left(T_s\frac{\boldsymbol{b}\times\nabla p_s}{q_sB}\right) + p_s\nabla\cdot\frac{\boldsymbol{b}\times\nabla p_s}{q_sn_sB} + \nabla\cdot\left(\frac{5}{2}\frac{p_s}{q_sB}\boldsymbol{b}\times\nabla T_s\right) \\
=&\frac{5}{2}\nabla\cdot\left(\frac{T_s}{q_sB}\boldsymbol{b}\times\nabla p_s\right) - \cancelto{0}{\frac{\boldsymbol{b}\times\nabla p_s}{q_sn_sB}\cdot\nabla p_s} + \frac{5}{2}\nabla\cdot\left(\frac{p_s}{q_sB}\boldsymbol{b}\times\nabla T_s\right) \\
=&\frac{5}{2}\nabla\cdot\left(\frac{\boldsymbol{b}}{q_sB}\times\nabla\left[n_sp_s\right]\right) = \frac{5}{2}\nabla\times\left(\frac{\boldsymbol{b}}{q_sB}\right)\cdot\nabla\left(\frac{p_s^2}{n_s}\right)
\end{aligned} \tag{2.88}$$

For the last equality the identity $\nabla\cdot(\boldsymbol{G}\times\boldsymbol{H}) = (\nabla\times\boldsymbol{G})\cdot\boldsymbol{H} - (\nabla\times H)\cdot\boldsymbol{G}$ and that $\nabla\cdot\nabla g = 0$, for some function $g$, were utilised. Continuing with the heat flux it is noted that the expressions for the electron heat flux given in Eq. (2.49) greatly resembles the expressions of the frictional and thermal resistive drifts given in Eqs. (2.75) and (2.76) and when taking the mass ratio of ions and electrons into consideration meaning the heat flux can writen:

$$\begin{aligned}
\boldsymbol{q}_{\perp,e} &= \boldsymbol{q}_{\perp,u,e} + \boldsymbol{q}_{\perp,T,e} \\
&= -\frac{3}{2}p_e\boldsymbol{u}_{R,u,e} - \sum_\alpha p_e\left(\frac{13}{4} + \frac{\sqrt{2}}{Z_\alpha}\right)\frac{2}{3}\boldsymbol{u}_{R,T,\alpha\to e}.
\end{aligned} \tag{2.89}$$

Combining this with the resistive drift terms for electrons gives:

$$\begin{aligned}
&\frac{3}{2}\nabla\cdot(p_e\boldsymbol{u}_{R,e}) + p_e\nabla\cdot\boldsymbol{u}_{R,e} + \nabla\cdot\boldsymbol{q}_{\perp,e} - Q_e + \Big(\boldsymbol{u}_E + \boldsymbol{u}_{D,e}\Big)\cdot\boldsymbol{R}_e \\
=&\frac{5}{2}\nabla\cdot(p_e\boldsymbol{u}_{R,e}) - \cancel{\boldsymbol{u}_{R,e}\cdot\nabla p_e} + \nabla\cdot\boldsymbol{q}_{\perp,e} - Q_e + \frac{\boldsymbol{b}\times\nabla\phi}{B}\cdot\boldsymbol{R}_e + \cancel{\frac{\boldsymbol{b}\times\nabla p_e}{q_en_eB}\cdot\boldsymbol{R}_e} \\
=&\nabla\cdot(p_e\boldsymbol{u}_{R,e}) - \nabla\cdot\sum_\alpha p_e\left(1 + \frac{\sqrt{2}}{Z_\alpha}\right)\frac{2}{3}\boldsymbol{u}_{R,T,e} - Q_e + \boldsymbol{u}_{R,e}\cdot(q_en_e\nabla\phi).
\end{aligned} \tag{2.90}$$

Here it was used that $(\boldsymbol{G}\times\boldsymbol{H})\cdot\boldsymbol{J}=\boldsymbol{G}\cdot(\boldsymbol{H}\times\boldsymbol{J})$ to rewrite $\left(\boldsymbol{u}_E+\boldsymbol{u}_{D,e}\right)\cdot\boldsymbol{R}_e$. Following a similar procedure for the ions results in:

$$\begin{aligned}\frac{3}{2}\nabla\cdot(p_\alpha\boldsymbol{u}_{R,\alpha})+p_\alpha\nabla\cdot\boldsymbol{u}_{R,\alpha}-Q_\alpha+\left(\boldsymbol{u}_E+\boldsymbol{u}_{D,\alpha}\right)\cdot\boldsymbol{R}_\alpha&\\ =\frac{5}{2}\nabla\cdot\left(p_\alpha\boldsymbol{u}_{R,\alpha}\right)-Q_\alpha+\boldsymbol{u}_{R,\alpha}\cdot(q_\alpha n_\alpha\nabla\phi)&\end{aligned} \tag{2.91}$$

#### 2.2.3.2 Drift terms and their final form

The above rewrites made for some simpler expressions. Unfortunately, the drift versions of the moment equations are still not easily implementable. Hence appropriate approximations are sought in order to get a numerically implementable model. All drift terms are now considered individually, in the context in which they appear.

$E\times B$ **drift related terms** Starting with the main driver of the interchange instability in the form of the $\boldsymbol{E}\times\boldsymbol{B}$-drift yields

$$\begin{aligned}\nabla\cdot(n_\alpha\boldsymbol{u}_E)&=n_\alpha\nabla\cdot\left(\frac{\boldsymbol{b}\times\nabla\phi}{B}\right)+\boldsymbol{u}_E\cdot\nabla n_\alpha\\ &=\frac{d}{dt}n_\alpha+n_\alpha\mathcal{C}(\phi)\end{aligned} \tag{2.92}$$

Where

$$\mathcal{C}(f)\equiv\nabla\cdot\left(\frac{\boldsymbol{b}\times\nabla f}{b}\right) \tag{2.93}$$

is the curvature operator. The total derivative was given in Eq. (2.68). The main driver of transport is the electric field. Henceforth the total derivative will be evaluated using the $E\times B$ drift:

$$\frac{d}{dt}\approx\frac{\partial}{\partial t}+\boldsymbol{u}_E\cdot\nabla \tag{2.94}$$

the above expression can be combined with the temporal derivative of the density to yield:

$$\frac{\partial}{\partial t}n_\alpha+\nabla\cdot(n_\alpha\boldsymbol{u}_E)=\frac{d}{dt}n_\alpha+n_\alpha\mathcal{C}(\phi) \tag{2.95}$$

Performing the same procedure for the ion and electron pressure equation yields:

$$\frac{3}{2}\frac{\partial}{\partial t}p_s+\frac{3}{2}\nabla\cdot(p_s\boldsymbol{u}_E)+p_\alpha\nabla\cdot\boldsymbol{u}_E=\frac{3}{2}\frac{d}{dt}p_s+\frac{5}{2}p_\alpha\mathcal{C}(\phi) \tag{2.96}$$

This is not really an approximation, but rather the form of which it appears given the curvature operator.

**Diamagnetic drift** For the diamagnetic drift, the approach used with the electric drift wrt. the density equation in Eq. (2.92), is used here as well:

$$\nabla \cdot \left(n_s \boldsymbol{u}_{D,s}\right) = \nabla \cdot \left(n_s \frac{\boldsymbol{b} \times \nabla p_s}{q_\alpha n_s B}\right) = \nabla \cdot \left(\frac{\boldsymbol{b} \times \nabla p_s}{q_s B}\right) = \frac{1}{q_s}\mathcal{C}(p_s) \tag{2.97}$$

Since the above expression is the same for both electrons and ions, the resulting contribution to the vorticity equation becomes:

$$\sum_\alpha Z_\alpha \nabla \cdot \left(n_\alpha \boldsymbol{u}_{D,\alpha}\right) - \nabla \cdot \left(n_e \boldsymbol{u}_{D,e}\right) = \mathcal{C}\left(\sum_\alpha p_\alpha + p_e\right) \tag{2.98}$$

For the pressure equations it was seen in Eq. (2.88) that terms related to diamagnetic drift partly cancel each other. Using the vector identities $\nabla \cdot (\boldsymbol{A} \times \boldsymbol{B}) = (\nabla \times \boldsymbol{A}) \cdot \boldsymbol{B} - (\nabla \times \boldsymbol{B}) \cdot \boldsymbol{A}$ and that $\nabla \times (\nabla \phi) = 0$ this can be expressed in terms of the curvature operator:

$$\begin{aligned} &\frac{3}{2}\nabla \cdot p_s \boldsymbol{u}_{D,s} + p_s \nabla \cdot \boldsymbol{u}_{D,s} + \nabla \cdot \boldsymbol{q}_{\times,s} \\ &= \frac{5}{2}\nabla \times \left(\frac{\boldsymbol{b}}{q_s B}\right) \cdot \nabla \left(\frac{p_s^2}{n_\alpha}\right) = \frac{5}{2}\frac{1}{q_s}\mathcal{C}\left(\frac{p_s^2}{n_s}\right) \end{aligned} \tag{2.99}$$

This concludes the lowest order drift terms which are the main drivers of transport with the diamagnetic drift being instrumental in the creation of electric fields and the electric drift being the main driver of radial transport. What should be noted here is that all the terms, though reduced in form, contain the exact same physics as in Eq. (2.71).

**Polarisation related terms** For the next order drift, the polarisation terms is considered first along with the gyro-viscous terms. Since it is mass dependent the contribution to the electron pressure equation is negligible and hence dropped. The polarisation term is however of utmost importance as it allows for the calculation of the electric field through the vorticity equation. For the density equation the implication of the gyro-viscous cancellation was already discussed in which the remainder term in this is often neglected as it merely serves as a correction when the magnetic field is inhomogeneous [Madsen]:

$$\begin{aligned} &\nabla \cdot (n_\alpha \boldsymbol{u}_{p,\alpha}) + \nabla \cdot (n_\alpha \boldsymbol{u}_{\pi,gy}) \\ &\approx \nabla \cdot \left(\frac{n_\alpha}{\Omega_{c,\alpha}}\left(\frac{\partial}{\partial t} + \boldsymbol{u}_E \cdot \nabla\right)\left(\boldsymbol{u}_E + \boldsymbol{u}_{D,\alpha}\right)\right) \end{aligned} \tag{2.100}$$

Furthermore, this is approximated using the thin layer approximation, or Boussinesq approximation, where the density factor before the total derivative is linearised. This reason for doing this is to easy the numerical implementation in the vorticity equation. The result is:

$$\begin{aligned}&\nabla\cdot\Big(\frac{n_\alpha}{\Omega_{c,\alpha}}\left(\frac{\partial}{\partial t}+\boldsymbol{u}_E\cdot\nabla\right)\left(\boldsymbol{u}_E+\boldsymbol{u}_{D,\alpha}\right)\\ &\approx\frac{n_{\alpha,0}}{\Omega_{c,\alpha,0}}\nabla\cdot\left(\frac{\partial}{\partial t}+\boldsymbol{u}_{E,0}\cdot\nabla\right)\left(\boldsymbol{u}_{E,0}+\boldsymbol{u}_{D,\alpha,0}\right)\end{aligned}\tag{2.101}$$

Where $\boldsymbol{u}_{E,0}$ is the $E\times B$ drift evaluated at a constant reference magnetic field $B_0$. Likewise, the diamagnetic drift $\boldsymbol{u}_{D,\alpha,0}$ is evaluated using reference values $n_{\alpha,0}$ and $B_0$ in the denominator (see Eq. (2.71)). It is rather debatable whether the thin layer approximation is valid since there are rather steep gradients in the density in the outer mid-board region[60]. The ion pressure counterpart is formally small and is consequently neglected [17]. The pressure equations also contain the term $p_\alpha\nabla\cdot\boldsymbol{u}_{p,\alpha}$ which is approximated similarly Eq. (2.101), except the $p_\alpha$ factor is already outside the divergence. The result is:

$$p_\alpha\nabla\cdot\boldsymbol{u}_{p,\alpha}\approx\frac{p_\alpha}{\Omega_{c,\alpha,0}}\nabla\cdot\left(\frac{\partial}{\partial t}+\boldsymbol{u}_{E,0}\cdot\nabla\right)\left(\boldsymbol{u}_{E,0}+\boldsymbol{u}_{D,\alpha,0}\right)\tag{2.102}$$

**Resistive drift** The interaction between particles is assumed twofold. First, there is the electric field due to long-range interaction which is dealt with through the electric drift. Secondly, there are the short-range electric interactions which, as discussed earlier, closely resemble binary collisions. The resistive contributions to the equations will be dealt with here. The terms as they are now are rather cumbersome to work with and so appropriate approximations are needed. The first thing to note is that the thermal part of the resistive force partly cancels the temperature gradient part of the frictional resistive force:

$$\begin{aligned}\boldsymbol{u}_{R,s}&=-\sum_{s'}\frac{\nu_{s'\to s}}{m_s\Omega_{c,s}^2}\left(\frac{\nabla p_s}{n_s}-\frac{q_s}{q_{s'}}\frac{\nabla p_{s'}}{n_{s'}}\right)+\frac{3}{2}\sum_{s'}\frac{\nu_{s'\to s}}{m_s\Omega_{c,s}^2}\mu_{ss'}\left(\frac{\nabla T_s}{m_s}-\frac{q_s}{q_{s'}}\frac{\nabla T_{s'}}{m_{s'}}\right)\\ &=-\sum_{s'}\frac{\nu_{s'\to s}}{m_s\Omega_{c,s}^2}\left(n_s\frac{\nabla T_s}{n_s}-\frac{q_s}{q_{s'}}\frac{n_{s'}\nabla T_{s'}}{n_{s'}}\right)-\sum_{s'}\frac{\nu_{s'\to s}}{m_s\Omega_{c,s}^2}\left(T_s\frac{\nabla n_s}{n_s}-\frac{q_s}{q_{s'}}\frac{T_{s'}\nabla n_{s'}}{n_{s'}}\right)\\ &\quad+\frac{3}{2}\sum_{s'}\frac{\nu_{s'\to s}}{m_s\Omega_{c,s}^2}\mu_{ss'}\left(\frac{\nabla T_s}{m_s}-\frac{q_s}{q_{s'}}\frac{\nabla T_{s'}}{m_{s'}}\right)\approx-\sum_{s'}\frac{\nu_{s'\to s}}{m_s\Omega_{c,s}^2}\left(T_s\frac{\nabla n_s}{n_s}-\frac{q_s}{q_{s'}}\frac{T_{s'}\nabla n_{s'}}{n_{s'}}\right)\end{aligned}\tag{2.103}$$

To lessen the reading burden, a diffusion coefficient is introduced which is defined as

$$D_{s'\to s} = \rho_s^2 \nu_{s'\to s} = \frac{\nu_{s'\to s} v_{th,s}^2}{\Omega_{c,s}^2} \tag{2.104}$$

where $v_{th} = \sqrt{T_s/m_s}$ is the thermal speed and $\Omega = q_s B/m_s$ is the gyro frequency as mentioned earlier. Evaluating the collision frequency $\nu_{s'\to s}$ given in 2.30 at reference density $n_{s',0}$ and temperature $T_{s,s',0}$ and likewise for the thermal velocity and lastly the gyro frequency at $B_0$, the resistive drift can be approximated as:

$$\boldsymbol{u}_{R,s} \approx -\sum_{s'} \frac{D_{s'\to s,0} n_{s'}}{n_{s',0} T_{s,0}} \left( T_s \frac{\nabla n_s}{n_s} - \frac{q_s}{q_{s'}} T_{s'} \frac{\nabla n_{s'}}{n_{s'}} \right) \equiv \boldsymbol{u}_{R,s,0} \tag{2.105}$$

Inserting this into the the density equation gives:

$$\begin{aligned} \nabla \cdot \left( n_s \boldsymbol{u}_{R,s,0} \right) = -\sum_{s'} \frac{D_{s'\to s,0}}{n_{s',0} T_{s,0}} \Big( & T_s \nabla n_{s'} \cdot \nabla n_s + n_{s'} \nabla T_s \cdot \nabla n_s + T_s n_{s'} \nabla^2 n_s \\ & - \frac{Z_s}{Z_{s'}} \left[ T_{s'} \nabla n_s \cdot \nabla n_{s'} + n_s \nabla T_{s'} \cdot \nabla n_{s'} + T_{s'} n_s \nabla^2 n_{s'} \right] \Big), \end{aligned} \tag{2.106}$$

Multiplying by $Z_s$ it is, after some simple algebra, verified that $Z_s \nabla \cdot \left( n_s \boldsymbol{u}_{R,s,0} \right) = -Z_s' \nabla \cdot \left( n_s' \boldsymbol{u}_{R,s',0} \right)$. For the electron and ion pressure equation it was seen in Eq. (2.90) and Eq. (2.91) respectively how the resistive drift enters. Using the same approach as in the density equation it is found that:

$$\begin{aligned} \nabla \cdot \left( p_s \boldsymbol{u}_{R,s,0} \right) \approx \nabla \cdot T_{0,s} n_s \boldsymbol{u}_{R,s,0} = -\sum_{s'} \frac{D_{s'\to s,0}}{n_{s',0}} \\ \Big( T_s \nabla n_{s'} \cdot \nabla n_s + n_{s'} \nabla T_s \cdot \nabla n_s + T_s n_{s'} \nabla^2 n_s \\ - \frac{Z_s}{Z_{s'}} \left[ T_{s'} \nabla n_s \cdot \nabla n_{s'} + n_s \nabla T_{s'} \cdot \nabla n_{s'} + T_{s'} n_s \nabla^2 n_{s'} \right] \Big), \end{aligned} \tag{2.107}$$

And lastly

$$\begin{aligned} \boldsymbol{u}_{R,s} \cdot (q_s n_s \nabla \phi) \simeq \boldsymbol{u}_{R,s,0} \cdot (q_s n_s \nabla \phi) \\ = -\sum_{s'} \frac{D_{s'\to s,0}}{n_{s',0} T_{s,0}} \left( T_s n_{s'} \nabla n_s - \frac{q_s}{q_{s'}} T_{s'} n_s \nabla n_{s'} \right) \cdot (q_s \nabla \phi). \end{aligned} \tag{2.108}$$

**Viscosity** The last kind of drift is the viscosity drift. As noted in Eq. (2.51) this could be split into a collisional, gyro viscous and parallel part with the latter being neglected. Starting with the collisional drift the thin layer approximation approach is employed as was done with the polarisation equation to arrive at:

$$\nabla \cdot n_\alpha \boldsymbol{u}_{\pi,\perp,\alpha} \approx \sum_\beta \frac{n_{\alpha,0} D_{\pi,\beta\to\alpha,0}}{\Omega_{c,\alpha,0}} \nabla^2 \nabla^2 \left( \frac{\nabla \phi}{B_0} + \frac{\nabla p_\alpha}{q_\alpha n_{\alpha,0} B_0} \right), \tag{2.109}$$

Here a viscosity diffusion coefficient has been introduced which is defined as

$$\begin{aligned} D_{\pi,\beta\to\alpha,0} &\equiv \frac{\eta_{\perp,\beta\to\alpha,0}}{n_{\alpha,0} m_{\alpha,0}} \\ &= D_{\beta\to\alpha,0} \frac{m_\alpha m_\beta}{\left(m_\alpha + m_\beta\right)^2} \left( \frac{3}{10} \frac{m_\beta}{m_\alpha} + \frac{1}{2} - \frac{1}{5} \frac{m_\beta}{m_\alpha} \frac{Z_\alpha}{Z_\beta} \right). \end{aligned} \tag{2.110}$$

where the coefficient $\eta_{\perp,\beta\to\alpha,0}$ was defined in Eq. (2.55). Here it should be noted that when $\alpha = \beta$, the results is a factor two smaller than what is found in Braginskii[37]. The gyro viscous part in the density equations was partly cancelled due to the gyro-viscous cancellation with the polarisation drift as discussed in Section 2.2.3.2. The corresponding term in the pressure equation was also discussed, where it was argued that together with the polarisation drift it was negligible. The pressure term corresponding to Eq. (2.109) is formally small and so it is dropped[17]. The other ion pressure term containing the polarisation drift is given as:

$$p_\alpha \nabla \cdot \boldsymbol{u}_{\pi,\perp,\alpha} \approx p_\alpha \sum_\beta \frac{D_{\pi,\beta\to\alpha,0}}{\Omega_{c,\alpha,0}} \nabla^2 \nabla^2 \left( \frac{\nabla \phi}{B_0} + \frac{\nabla p_\alpha}{q_\alpha n_{\alpha,0} B_0} \right), \tag{2.111}$$

Lastly for the viscosity dependent terms are the dyadic product term $\boldsymbol{\pi}\, \boldsymbol{u}_{\alpha,0}$. For clarity, consider the lowest order drifts when the magnetic field is in the $z$-direction:

$$\boldsymbol{u}_{\alpha,0} = \frac{\boldsymbol{b} \times \phi}{B} + \frac{\boldsymbol{b} \times \phi}{q_\alpha n_\alpha B} = \frac{1}{B} \begin{pmatrix} -\partial_y \phi \\ \partial_x \phi \end{pmatrix} + \frac{1}{q_\alpha n_\alpha B} \begin{pmatrix} -\partial_y p_\alpha \\ \partial_x p_\alpha \end{pmatrix} \tag{2.112}$$

Inserting this into the pressure tensor when only considering the $x, y$ coordinates and approximating with $B_0$ and $n_0$ in the denominators, the perpendicular collisional part can be written:

$$\boldsymbol{\pi}_{\perp,\alpha} = -\eta_{\perp,\alpha} \begin{bmatrix} (\partial_x u_x - \partial_y u_y) & (\partial_x u_y + \partial_y u_x) \\ (\partial_x u_y + \partial_y u_x) & -(\partial_x u_x - \partial_y u_y) \end{bmatrix} \tag{2.113}$$

$$\approx -\eta_{\perp,\alpha} \begin{bmatrix} -2\frac{\partial_{xy}\phi}{B_0} - 2\frac{\partial_{xy} p_\alpha}{q_\alpha n_{\alpha,0} B_0} & \frac{(\partial_{xx} - \partial_{yy})\phi}{B_0} + \frac{(\partial_{xx} - \partial_{yy}) p_\alpha}{q_\alpha n_{\alpha,0} B_0} \\ \frac{(\partial_{xx} - \partial_{yy})\phi}{B_0} + \frac{(\partial_{xx} - \partial_{yy}) p_\alpha}{q_\alpha n_{\alpha,0} B_0} & 2\frac{\partial_{xy}\phi}{B_0} + 2\frac{\partial_{xy} p_\alpha}{q_\alpha n_{\alpha,0} B_0} \end{bmatrix} \tag{2.114}$$

Likewise for the gyro-viscous part one gets:

$$\boldsymbol{\pi}_{gy,\alpha} = -\eta_{\perp,\alpha}\left[\begin{array}{cc} (\partial_x u_y + \partial_y u_x) & -(\partial_x u_x - \partial_y u_y) \\ -(\partial_x u_x - \partial_y u_y) & -(\partial_x u_y + \partial_y u_x) \end{array}\right] \tag{2.115}$$

$$\approx -\eta_{\perp,\alpha}\left[\begin{array}{cc} \frac{(\partial_{xx}-\partial_{yy})\phi}{B_0} + \frac{(\partial_{xx}-\partial_{yy})p_\alpha}{q_\alpha n_{\alpha,0}B_0} & 2\frac{\partial_{xy}\phi}{B_0} + 2\frac{\partial_{xy}p_\alpha}{q_\alpha n_{\alpha,0}B_0} \\ 2\frac{\partial_{xy}\phi}{B_0} + 2\frac{\partial_{xy}p_\alpha}{q_\alpha n_{\alpha,0}B_0} & -\frac{(\partial_{xx}-\partial_{yy})\phi}{B_0} - \frac{(\partial_{xx}-\partial_{yy})p_\alpha}{q_\alpha n_{\alpha,0}B_0} \end{array}\right] \tag{2.116}$$

Taking the gradient of the lowest order drift velocities gives

$$\nabla \boldsymbol{u}_{\alpha,0} = \left[\begin{array}{cc} \partial_x u_{\alpha,0,x} & \partial_y u_{\alpha,0,x} \\ \partial_x u_{\alpha,0,y} & \partial_y u_{\alpha,0,y} \end{array}\right] \approx \left[\begin{array}{cc} -\left(\frac{\partial_{xy}\phi}{B_0} + \frac{\partial_{xy}p_\alpha}{q_\alpha n_{\alpha,0}B_0}\right) & -\left(\frac{\partial_{yy}\phi}{B_0} + \frac{\partial_{yy}p_\alpha}{q_\alpha n_{\alpha,0}B_0}\right) \\ \left(\frac{\partial_{xx}\phi}{B_0} + \frac{\partial_{xx}p_\alpha}{q_\alpha n_{\alpha,0}B_0}\right) & \left(\frac{\partial_{xy}\phi}{B_0} + \frac{\partial_{xy}p_\alpha}{q_\alpha n_{\alpha,0}B_0}\right) \end{array}\right] \tag{2.117}$$

Proceeding now to take the double dot, or dyadic, product[3] between the viscous tensor and the gradient of the velocity gives:

$$\boldsymbol{\pi}_{gy,\alpha} : \nabla \boldsymbol{u}_{\alpha,0} \approx -\eta_\alpha\left(\left[\frac{\partial_{xx}\phi}{B_0} + \frac{\partial_{xx}p_\alpha}{q_\alpha n_{\alpha,0}B_0} - \frac{\partial_{yy}\phi}{B_0} + \frac{\partial_{yy}p_\alpha}{q_\alpha n_{\alpha,0}B_0}\right]^2 \right.$$
$$\left. -4\left[\frac{\partial_{xy}\phi}{B_0} + \frac{\partial_{xy}p_\alpha}{q_\alpha n_{\alpha,0}B_0}\right]\right) \tag{2.118}$$

$$= -\sum_\beta m_\alpha n_{\alpha,0} D_{\pi,\beta\to\alpha,0}\left(\left[\frac{\partial_{xx}\phi}{B_0} + \frac{\partial_{xx}p_\alpha}{q_\alpha n_{\alpha,0}B_0} - \frac{\partial_{yy}\phi}{B_0} + \frac{\partial_{yy}p_\alpha}{q_\alpha n_{\alpha,0}B_0}\right]^2 \right.$$
$$\left. -4\left[\frac{\partial_{xy}\phi}{B_0} + \frac{\partial_{xy}p_\alpha}{q_\alpha n_{\alpha,0}B_0}\right]\right) \tag{2.119}$$

where in the last equality the definition of the viscous diffusion given in Eq. (2.110) was used.

**Heat Fluxes** The diamagnetic contribution to the ion heat flux, $\boldsymbol{q}_{s,\times}$, was already discussed in Section 2.2.3.2 resulting is a much more compact expression. Furthermore, in Eq. (2.90) it was seen for electrons how the resistive part of the heat flux could be combined with the electron resistive drift. The ion resistive heat flux given in Eq. (2.48) is approximated similar to all terms

---

[3] The definition of the double dot product is ambiguous and is often stated as either $\boldsymbol{A}:\boldsymbol{B} = a_{ij}b_{ji}$ or $\boldsymbol{A}:\boldsymbol{B} = a_{ij}b_{ij}$ where sum over indices are implied. For this work the latter is used, however it should be noted that for symmetric $\boldsymbol{A}$ or $\boldsymbol{B}$ the two are equivalent.

including collisions:

$$\begin{aligned}\nabla\cdot\boldsymbol{q}_{\perp,\alpha}=&\frac{p_\alpha}{m_\alpha^2\Omega_{c,\alpha}^2}\sum_\beta\mu_{\alpha\beta}\nu_{\beta\to\alpha}\left(\frac{3}{2}\left[\frac{\nabla p_\alpha}{n_\alpha}-\frac{Z_\alpha\nabla p_\beta}{Z_\beta n_\beta}\right]\right.\\&\left.-\frac{m_\alpha}{m_\alpha+m_\beta}\left[\left(\frac{13}{4}\frac{m_\beta}{m_\alpha}+4+\frac{15}{2}\frac{m_\alpha}{m_\beta}\right)\nabla T_\alpha-\frac{27}{4}\frac{Z_\alpha}{Z_\beta}\nabla T_\beta\right]\right).\end{aligned}\tag{2.120}$$

**Sources and Sinks** In Section 2.1.3 the sink and source terms $S_n$, $\boldsymbol{S}_u$ and $S_p$ were expressed in regards to the fundamental fluid variable sources $\Sigma_n$, $\boldsymbol{\Sigma}_u$ and $\Sigma$. The density and fluid velocity sources each contribute to $S_u$ and consequently also to the resulting source drift $\boldsymbol{u}_S$. Inserting it into the density equation yields

$$\begin{aligned}\nabla\cdot\left(n_s\boldsymbol{u}_{S_{u,s}}\right)&=-\nabla\cdot\left(n_s\frac{m_s\boldsymbol{b}\times\boldsymbol{S}_{u,s}}{q_sB}\right)\\&=-\nabla\cdot\left[\frac{m_s}{q_sB}\left(\left[\boldsymbol{b}\times\boldsymbol{u}_s'+\frac{\nabla\phi}{B}+\frac{\nabla p_s}{q_sn_sB}\right]\Sigma_{n,s}+n_s\boldsymbol{b}\times\boldsymbol{\Sigma}_{u,s}\right)\right]\\&\approx-\frac{m_s}{q_sB_0}\nabla\cdot\left(\left[\boldsymbol{b}\times\boldsymbol{u}_s'+\frac{\nabla\phi}{B_0}+\frac{\nabla p_s}{q_sn_{s,0}B_0}\right]\Sigma_{n,s}+n_s\boldsymbol{b}\times\boldsymbol{\Sigma}_{u,s}\right)\end{aligned}\tag{2.121}$$

Since there is a mass dependency, the term is neglected for electron density. The approximations used here, readily carries over to the vorticity equation. For the ion pressure equation the two terms containing the source drift are written as:

$$\begin{aligned}\nabla\cdot\left(p_s\boldsymbol{u}_{S_{u,s}}\right)&=-\nabla\cdot p_s\frac{m_s\boldsymbol{b}\times\boldsymbol{S}_{u,s}}{q_sB}\\&=-\nabla\cdot\left[\frac{m_s}{q_sB}\left(\left[\boldsymbol{b}\times\boldsymbol{u}_s'+\frac{\nabla\phi}{B}+\frac{\nabla p_s}{q_sn_sB}\right]T_s\Sigma_{n,s}+p_s\boldsymbol{b}\times\boldsymbol{\Sigma}_{u,s}\right)\right]\\&\approx-\frac{m_s}{q_sB_0}\nabla\cdot\left(\left[\boldsymbol{b}\times\boldsymbol{u}_s'+\frac{\nabla\phi}{B_0}+\frac{\nabla p_s}{q_sn_{s,0}B_0}\right]T_s\Sigma_{n,s}+p_s\boldsymbol{b}\times\boldsymbol{\Sigma}_{u,s}\right)\end{aligned}\tag{2.122}$$

and

$$\begin{aligned}
p_s \nabla \cdot \boldsymbol{u}_{S_{u,s}} &= -p_s \nabla \cdot \frac{m_s \boldsymbol{b} \times \boldsymbol{S}_{u,s}}{q_s B} \\
&= -p_s \nabla \cdot \left[ \frac{m_s}{q_s B} \left( \left[ \boldsymbol{b} \times \boldsymbol{u}_s' + \frac{\nabla \phi}{B} + \frac{\nabla p_s}{q_s n_s B} \right] \frac{\Sigma_{n,s}}{n_s} + \boldsymbol{b} \times \boldsymbol{\Sigma}_{u,s} \right) \right] \\
&\approx -\frac{m_s}{q_s B_0} \nabla \cdot \left( \left[ \boldsymbol{b} \times \boldsymbol{u}_s' + \frac{\nabla \phi}{B_0} + \frac{\nabla p_s}{q_s n_{s,0} B_0} \right] \frac{\Sigma_{n,s}}{n_s} + \boldsymbol{b} \times \boldsymbol{\Sigma}_{u,s} \right)
\end{aligned} \tag{2.123}$$

For the pressure equations there was also a general pressure source $S_p$ given in Eq. (2.63). In the implementation, the zeroth order velocities are used to evaluate the plasma fluid velocity giving

$$\begin{aligned}
S_p \approx& \frac{1}{2} m_s \left( \boldsymbol{u}_s' - \left[ \frac{\boldsymbol{b} \times \nabla \phi}{B} + \frac{\boldsymbol{b} \times \nabla p_s}{q_s n_s B} \right] \right)^2 \Sigma_{n,s} + \frac{3}{2} \left( T_s' \Sigma_{n,s} + n_s \Sigma_{T,s} \right) \\
=& \frac{1}{2} m_s \left( \boldsymbol{u}_s'^2 + \left( \frac{\nabla \phi}{B} + \frac{\nabla p_s}{q_s n_s B} \right)^2 - 2 \left( \frac{\boldsymbol{b} \times \nabla \phi}{B} + \frac{\boldsymbol{b} \times \nabla p_s}{q_s n_s B} \right) \cdot \boldsymbol{u}_s' \right) \Sigma_{n,s} \\
&+ \frac{3}{2} \left( T_s' \Sigma_{n,s} + n_s \Sigma_{T,s} \right)
\end{aligned} \tag{2.124}$$

where in the last equality it was used that $\boldsymbol{b} \cdot \nabla_\perp \phi = \boldsymbol{b} \cdot \nabla_\perp p_s = 0$ since only the perpendicular components are of interest.

**Neoclassical corrections** It has been found that the calculation of the collisional transport, exemplified in the viscosity and resistivity drifts which is due to coulomb collisions, underestimates the transport in tokamak plasmas. Due to the magnetic geometry of a tokamak, particles can follow a banana orbit trajectory within the plasma which severely increases the collisional effects of the plasma[11]. As a consequence the collisional diffusive transport is significantly increased. To account for the increased transport caused by diffusion, the diffusion coefficients are modified by Pfirsch-Schluter corrections in which a neoclassical correction is added to the classical diffusion coefficients in the form of [61]

$$D \to \left( 1 + \frac{R}{a} q_{95}^2 \right) D \tag{2.125}$$

where $q_{95}$ is the safety factor at the flux surface where 95% of the toroidal flux is enclosed. Depending on the magnetic field configuration, this can significantly increase the diffusive transport. It should be noted that the derivation of Pfirsch-Schluter corrections assume the magnetic field lines to be closed while this model concerns transport on both open and closed field lines. While a thorough derivation is beyond to scope of this work, it is expected that the same mechanism occurs on the open field lines at least to some extend as so the correction is applied equally here.

**Parallel parametrisation** The model so far has only dealt with a 2D slab geometry, meaning the parallel fluxes have been completely neglected. In order to remedy this the losses due to parallel transport are parametrised. Unfortunately the parallel expansion with multiple species is not well understood in regards to a tokamak plasma, and so for the time being an averaged approach will be used. For losses in the open field lines the implementation is in line with the HESEL[62] model which, in turn, follows the original ESEL model with cold ions[63]. In the single ion species case it has been found that plasmas filaments expand into vacuum at the sound speed $c_S = \sqrt{(T_e + T_i)/m_i}$[64]. This expansion acts as a sink on the filament, depleting it of particles. The parallel damping rate for the densities is then in the single species case:

$$\tau_n = \frac{L_b}{2Mc_S} \tag{2.126}$$

where $M$ is the Mach number and $L_b$ is the parallel blob size which is approximated to be:

$$L_b = \frac{2\pi q_{95} R}{6} \approx q_{95} R \tag{2.127}$$

Since the multi-species systems are the focus here, the single ion sound speed will be substituted with a common sound speed given by:

$$c_S = \sqrt{\frac{\sum_s n_s T_s}{m_s n_s}}. \tag{2.128}$$

This gives for the parallel loss term for the density equations

$$\frac{\partial}{\partial t} n_\alpha -= \frac{n_\alpha}{\tau_n}. \tag{2.129}$$

The vorticity is also affected by parallel loss mechanisms. This is in part due to parallel advection of the vorticity and is parametrised as:

$$\sum_\alpha \frac{n_{\alpha,0}}{\Omega_{c,\alpha,0}} \frac{\partial}{\partial t} \left( \frac{\nabla^2 \phi}{B} + \frac{\nabla^2 p_\alpha}{q_\alpha n_{\alpha,0} B_0} \right) -= \frac{1}{\tau_n} \sum_\alpha \frac{n_{\alpha,0}}{\Omega_{c,\alpha,0}} \left( \frac{\nabla^2 \phi}{B} + \frac{\nabla^2 p_\alpha}{q_\alpha n_{\alpha,0} B_0} \right) \tag{2.130}$$

Similarly the ion and electron pressure are advected in the parallel direction leading to loss. The resulting parametrisation is

$$\frac{3}{2}\frac{\partial}{\partial t}p_s -= \frac{9}{2}\frac{p_s}{\tau_n} \tag{2.131}$$

Lastly the pressure is also subject to parallel heat conduction. The electron parallel heat conduction due to currents is small due to quasi-neutrality. Conversely, parallel heat conduction due to thermal gradients is non-negligible. The size of the heat conduction depends on the mix of the ions and so here an effective charge approach will be used. The final parametrisation of the electron heat conduction on the open field lines is given by:

$$\nabla_{\parallel} \cdot \boldsymbol{q}_{e,T} \approx -\chi(Z_{\mathit{eff},0}) \frac{n_e T_e^{7/2}}{m_e \nu_{i_{\mathit{eff}} \to e,0} T_0^{3/2} L_c^2} \tag{2.132}$$

where $L_c$ is the parallel gradient scale, $\chi(Z_{\mathit{eff},0})$ is a Spitzer-Harm coefficient related to the electron thermal conductivity evaluated at reference values and $\nu_{i_{\mathit{eff}} \to e,0}$ is the collision frequency of the electrons with the effective ion mix also evaluated at reference values. $Z_{\mathit{eff}} = \sum_\alpha n_\alpha Z_\alpha^2 / n_e$. For $Z_{\mathit{eff},0} = \{1,2\}$ one gets $\chi(Z_{\mathit{eff},0}) = \{3.16, 4.9\}$.

On closed magnetic field lines there is also a parallel loss in the form of compression of the parallel current which is approximated by drift waves as follows [62]:

$$\frac{\partial}{\partial t} n_e -= \alpha \left( \tilde{T}_e + \frac{\bar{T}_e}{\bar{n}_e} \tilde{n}_e - e\tilde{\phi} \right) \tag{2.133}$$

$$\frac{\partial}{\partial t} p_e -= \alpha \bar{T}_e \left( \tilde{T}_e + \frac{\bar{T}_e}{\bar{n}_e} \tilde{n}_e - e\tilde{\phi} \right) \tag{2.134}$$

where the coefficient is given by[65]

$$\alpha = \frac{n_{e,0}}{\sigma_{\parallel}(Z_{\mathit{eff},0}) m_e \nu_{i_{\mathit{eff}} \to e,0} L_{\parallel}^2} \tag{2.135}$$

and $\sigma_{\parallel}(Z_{\mathit{eff},0})$ is the Spitzer-Harm coefficient related to electrical conductivity. For $Z_{\mathit{eff},0} = \{1,2\}$ one gets $\sigma_{\parallel} = \{0.51, 0.43\}$. $L_{\parallel}$ is the parallel ballooning length, and it typically set so $L_{\parallel} = L_b$ The contribution to the electron density equation readily carries over to the vorticity equation. The mean and fluctuation values are defined as follows:

$$\bar{f} = \frac{1}{L_y} \int_0^{L_y} f dy \tag{2.136}$$

$$\tilde{f} = f - \bar{f} \tag{2.137}$$

The Spitzer-Harm coefficients were first evaluated numerically in [66] while analytical expressions for any value of $Z$ are given in [33]. It should be noted that for the drift wave loss, only the electron density is explicitly affected. This is due to the assumption that the electrons due to their small mass contribute nearly exclusively to the current. The ions are implicitly affected as they are coupled to the electron density through the vorticity equation.

**Normalisation and the MIHESEL equations** All terms involved in the equations have now been derived and discussed. These can now be readily inserted into the density, vorticity and pressure equations Eqs. (2.80), (2.82), (2.83) and (2.86). Before writing down the full set of equations, it is instructive to normalise all the above expressions. The idea is to bring the scales of the equations into a comparable regime of order one and at the same time put them into a dimensionless form. The procedure for doing this is the gyro-Bohm normalisation:

$$\frac{T_s}{T_{e,0}} \rightarrow \breve{T}_s,\ \frac{\boldsymbol{x}}{\rho_{Ref}} \rightarrow \breve{\boldsymbol{x}},\ \Omega_{c,Ref,0}t \rightarrow \breve{t},\ \frac{q_{ref}\phi}{T_{e,0}} \rightarrow \breve{\phi},\ \frac{n_s}{n_{e,0}} \rightarrow \breve{n}_s, \tag{2.138}$$

where $\rho_{Ref} = \sqrt{T_{e,0}m_{Ref}/q_{Ref}^2B_0^2}$ is the reference larmor radius and $\Omega_{c,Ref,0} = q_{Ref}B_0/m_{Ref}$ the reference gyro frequency. Furthermore, constant parameters are normalised as:

$$m_s/m_{Ref} \rightarrow \mu_s,\ n_{s,0}/n_{e,0} \rightarrow a_s,\ T_{s,0}/T_{e,0} \rightarrow \tau_s \tag{2.139}$$

The procedure for normalising the equations is rather straight forward and only an illustrative glimpse will be given here. Starting with, e.g., the time derivative in the pressure equation one gets:

$$\frac{3}{2}\frac{\partial}{\partial t}p_s = \frac{3}{2}\omega_{Ref}n_{e,0}T_{e,0}\frac{\partial}{\partial \breve{t}}\breve{p}_s \tag{2.140}$$

For the curvature taking, e.g. the potential related term in the density equation, one gets:

$$\begin{aligned} n_s\mathcal{C}(\phi) &= -n_s\frac{\partial_y\phi}{B_0R} = -n_0\breve{n}_s\frac{T_{e,0}}{q_{Ref}\rho_{Ref}R_0B_0}\partial_{\breve{y}}\breve{\phi} \\ &= -n_0\Omega_{c,Ref}\breve{n}_s\frac{\rho_{Ref}}{R_0}\partial_{\breve{y}}\breve{\phi} = -n_0\Omega_{c,Ref}\breve{n}_s\kappa\partial_{\breve{y}}\breve{\phi} \end{aligned} \tag{2.141}$$

where $\kappa = \rho_{Ref}/R_0$ has been introduced as the curvature constant. This can be done for all terms in all equation and will result in a factor $\omega_{Ref}$ and either $n_{e,0}$ for density and vorticity or the $n_{e,0}T_{e,0}$ for the pressure equations.

From here on the breve $\breve{()}$ is dropped for simpler notation. Introducing the generalised potential

$$\phi_\alpha^* = \phi + \frac{p_\alpha}{Z_\alpha a_{\alpha,0}}, \tag{2.142}$$

dividing through with $\Omega_{c,Ref}$ and the appropriate field normalisation and setting reference values to one yields:

$$\begin{aligned}
&\frac{d}{dt} n_\alpha + n_\alpha \mathcal{C}(\phi) + \frac{1}{Z_\alpha}\mathcal{C}(p_\alpha) \\
&\qquad - a_\alpha \frac{\mu_\alpha}{Z_\alpha} \nabla \cdot \left( \frac{d^0}{dt} \nabla_\perp \phi_\alpha^* \right) = \Lambda_{n_\alpha}, && (2.143)\\
&\sum_\alpha a_\alpha \mu_\alpha \nabla \cdot \left( \frac{d^0}{dt} \nabla_\perp \phi_\alpha^* \right) - \mathcal{C}\left( \sum_\alpha p_\alpha + p_e \right) = \Lambda_w, && (2.144)\\
&\frac{3}{2}\frac{d}{dt} p_\alpha + \frac{5}{2} p_\alpha \mathcal{C}(\phi) + \frac{5}{2}\frac{1}{Z_\alpha}\mathcal{C}\left( \frac{p_\alpha^2}{n_\alpha} \right) \\
&\qquad - p_\alpha \frac{\mu_\alpha}{Z_\alpha} \nabla \cdot \left( \frac{d^0}{dt} \nabla_\perp \phi_\alpha^* \right) = \Lambda_{p_\alpha}, && (2.145)\\
&\frac{3}{2}\frac{d}{dt} p_e + \frac{5}{2} p_e \mathcal{C}(\phi) - \frac{5}{2}\mathcal{C}\left( \frac{p_e^2}{n_e} \right) = \Lambda_{p_e}. && (2.146)
\end{aligned}$$

And the right hand side which contain all interactions due to collisions are given by:

$$\begin{aligned}
\Lambda_{n_\alpha} =&\sum_s \frac{D_{s\to\alpha,0}}{a_s\tau_\alpha}\Big(T_\alpha\nabla n_s\cdot\nabla n_\alpha + n_s\nabla T_\alpha\cdot\nabla n_\alpha + T_\alpha n_s\nabla^2 n_\alpha \\
&-\frac{Z_\alpha}{Z_s}\Big[T_s\nabla n_\alpha\cdot\nabla n_s + n_\alpha\nabla T_s\cdot\nabla n_s + T_s n_\alpha\nabla^2 n_s\Big]\Big) \\
&-\sum_\beta \frac{a_\alpha D_{\pi,\beta\to\alpha,0}}{\Omega_{c,\alpha,0}}\nabla^2\nabla^2\phi^*_\alpha + \Xi_{n,\parallel} + S_{n_\alpha}, \qquad (2.147)\\
\Lambda_w =&\sum_\alpha\sum_\beta Z_\alpha\frac{a_\alpha D_{\pi,\beta\to\alpha,0}}{\Omega_{c,0,\alpha}}\nabla^2\nabla^2\phi^*_\alpha + \Xi_{w,\parallel} + S_w, \qquad (2.148)\\
\Lambda_{p_\alpha} =&\frac{5}{2}\sum_s \frac{D_{s\to\alpha,0}}{a_s}\Big(T_\alpha\nabla n_s\cdot\nabla n_\alpha + n_s\nabla T_\alpha\cdot\nabla n_\alpha + T_\alpha n_s\nabla^2 n_\alpha \\
&-\frac{Z_\alpha}{Z_s}\Big[T_s\nabla n_\alpha\cdot\nabla n_s + n_\alpha\nabla T_s\cdot\nabla n_s + T_s n_\alpha\nabla^2 n_s\Big]\Big) \\
&-p_\alpha\sum_\beta\frac{D_{\pi,\beta\to\alpha,0}}{\Omega_{c,\alpha,0}}\nabla^2\nabla^2\phi^*_\alpha - \sum_\beta\frac{D_{\beta\to\alpha,0}}{\mu_\alpha a_\beta}\mu_{\alpha\beta}\nabla\cdot\left(\frac{3}{2}\left[n_\beta\nabla p_\alpha - \frac{Z_\alpha}{Z_\beta}n_\alpha\nabla p_\beta\right]\right.\\
&\left.-\frac{\mu_\alpha}{\mu_\alpha+\mu_\beta}n_\alpha n_\beta\left[\left(\frac{13}{4}\frac{\mu_\beta}{\mu_\alpha}+4+\frac{15}{2}\frac{\mu_\alpha}{\mu_\beta}\right)\nabla T_\alpha - \frac{Z_\alpha}{Z_\beta}\frac{27}{4}\nabla T_\beta\right]\right)\\
&+\sum_s\frac{D_{s\to\alpha,0}}{a_s\tau_\alpha}\left(T_\alpha n_s\nabla n_\alpha - \frac{q_\alpha}{q_s}T_s n_\alpha\nabla n_s\right)\cdot\left(q_\alpha\nabla\phi\right)\\
&+\sum_\beta \mu_\alpha a_\alpha D_{\pi,\beta\to\alpha,0}\left[\left(\partial_x^2\phi^*_\alpha - \partial_y^2\phi^*_\alpha\right)^2 + 4\left(\partial_{xy}\phi^*_\alpha\right)^2\right]\\
&+\sum_s\frac{3n_\alpha n_s\nu_{s\to\alpha,0}\mu_\alpha\left(T_s - T_\alpha\right)}{a_s(\mu_\alpha+\mu_s)} + \Xi_{p_\alpha,\parallel} + S_{p_\alpha}, \qquad (2.149)\\
\Lambda_{p_e} =&\sum_s\frac{D_{s\to\alpha,0}}{a_s\tau_e}\Big(T_e\nabla n_s\cdot\nabla n_e + n_s\nabla T_e\cdot\nabla n_e + T_e n_s\nabla^2 n_e\\
&-\frac{Z_e}{Z_s}\Big[T_s\nabla n_e\cdot\nabla n_s + n_e\nabla T_s\cdot\nabla n_s + T_s n_e\nabla^2 n_s\Big]\Big)\\
&+\sum_\alpha\left(1+\frac{\sqrt{2}}{Z_\alpha}\right)D_{\alpha\to e,0}\nabla\cdot\left(n_e\nabla T_e\right)\\
&+\sum_s\frac{D_{s\to e,0}}{a_s\tau_e}\left(T_e n_s\nabla n_e - \frac{q_e}{q_s}T_s n_e\nabla n_s\right)\cdot\left(q_e\nabla\phi\right)\\
&+\sum_s\frac{3n_e n_s\nu_{s\to e,0}\mu_e\left(T_s-T_e\right)}{a_s(\mu_e+\mu_s)} + \Xi_{pe,\parallel} + S_{p_e}. \qquad (2.150)
\end{aligned}$$

where $\Xi_{f,\parallel}$ represents the parallel loss terms for a field $f$ with expressions given in Eqs. (2.129) to (2.134). Similarly, the $S_n$ terms are all expressions related to sources including drifts associated with sources as given in 2.121 2.122 2.123 2.124 as well as for whatever form $\Sigma_{n_\alpha}$. For the vorticity equation, the quasi-neutrality condition gives $\sum_\alpha Z_\alpha \Sigma_{n_\alpha} - \Sigma_{n_e} = 0$. Two forms of the total derivative were used which are given as

$$\frac{d}{dt} = \frac{\partial}{\partial t} + \frac{1}{B}\{\phi, \cdot\} \quad \text{and} \quad \frac{d^0}{dt} = \frac{\partial}{\partial t} + \{\phi, \cdot\}\,. \tag{2.151}$$

where the Poisson bracket was used, which is given as:

$$\{f, g\} \equiv \partial_x f \partial_y g - \partial_y f \partial_x g \tag{2.152}$$

#### 2.2.3.3 Summability of the MIHESEL model

One important aspect of the multispecies model is that it should converge to a single species model when multiple species are identical in mass, charge and temperature. I.e., taking a single ion species plasma and arbitrarily dividing it into two identical species should give the exact same result. For the MIHESEL equations this means that:

$$\sum_\alpha \left( \frac{\partial}{\partial t} n_\alpha + \nabla \cdot [n_\alpha \boldsymbol{u}_\alpha] \right) = \left( \frac{\partial}{\partial t} n_i + \nabla \cdot [n_i \boldsymbol{u}_i] \right) \tag{2.153}$$

where $\sum_\alpha n_\alpha = n_i$ and $\boldsymbol{u}_i$ are evaluated using $n_i$. The same goes for the pressure equation. However, the truncation involved in the drift expansion procedure appears to introduce an asymmetry that causes the above mentioned condition to not be met. Looking further into the drift it is found that the $E \times B$, diamagnetic and resistive drift all either add linearly in $n_\alpha$ or add to zero, leading to exact results. The polarisation on the other hand introduces non-linear addition of the density as seen in the following:

$$\begin{aligned} \sum_\alpha \nabla \cdot n_\alpha \boldsymbol{u}_{p,\alpha} &= \sum_\alpha \nabla \cdot \left( \frac{n_\alpha}{\Omega_{c,\alpha}} \boldsymbol{b} \times \frac{d}{dt} \left( \frac{\boldsymbol{b} \times \nabla \phi}{B} + \frac{\boldsymbol{b} \times \nabla p_\alpha}{q_\alpha n_\alpha B} \right) \right) \\ &\neq \nabla \cdot \left( \frac{\sum_\alpha n_\alpha}{\Omega_{c,\alpha}} \boldsymbol{b} \times \frac{d}{dt} \left( \frac{\boldsymbol{b} \times \nabla \phi}{B} + \frac{\boldsymbol{b} \times \nabla p_i}{\sum_\alpha q_\alpha n_i B} \right) \right) \end{aligned} \tag{2.154}$$

where $n_i = \sum_\alpha n_\alpha$. The non-linearity in $n_\alpha$ is as a consequence of the inclusion of the diamagnetic drift as a lowest-order drift. However, this is debatable as such a drift is inherently charge separating at this order. This potentially violates the quasi-neutrality condition. Similarly, the expression for the perpendicular collisional part of the stress tensor evaluated at $\boldsymbol{u}_{0,\alpha}$ is non-linear. Overall the result is that the density equation does not sum up in a way that makes it possible to arbitrarily split a species, solve the system as a multi-species system and still get the same overall result. Fortunately, a number of the approximations were employed which linearised the equations in such that the density equation sum up as expected. However, the $p_\alpha \nabla \cdot \left( \boldsymbol{u}_{p,\alpha} + \boldsymbol{u}_{\pi,\perp} \right)$ still retain the non-linearity in density under summation. Fortunately, the terms are higher-order and so are in numerical experiments found to be small. More generally, consider a single species being split as:

$$n_\alpha(x,y,t=0) = f_\alpha(x,y) n_i(x,y,t=0), \quad \sum_\alpha f_\alpha(x,y) = 1 \tag{2.155}$$

where $f_\alpha(x,y)$ is some function describing the splitting. If $f_\alpha(x,y) = const$, the ratio of the species is a constant in space, and so the density and ion pressure equations add as required. It is only in the cases where it is not a constant that the non-addibility of the equations is present. It should also be noted that the resistive force, in general, seeks to homogenise the density ratio over space, further reducing the problem, unless there is a constant source such that counteracts this. Furthermore, the drift fluid expansion, which is a rather fundamental expansion in plasma physics, contains an inconsistency in that the diamagnetic drift with this ordering should lead to charge separation. This is in contrast to the quasi-neutrality condition. Thus the inclusion of the diamagnetic term as a lowest-order is questionable [67]. While this is an inconsistency in the approach, the terms that supply the inconsistency are higher-order terms meaning their contribution is small. Furthermore, the resistive forces between ion species act to equilibrate the ion density ratios over all space. Hence the separation in ion species is small and therefore negligible.

## 2.3 Section conclusion - current issues and ideas for future implementations

In the previous sections, the derivation of the fluid equations from the single-particle Boltzmann equation was discussed. Concerning this, it was clear that a closure was needed to obtain a solvable set of equations. For this work, the Zhdanov closure was used, which is based on Grad's moment method, which was originally used for dilute gasses, but easily generalises to charged particles. In this context, the Zhdanov closure used a 21-moment method to obtain accurate representations of the physical quantities. However, this closure was limited to only deal with similar ion temperatures $\|T_\alpha - T_\beta\| \ll T_\alpha$. In future work, this should be expanded upon such that temperature limits are not as strict. This will be useful when studying, e.g., heating by ion cyclotron resonance heating (ICRH) where the heating is dominated by transfer at the resonance frequency. This means that a main ion will be heated by the ICRH whereas other species will be predominantly heated by collisions. This is possible to investigate as the model is now provided that the ICRH heating is significantly slower than the collisional heat exchange. In such a case, the temperatures will equilibrate faster than the heated species heats up. In regards to neutrals, they are typically much colder than the plasma, and so when they are ionized they start at a lower temperature, meaning the MIHESEL model is not well suited for such cases. To overcome the temperature limitation, a thorough mathematical derivation of the 21-moment method should be done without the limitation. Some work has been done to get exact expressions for an arbitrary number of moments with arbitrary temperatures [43], [68], [69]. This could serve as a starting for the studies.

Furthermore, the drift fluid expansion presented an adding problem when there are more than two species. The problem was that the terms involving polarisation and collisional viscosity do not add in such a way that a single species could be described as an arbitrarily split two or more species plasma. It was noted that the main cause of the problem was the inclusion of the diamagnetic drift in the lowest order drift, which in turn is due to steep gradient in the edge/SOL region. However, there is an inconsistency in this as it is a charge separating drift and the derivation is hinged on the quasi-neutrality condition which might be violated in such a case. How the splitting problem can be overcome should be something that is considered for future studies.

In the parametrisation of the parallel dynamics, a common averaged approach was used by, e.g., using a common sound speed. In this regard it would be preferable to do more work on multi-species plasma expansion in a vacuum in order to obtain a more accurate parametrisation. Starting studies could/should involve [70]–[72].

Lastly, the model was derived as an extension of the HESEL model along with many of the same approximations, such as the Boussinesq approximation. This was in large part due to numerical convenience. It would be interesting to test the effect of the approximation compared to the full model.

In the next chapter, the numerical implementation of the model is presented along with the numerical framework used to solve them. In chapter 4, the equations are employed to study both seeded blobs and turbulent transport.

# Chapter 3

# Numerical implementation

In the previous section, the theoretical derivation of the MIHESEL model was presented. Based on the Boltzmann equations, the moment equations were derived to develop a reduced fluid model that could be used to study turbulent transport. However, providing an analytical solution to the MIHESEL equations is close to impossible. As such, the system of equations is cast as an initial value problem, which allows for performing numerical simulations to obtain a solution. In this section, the tools used to solve the equations will be presented. This includes the numerical library that is used, the spatial discretisation, linear and non-linear solvers and time integration schemes. The time integration and non-linear solver are the main contributions to the library as a result of this work. Furthermore, for the MIHESEL equations stated in Eqs. (2.143) to (2.146) the vorticity and ion pressure equations are coupled in the time derivative. This means that to solve the problem, the equations have to cast in a numerically suitable way.

## 3.1 Numerical implementation of MIHESEL

In this section, the numerical implementation of the MIHESEL equations is discussed. This in particular, concerns dealing with the coupling of the potential and ion pressure.

### 3.1.1 Symmetrise linear problem

The right hand side op the MIHESEL equations (Eqs. (2.143) to (2.146)) are easily implemented as they all contain 'known' variables. The left hand side however, contains unknown variables, namely $\partial_t n_\alpha, \partial_t \phi, \partial p_\alpha$ and $\partial_t p_e$ which are all needed to integrate the equations in time. What complicates matters is the coupling between the variables, and in particular the potential and ion pressure. To illustrate the dependence, it is instructive to write the equations in matrix from:

$$\begin{pmatrix}
1 & 0 & \cdots & -a_1\frac{\mu_1}{Z_1}\nabla^2 & -\frac{\mu_1}{Z_1^2}\nabla^2 & 0 & \cdots & 0 \\
0 & 1 & \cdots & -a_2\frac{\mu_2}{Z_2}\nabla^2 & 0 & -\frac{\mu_2}{Z_2^2}\nabla^2 & \ddots & 0 \\
\vdots & \ddots & \ddots & \vdots & \vdots & \ddots & \ddots & 0 \\
0 & 0 & 0 & \sum_\alpha a_\alpha \mu_\alpha \nabla^2 & \frac{\mu_1}{Z_1}\nabla^2 & \frac{\mu_2}{Z_2}\nabla^2 & \cdots & 0 \\
0 & 0 & 0 & -p_1\frac{\mu_1}{Z_1}\nabla^2 & \frac{3}{2} - p_1\frac{\mu_1}{Z_1^2 a_1}\nabla^2 & 0 & \cdots & 0 \\
0 & 0 & 0 & -p_2\frac{\mu_2}{Z_2}\nabla^2 & 0 & \frac{3}{2} - p_2\frac{\mu_2}{Z_2^2 a_2}\nabla^2 & \ddots & 0 \\
\vdots & \vdots & \vdots & \vdots & \vdots & \ddots & \ddots & 0 \\
0 & 0 & 0 & 0 & 0 & 0 & 0 & \frac{3}{2}
\end{pmatrix} \cdot \begin{pmatrix}
\frac{\partial}{\partial t} n_1 \\
\frac{\partial}{\partial t} n_2 \\
\vdots \\
\frac{\partial}{\partial t} \phi \\
\frac{\partial}{\partial t} p_1 \\
\frac{\partial}{\partial t} p_2 \\
\vdots \\
\frac{\partial}{\partial t} p_e
\end{pmatrix}$$

$$= \begin{pmatrix}
\Lambda_{n_1} - n_1\mathcal{C}(\phi) - \frac{1}{Z_1}\mathcal{C}(p_1) + a_1\frac{\mu_1}{Z_1}\nabla\cdot\{\phi, \nabla_\perp \phi_1^*\} \\
\Lambda_{n_2} - n_2\mathcal{C}(\phi) - \frac{1}{Z_2}\mathcal{C}(p_2) + a_1\frac{\mu_2}{Z_2}\nabla\cdot\{\phi, \nabla_\perp \phi_2^*\} \\
\vdots \\
\left(\Lambda_w + \mathcal{C}\left(\sum_\alpha p_\alpha + p_e\right) - \sum_\alpha a_\alpha \mu_\alpha \nabla\cdot\{\phi, \nabla_\perp \phi_\alpha^*\}\right) \\
\left(\Lambda_{p_1} - \frac{5}{2}p_1\mathcal{C}(\phi) - \frac{5}{2}\frac{1}{Z_1}\mathcal{C}\left(\frac{p_1^2}{n_1}\right) + p_1\frac{\mu_1}{Z_1}\nabla\cdot\{\phi, \nabla_\perp \phi_1^*\}\right) \\
\left(\Lambda_{p_2} - \frac{5}{2}p_2\mathcal{C}(\phi) - \frac{5}{2}\frac{1}{Z_2}\mathcal{C}\left(\frac{p_2^2}{n_2}\right) + p_2\frac{\mu_2}{Z_2}\nabla\cdot\{\phi, \nabla_\perp \phi_2^*\}\right) \\
\vdots \\
\left(\Lambda_{p_e} - \frac{5}{2}p_e\mathcal{C}(\phi) + \frac{5}{2}\mathcal{C}\left(\frac{p_e^2}{n_e}\right)\right)
\end{pmatrix} \tag{3.1}$$

Given that the right hand side is known, the above system becomes a Helmholtz type linear system of equation that needs to be solved for the temporal derivatives $\partial_t$. An exact general solution to this linear system is not possible to obtain, hence it needs to solved numerically and for this work it is done iteratively. It is first noted that the density part is coupled with pressure and potential but not the other way around. Furthermore, the electron pressure is not coupled to anything in $\partial_t p_e$ and so is easy to evaluate. This leaves the potential and ion pressure part of the matrix. Since these are independent of $n_\alpha$ and $p_e$ the focus is on that square *asymmetric* sub-matrix. The numerical library that is used in this work solves linear problems using the conjugate gradient method. This is further discussed in Section 3.2.4. This method only works for symmetric positive definite problems [73]. Hence the aforementioned sub-matrix need to be symmetrised. This is done by dividing the pressure equations with $p_\alpha$ and change the sign of the vorticity equation. The final result is:

$$\begin{pmatrix} -\sum_\alpha a_\alpha \mu_\alpha \nabla^2 & -\frac{\mu_1}{Z_1}\nabla^2 & -\frac{\mu_2}{Z_2}\nabla^2 & \cdots \\ -\frac{\mu_1}{Z_1}\nabla^2 & \frac{3}{2}\frac{1}{p_1} - \frac{\mu_1}{Z_1^2 a_1}\nabla^2 & 0 & \\ -\frac{\mu_2}{Z_2}\nabla^2 & 0 & \frac{3}{2}\frac{1}{p_2} - \frac{\mu_2}{Z_2^2 a_2}\nabla^2 & \\ \vdots & & & \ddots \end{pmatrix} \cdot \begin{pmatrix} \partial_t \phi \\ \partial_t p_1 \\ \partial_t p_2 \\ \vdots \end{pmatrix}$$

$$= \begin{pmatrix} -\left(\Lambda_w + \mathcal{C}\left(\sum_\alpha p_\alpha + p_e\right) - \sum_\alpha a_\alpha \mu_\alpha \nabla \cdot \{\phi, \nabla_\perp \phi_\alpha^*\}\right) \\ \left(\Lambda_{p_1} - \frac{5}{2} p_1 \mathcal{C}(\phi) - \frac{5}{2}\frac{1}{Z_1}\mathcal{C}\left(\frac{p_1^2}{n_1}\right) + p_1 \frac{\mu_1}{Z_1}\nabla \cdot \{\phi, \nabla_\perp \phi_1^*\}\right)/p_1 \\ \left(\Lambda_{p_2} - \frac{5}{2} p_2 \mathcal{C}(\phi) - \frac{5}{2}\frac{1}{Z_2}\mathcal{C}\left(\frac{p_2^2}{n_2}\right) + p_2 \frac{\mu_2}{Z_2}\nabla \cdot \{\phi, \nabla_\perp \phi_2^*\}\right)/p_2 \\ \vdots \end{pmatrix} \tag{3.2}$$

As mentioned the conjugate gradient works with symmetric positive definite matrices. The above matrix is symmetric, and since the negative Laplacian is positive definite and the factor $\frac{3}{2}p_\alpha^{-1}$ means a diagonal of positive values which is positive definite, the matrix as a whole is symmetric positive definite and so solvable by the conjugate gradient method. To solve the MIHESEL equations one then proceeds by first solving the above system (Eq. (3.2)) for $\partial_t \phi$ and $\partial_t p_\alpha$ respectively and subsequently solve the density for $\partial_t$ by substitution of the corresponding pressure equation. Solving for $\partial_t p_e$ is done by evaluating the right-hand side. The inversion is performed for each call to the MIHESEL equations. The amount of time they are evaluated depends on the type of time integration scheme that is used. This is discussed in Section 3.2.5. The inversion is performed for each iteration in the nonlinear solver Section 3.2.5. In this is regard is it worth noting that the convergence of the matrix inversion is secondary to the convergence of the nonlinear solver as we are interested in the new state of the system and not explicitly the new $\partial_t \cdot$. Naturally, the convergence of the nonlinear solver is dependent on the convergence of the matrix inversion. However, high tolerances are not necessary for the matrix inversion in order to achieve an accurate result in the nonlinear solver. In general, it is noted that the number of iterations in the nonlinear solver increases as the tolerance of the linear solver is reduced. However, reaching a high tolerance in the linear solver can be very expensive, meaning it is often beneficial to set a low tolerance at the cost of more nonlinear iterations in order to achieve a shorter run time.

## 3.2 Spatial discretisation and numerical library

There are a variety of methods for discretizing the spatial domain each with its strengths and weaknesses. These include, but are not limited to, the finite difference, finite volume, finite element or discontinuous Galerkin method. For this work, the choice of a numerical library falls on the discontinuous Galerkin library FELTOR[28] which, as the name suggests, uses the discontinuous Galerkin discretisation method. The choice of this library was due to its ability to easily invert coupled linear equations and adaptiveness in the number of equations which grows when more species are added. This is especially important as the number of ion species can be set arbitrarily.

### 3.2.1 Feltor library

FELTOR is an open-source library/framework developed at the University of Innsbruck and subsequently the Technical University of Denmark for solving problems in plasma physics[1]. It is designed for easy implementation and time integration of partial differential equations without the need for advanced knowledge of numerical methods. The library is written in `C++`, is used as a header-only library and can be run in parallel using either openMP or CUDA together with MPI. This allows for utilisation of a wide range of hardware, such as Skylake nodes and NVIDIA GPUs, which in turn allows for fast execution of simulations. Also, the FELTOR library comes with parallelised implementations of all the necessary basic linear algebra routines, including scalar-vector, vector-vector and matrix-vector operations. This makes it straight forward to implement new parallel routines. In general, to avoid heavy memory usage, there is an emphasis on matrix-free methods, i.e. methods where only the matrix-vector product is needed. In regards to linear solvers, many Krylov subspace methods, such as the conjugate gradient method, have this feature. This also means that implementing new physics models in parallel is straight forward when using the implemented classes.

### 3.2.2 Discontinuous Galerkin

A brief overview of the discretisation method employed by the FELTOR library and how differential operators are constructed will now be presented following the outline of [74], [75]. The general aim of discretisation methods is to represent some function using a discrete number of (weighted) points. In this regard, it should be noted that this implementation is for structured

---

[1] The code can be obtained from https://github.com/feltor-dev/feltor

grids only. The main idea of the discontinuous Galerkin method is to divide a domain into small subdomains, or cells, and expand a function through a set of orthogonal functions on each cell:

$$f_n(x) = \sum_{k=0}^{k-1} a_k P_k(x) \tag{3.3}$$

where $a_k$ is some coefficient and $P_k$ is some polynomial of degree $k$ and $f_n(x)$ the function $f(x)$ on cell $n$. It is important to note that the function $f_n(x)$ is zero outside the cell. This is then used to approximate the function $f(x)$ on the whole domain with a finite sum of these functions:

$$f(x) = \sum_{n=1}^{N} f_n(x) \tag{3.4}$$

Take, e.g., a 1D grid of length $l_x$ with $N_x$ cells with equal grid spacing $h_x$. The cells are defined on the interval [76]:

$$I_{n_x} = \{(x) : x \in \left[x_{n_x-1/2}, x_{n_x+1/2}\right]\} \tag{3.5}$$

with $n_x \in [1, N_x]$. For $n_x = 1, N_x$ this gives $x_{1-1/2} = 0$ and $x_{N_x+1/2} = l_x$. The idea is now to form basis functions of polynomials on these cells. The space of polynomials is defined as:

$$V_h^p = \{v : v|_{I_{n_x}} \in P_p; 1 \leq n_x \leq N_x\} \tag{3.6}$$

Where $P_p(I_{n_x})$ is the set of polynomials on the space $I_{n_x}$.

The polynomials are not unique, and a wide range of choices are available[77]. The choice of polynomial basis for this library is the orthogonal Legendre polynomials which are recursively defined on an interval $[-1, 1]$ through

$$(p+1)P_{p+1}(x) = (2p+1)xP_p(x) - pP_{p-1}(x) \tag{3.7}$$

with $P_0 = 1$, $P_1 = x$, and $p$ the degree of the polynomial. The inner product of two polynomials can be given exactly[78]. For the Legendre polynomials using the Gauss-Legendre quadrature on the interval $[-1, 1]$ gives:

$$\int_{-1}^{1} P_n(x)P_m(x)\mathrm{d}x = \sum_{j=0}^{p} w_j P_n(x_j^a) P_m(x_j^a) = \frac{p}{2p+1}\delta_{nm} \tag{3.8}$$

where $w_j$ and $x_a^j$ denote the Gauss-Legendre weights and abscissas. The weights are given by

$$w_j = \frac{2}{(1-x_j^2)\left[P_p'(x_j)\right]^2} \tag{3.9}$$

and the corresponding abscissas are given by the roots of the of the polynomials $P_p$ which are symmetric around $x = 0$. The polynomials are also complete meaning that:

$$\sum_{n=0}^{\infty} \frac{2n+1}{2} P_n(x) P_n(x') = \delta(x' - x) \tag{3.10}$$

which in discrete form is given as:

$$\sum_{n=0}^{p} \frac{2n+1}{2} \omega_j P_n(x_i^a) P_n(x_j^a) = \delta_{ij} \tag{3.11}$$

A function can now be expressed in spectral space in discrete form as:

$$\bar{f}^p \equiv \frac{2p+1}{2} \sum_{j=0}^{p} w_j P_p(x_j^a) f(x_j^a) \tag{3.12}$$

where $f(x)$ with $x \in [-1,1]$ is some real function. This gives a (forward) transformation operator from physical space to spectral space [74], [78]:

$$F_{nj} \equiv \frac{2n+1}{2} w_j P_n(x_j^a) \tag{3.13}$$

A (backward) transformation operator, $B_{in}$ from spectral space to physical space can be found by requiring the product of the forward and backward transformation to be unitary $\sum_{k=0}^{p} B_{ik} F_{kj} = \delta_{ij}$. Using the discrete completeness (Eq. (3.11)) this gives:

$$B_{in} = P_n(x_i^a) \tag{3.14}$$

The unitarity property gives:

$$f(x_i^a) = \sum_{n=0}^{p} \sum_{j=0}^{p} B_{in} F_{nj} f(x_j^a) \tag{3.15}$$

So far, only the interval $[-1,1]$ has been considered. Naturally it is beneficial to extend this to an arbitrary interval $[a,b]$. As mentioned earlier, the domain can be split into $N$ equidistant grid. This means the results can readily be applied on the function representation to the $n'th$ cell where $x_{nj}^a \equiv x_n + \frac{h}{2} x_j^a$ with $x_n$ being the cell center and $h = (b-a)/N$. An approximation $f_h(x)$ of a function $f(x)$ on $[a,b]$ can be then expressed as:

$$f_h(x) = \sum_{n=1}^{N} \sum_{k=0}^{p} \bar{f}^{nk} P_{nk}(x) \tag{3.16}$$

where $\bar{f}^{nk}$ is given by Eq. (3.12) with $f_{nj} = f(x^a_{nj})$ and the polynomials have been shifted such that

$$P_{nk}(x) = \begin{cases} P_k\left(\frac{2}{h}(x - x_n)\right), & x - x_n \in \left[\frac{-h}{2}, \frac{h}{2}\right] \\ 0, & \text{otherwise} \end{cases} \tag{3.17}$$

This is the discontinuous Galerkin expansion. Here it should be noted that since the expansions are made on each cell, the boundaries of the expansion in the given cell and the adjacent cell do not necessarily coincide resulting in discontinuities. Hence the name of the method. Since an aim of the library is to numerically solve partial differential equations, there is a natural need for differential operators. A problem here is that the cell boundaries do not have a well defined value and so a choice needs to be made about the numerical flux across the boundaries. Three options are available, the forward, backward and centered:

$$\hat{f}_B(x) = \lim_{\epsilon \to 0, \epsilon > 0} f_h(x - \epsilon) \tag{3.18}$$

$$\hat{f}_C(x) = \frac{1}{2}\left(\hat{f}_B(x) + \hat{f}_F(x)\right) \tag{3.19}$$

$$\hat{f}_F(x) = \lim_{\epsilon \to 0, \epsilon > 0} f_h(x + \epsilon) \tag{3.20}$$

In regards to boundary conditions on the domain on the whole domain, there is the choice of Dirichlet, Neumann and periodic. For Dirichlet it is assumed that $\hat{f}(a) = \hat{f}(b) = 0$ on the boundary while for Neumann it is assumed that $\hat{f}(a) = \lim_{\epsilon \to 0, \epsilon > 0} f_h(a + \epsilon)$ and $\hat{f}(b) = \lim_{\epsilon \to 0, \epsilon > 0} f_h(b) - \epsilon)$. For both cases this means some care has to be taken when the boundary-values are non-zero. Lastly, periodic boundaries assume $\hat{f}(a - \epsilon) = \lim_{\epsilon \to 0, \epsilon > 0} f_h(b - \epsilon)$ and $\hat{f}(a + \epsilon) = \lim_{\epsilon \to 0, \epsilon > 0} f_h(b + \epsilon)$. For the derivative, the centered flux is discussed as this is what is used in the numerical implementation of the MIHESEL equations. The derivative in the spectral space, derived in weak formulation [74], is given as:

$$\bar{\boldsymbol{f}}_x = (\mathbf{1} \otimes T) \circ \bar{D}^{cen}_{x,\substack{Neu\\Per\\Dir}} \bar{\boldsymbol{f}} \tag{3.21}$$

with the centered differential operator given as

$$\bar{D}_{x,\substack{Neu\\Per\\Dir}} = \frac{1}{2}\begin{pmatrix} \substack{M-M^T-L\\ M-M^T \\ M-M^T+L} & RL & 0 & & \substack{0\\ -LR\\ 0} \\ -LR & M-M^T & RL & & \\ 0 & -LR & \ddots & \ddots & \\ & & \ddots & & RL \\ \substack{0\\ RL\\ 0} & & & -LR & \substack{M-M^T+R\\ M-M^T\\ M-M^T-R} \end{pmatrix} \tag{3.22}$$

where the Neumann operator corresponds to the upper expressions in the corners, the periodic corresponds to the middle and the Dirichlet to the bottom expressions in the corners. All non-corner entries are the same for all boundary conditions. The operators in Eq. (3.22) are given as

$$T_{ij} = \frac{2i+1}{h}\delta_{ij} \tag{3.23}$$

$$M_{ij} = \begin{cases} 1-(-1)^{i+j}, & i \leq (j-1) \\ 0, & \text{else} \end{cases} \tag{3.24}$$

$$R_{ij} = 1 \tag{3.25}$$

$$L_{ij} = (-1)^{i+j} \tag{3.26}$$

$$RL_{ij} = (-1)^{j} \tag{3.27}$$

$$LR_{ij} = (-1)^{i} \tag{3.28}$$

The indices are such that $i, j = 0, ..p$. The derivative in physical space is given as:

$$\boldsymbol{f}_x = (\mathbf{1} \otimes V) \circ D^{cen}_{x,\substack{Neu\\Per\\Dir}} \boldsymbol{f} \tag{3.29}$$

where the differential operator is

$$D^{cen}_{x,\substack{Neu\\Per\\Dir}} = \left(1 \otimes F^T\right) \circ \bar{D}^{cen}_{x,\substack{Neu\\Per\\Dir}} \circ (\mathbf{1} \otimes F) \tag{3.30}$$

with

$$F = TB^T W \tag{3.31}$$

$$T_{ij} = \frac{2i+1}{h}\delta_{ij} \tag{3.32}$$

$$W_{ij} = \frac{hw_j}{2}\delta_{ij} \tag{3.33}$$

$$V_{ij} = W_{ij}^{-1} \tag{3.34}$$

and $B$ was the backward transformation matrix defined in Eq. (3.14). Again the indices are $i,j = 0,...,p$. This concludes the first derivatives.

A typical problem in partial differential equations is solving the (general) elliptic equation:

$$-\frac{\partial}{\partial x}\left(\chi(x)\frac{\partial}{\partial x}\phi(x)\right) = \rho(x) \tag{3.35}$$

For the MIHESEL equations, a similar term is associated with finding the potential and ion pressure, which will be discussed in detail in Section 3.1. Before the elliptic equation can be solved, it is necessary to obtain a discretisation of the operator. This is given as:

$$\rho = (\mathbf{1}\otimes V)\left[D_x^T \circ \chi \circ (\mathbf{1}\otimes V)\circ D_x + \alpha J\right]\phi \tag{3.36}$$

At a first glance this is simply the successive application of the first derivative differentiation operator. However, the successive application of the first derivative does not convergence for a given $\rho$. For this reason, the jump term $J$ is introduced which penalises the discontinuities at the cell boundaries. It is given as:

$$J_{\substack{Neu\\Per\\Dir}} = \begin{pmatrix} \underset{L+R}{\overset{R}{L+R}} & -RL & 0 & & \underset{0}{\overset{0}{-LR}} \\ -LR & L+R & RL & & \\ 0 & -LR & \ddots & \ddots & \\ & & \ddots & & -RL \\ \underset{0}{\overset{0}{-RL}} & & & -LR & \underset{L+R}{\overset{L}{L+R}} \end{pmatrix} \tag{3.37}$$

The notation used to distinguish Neumann, periodic and Dirichlet boundaries in Eq. (3.22) is also used here. The result of the jump term is convergence when solving for $\phi$ but at the cost increased numerical diffusion that increases as $\alpha$ increases. What value of $\alpha$ should be taken is undefined, however, it seems to be beneficial for it to be of order 1 [75]. It should be noted that as the resolution of the domain increases with reduced discontinuities to follow, the effect of the jump term diminishes. This concludes the differential operators.

It should lastly be noted that the order of the discretisation is prescribed by the number of polynomial coefficients in the polynomial expansion. For a zeroth-order polynomial, $p = 0$, there is one coefficient and so, the discretisation is first order. Likewise, if $p = 1$, it is a second-order discretisation. So, in general, the order of the discretisation is $p + 1$.

### 3.2.3 Time integration

No numerical library for solving partial differential equations with a temporal component is complete without a time integration scheme. Such schemes can in general be split into two types, explicit and implicit time integration[79]. The two approaches can also be combined such that part of the equations are solved explicitly and the rest solved implicitly. This is sometimes referred to as IMEX, or semi-implicit, schemes. As a quick summary, suppose the state of the system $y(t)$ at time $t$ is known and the aim is to find the state at some later time $t + \delta t$ as prescribed by a system of equations $f(y,t)$. The simplest approaches describing these systems are the first order Euler method which, for the explicit, implicit and IMEX scheme, can be written as:

$$y_{n+1} = y_n + \delta t f(y_n, t_n) \tag{3.38}$$

$$y_{n+1} = y_n + \delta t f(y_{n+1}, t_{n+1}) \tag{3.39}$$

$$y_{n+1} = y_n + \delta t \left(g(y_n, t_n) + h(y_{n+1}, t_{n+1})\right) \tag{3.40}$$

Where $g(y,t)$ and $h(y,t)$ are the two component functions in the IMEX scheme which add up as $f(y,t) = g(y,t) + h(y,t)$. As can be seen, integration by the explicit Euler is very easy to perform as $y_n$ is known, whereas the implicit Euler requires solving a (coupled) system of algebraic equations to obtain $y_{n+1}$. In general, explicit schemes are very easy to incorporate and each time step is cheap to apply as it requires only a single function evaluation for each step. Implicit schemes, on the other hand, can be far more computationally demanding than explicit and IMEX schemes. This is due to the need for solving a large system of possibly non-linear algebraic equations. If an algebraic solution is unobtainable an iterative solver can be used instead. The choice of which iterative solver to use highly depends on the type of system you wish to solve. In general, implicit schemes can be far more computationally demanding but often allows for larger times steps. Especially if iterative schemes are used to solve the system, multiple function evaluations are needed before an acceptable solution is obtained. A rule of thumb for PDE's is to use explicit schemes for advective problems and implicit schemes for diffusive problems. The reason for this is that for diffusive problems the maximum stable time step in explicit schemes goes as:

$$\delta t_{max} \propto D\Delta\delta x^2, \tag{3.41}$$

where $\delta x$ is the grid spacing, while implicit schemes do not suffer this shortcoming. Here $D$ is some diffusion coefficient. This quickly becomes prohibitive if the discretised spatial domain is very large with small grid spacing. If the problem is purely advective, explicit schemes are limited by the CFL condition[79]:

$$\frac{u\delta t}{\Delta x} \leq C_{max} \tag{3.42}$$

where $C_{max}$ is the maximum Courant number that is usually around 1 for explicit whereas this does not apply for implicit schemes. However, as the time step only goes linearly with the grid spacing it is often advantageous to use explicit schemes for advective problems as the time step is much cheaper to perform. If the problem contains both advective and diffusive parts, an explicit approach might be applicable if the advection stability constraint is dominant, i.e. small diffusion coefficient. Otherwise one has to resort to an implicit method or an IMEX method. In the latter case, it is common to have the explicit part contain any advective components while the implicit part gets the diffusive components. If the diffusive part is linear, it can be solved using either a direct or as in the case of FELTOR, an iterative linear solver such as conjugate gradient.

When the MIHESEL equations were first implemented into the FELTOR framework, only explicit schemes and IMEX schemes for a linear implicit part were present. An explicit Runge Kutta method was used initially, however, it quickly became evident that even with HPC resources only a limited number of initial value problems were solvable.

The issue with the MIHESEL equations (Eqs. (2.143) to (2.146)) is that they are clearly non-linear and more importantly, they are non-linear in the diffusive part and the diffusive part is the dominating limitation for the time integration. To overcome this problem, a fully implicit scheme was implemented in such a way that it required no changes to the existing code being used in the explicit scheme. The resulting time integration scheme chosen was the backward differentiation formula (BDF) method which is a class of linear multistep methods. The method relies on approximating the time derivative using a finite difference approach which by using previous time steps can increase the order of the method. The general expression for

| | $\alpha_0$ | $\alpha_1$ | $\alpha_2$ | $\alpha_3$ | $\alpha_4$ | $\alpha_5$ | $\beta$ |
|---|---|---|---|---|---|---|---|
| $s=1$ | 1 | - | - | - | - | - | 1 |
| $s=2$ | $\frac{4}{3}$ | $-\frac{1}{3}$ | - | - | - | - | $\frac{2}{3}$ |
| $s=3$ | $\frac{18}{11}$ | $-\frac{9}{11}$ | $\frac{2}{11}$ | - | - | - | $\frac{6}{11}$ |
| $s=4$ | $\frac{48}{25}$ | $-\frac{36}{25}$ | $\frac{16}{25}$ | $-\frac{3}{25}$ | - | - | $\frac{12}{25}$ |
| $s=5$ | $\frac{300}{137}$ | $-\frac{300}{137}$ | $\frac{200}{137}$ | $-\frac{75}{137}$ | $\frac{12}{137}$ | - | $\frac{60}{137}$ |
| $s=6$ | $\frac{360}{147}$ | $-\frac{450}{147}$ | $\frac{400}{147}$ | $-\frac{225}{147}$ | $\frac{72}{147}$ | $-\frac{10}{147}$ | $\frac{60}{147}$ |

Table 3.1: Coefficient for the BDF formula to perform implicit time integration[80].

scheme is [80]:

$$y_{n+1} = \sum_{k=0}^{s-1} \alpha_k y_{n-k} + \delta t \beta f\left(y_{n+1}, t_{n+1}\right) \tag{3.43}$$

where $s$ is the order of the method. The coefficients $\alpha_k$ and $\beta$ for orders $s = 1..6$ are given in Section 3.2.3 : The stability of the methods decrease as the order increases, hence usually only orders up to three are used. As this is a multistep method, a problem presents itself in regards to starting the algorithm. The problem is that for orders higher than one, the method needs more than one previous value. However, as this is an initial value problem, more than one initial values are not know. Hence a starting method is needed to kick-start the procedure. For this, a multistage implicit Runge-Kutta method of order $s$, that has since been implemented in the library, is used. It should be noted here that multi stage methods are in this case more expensive to use since for each non-linear iteration the matrix in Eq. (3.2) needs to be inverted. This is the reason for using the single stage, multi step BDF method over implicit Runge Kutta methods. To solve the non-linear system of equations arising from the time integration a non-linear solver was needed. This will be discussed in detail in Section 3.2.5 along with testing of the numerical implementation of the BDF method.

### 3.2.4 Linear Solvers

As mentioned in Section 3.1, the MIHESEL model, the ion pressure and vorticity equations (Eqs. (2.144), (2.145) and (3.2)) are coupled in the time derivative. This means, that to put the MIHESEL equations in a form suitable for the BDF method the equations have to be solved for $\partial_t\phi, \partial_t p_1, \partial_t p_2, \cdots$ before the time integration can be performed. This requires solving a linear system of equations. When the equations were first implemented, only the conjugate gradient method was implemented. To speed up the convergence of the linear solve, it is implemented as a nested method, where the linear problem is solved first on a coarse grid, and the projected to a finer grid. This is repeated until it reaches the finest grid. The idea is that the projected solution is a good initial guess on the finer grid. The consequence of this is a significant reduction in the number of iterations and more importantly, wall clock time. Typically three grids are sufficient for a good speedup. For preconditioning the system, a simple diagonal preconditioner using the inverse weights $V$ given in Eq. (3.33). Since the conjugate gradient method is designed for symmetric positive definite matrices, the coupling of the time derivatives in the potential and pressure need to be cast as such. This will be discussed in detail in Section 3.1.1.

### 3.2.5 Non-Linear Solvers

In Section 3.2.3, the implementation of time integration techniques and in particular the implicit BDF method was discussed. Here it was discussed that in order to solve the system of equations arising in the Eq. (3.43) a nonlinear solver was needed. To find a solution to the problem it is first noticed that the time integration is in fact cast in the form of a fixed point iteration (or Picard iteration, non-linear Richardson):

$$\boldsymbol{y}_{n+1}^{i+1} = \boldsymbol{K}(\boldsymbol{y}_{n+1}^{i}) \tag{3.44}$$

where $K(\boldsymbol{x}_{n+1})$ represents the right hand side of Eq. (3.43) and $i$ is the iterator. This forms a basis for constructing an efficient non-linear solver, but a fixed point solver itself would not work as that the convergence properties of the method are dependent on the time step [81]. This is similar to the problems encountered with the explicit method. A modification to the method can be performed where a damping factor is introduced. The process is then to use the residual given as:

$$\boldsymbol{r}_i = \boldsymbol{y}_{n+1}^{i} - \boldsymbol{K}(\boldsymbol{y}_{n+1}^{i}). \tag{3.45}$$

The residual is then added to the solution with some damping parameter $\omega$:

$$\boldsymbol{y}_{n+1}^{i+1} = \boldsymbol{y}_{n+1}^{i} - \omega \boldsymbol{r}_i \tag{3.46}$$

| $m_{Max}$ | $m_{res}$ | $maxiter$ | $AAstart$ | $\omega$ | $\beta$ | $\epsilon$ |
|---|---|---|---|---|---|---|
| 10 | 10 | 500 | 0 | 0.1 | 0.9 | $10^{-7}$ |

Table 3.2: Typical input parameters for the Anderson acceleration algorithm.

This is the nonlinear version of modified Richardson iteration where the damping parameter $\omega$ can either be fixed or chosen using a line search method [82]. In the case of $\omega = 1$, it reduces to the simple fixed-point iteration. The damping parameter can significantly improve the convergence of the solver but it still might be prohibitively slow. One solution which has been implemented is to accelerate the convergence of the iterations using Anderson acceleration [83]. The idea is to use a linear combination of several previous iterations and a new trial solution to construct a new solution. If the new solution falls within some tolerance the iteration is terminated, and if not it is used to obtain the next iterative solution. The algorithm is summarized in Algorithm 1 and is based on the algorithm presented in [84].

A number of input parameters are needed for the algorithm to run. The function $\boldsymbol{F}(\boldsymbol{y})$ is a function whose root needs to found. In regards to the BDF method, this should be Eq. (3.45) that is written as $\boldsymbol{F}_i(\boldsymbol{y}) = \boldsymbol{y}^i_{n+1} - \boldsymbol{K}(\boldsymbol{y}^i_{n+1}) = \boldsymbol{r}_i$ where the aim is for the residual to get a close to zero as possible. The method requires the input $m_{Max}$,$m_{res}$,$maxiter$ and $AAstart$ stating the maximum number of previous iterations that should be used to obtain a new trial solution, after how many iterations the procedure should be restarted, the total number of iterations performed before it is deemed not to be converging and lastly a delay in when the acceleration should begin. The values $\omega$ and $\beta$ are damping parameters. The first is related to the modified Richardson iteration Eq. (3.46), while the latter is a damping parameter that aims to allow for more aggressive acceleration based on a linear combination of the previous iterations. Lastly, $\epsilon$ is the tolerance in the error for terminating the procedure and $S_{norm}$ is the norm with which the residual is calculated. For the latter, the norm is calculated using the weights given by Eq. (3.33). Some typical values that have been found to give good results are given in Table 3.2.

The algorithm was originally implemented for the use of electronic structure computations but has within recent years become much more studied and implemented for the general solution of non-linear systems of equations [86]. In particular, it has been shown that it is closely related to quasi-newton methods [87] and in the case of linear problems that it is very similar to the GMRES method for linear problems [86]. The above algorithm is a slight modification as it contains a restart after every $m$ iteration using information

**Algorithm 1** Anderson Acceleration algorithm based on [84] and [85]

```
procedure AA($\boldsymbol{F}(\boldsymbol{y}), \boldsymbol{y}, m_{Max}, m_{res}, maxiter, \epsilon, \beta, \omega, S_{norm}, AAstart$)
    System Initialization
    Set mAA = 0
    for $i = 1, .., maxiter$ do
        if $i \bmod m_{res} = 0$ then
            $mAA = 0$
        $f_i = \boldsymbol{F}(\boldsymbol{y}_{i-1})$ //
        $g_i = \boldsymbol{y}_{i-1} - \omega \cdot f_i$
        if $|f_i|_{S_{norm}} < \epsilon$ then
            Return $\boldsymbol{y}_i$
        if $mMax = 0$ then
            $\boldsymbol{y}_i = g_i$
        else
            if $k > AAstart$ then
                $df_i = f_i - f_{i-1}$
                if $mAA < m_{Max}$ then
                    $\mathcal{G}_{mAA} = g_i - g_{i-1}$
                else
                    $\mathcal{G}_j = \mathcal{G}_{j+1}, \quad j < mMax$        ▷ Shift all entries by one.
                    $\mathcal{G}_{m_{Max}} = g_i - g_{i-1}$        ▷ Add $g_i - g_{i-1}$ to last entry.
                $mAA = mAA + 1$
            if $mAA = 0$ then
                $\boldsymbol{y}_i = g_i$
            else
                if $mAA = 1$ then
                    $R(1,1) = \sqrt{df_i}$        ▷ First entry in R in QR decomposition
                    $\boldsymbol{Q}(1) = \frac{df_i}{R(1,1)}$        ▷ First column in Q in QR decomposition
                else
                    if $mAA > mMax$ then
                        $mAA = mAA - 1$
                        $QRdelete(Q, R)$        ▷ Remove column from Q and update R accordingly
                    for $j = 1, ..., mAA - 1$ do
                        $R(j, mAA) = Q(j) \cdot df_i$        ▷ Update R in QR decomposition
                        $df_i = df_i R(j, mAA) Q(j)$
                    $R(mAA, mAA) = \sqrt{df_i, df_i}$
                    $Q(mAA) = \frac{df_i}{R(mAA,mAA)}$
                Solve$R \cdot \gamma = Q^T \cdot f_i$        ▷ Solve least squares problem by backward substitution.
                $\boldsymbol{y}_i = g_i - \mathcal{G} \cdot \gamma$        ▷ Update $\boldsymbol{y}_i$
                if $\beta > 0$ and $\beta \neq 1$ then
                    $\boldsymbol{y}_i = \boldsymbol{y}_i - (1 - \beta)(f_i - Q \cdot R \cdot \gamma)$
```

only from the most recent iteration [85]. The implementation of the restart procedure seems to significantly improve the convergence of the algorithm. It should be noted that while the implicit time integration allows for larger time steps, larger steps, in general, require more iterations to converge. The reason for this is that the bigger the time-step, the bigger the error in the initial guess is and hence the problem becomes more ill-conditioned. For the initial guess, a linear prediction is given by:

$$\boldsymbol{y}_{n+1} = \sum_{i=0}^{N-1} \beta_i \boldsymbol{y}_{n-i} \tag{3.47}$$

where $N$ is the order of the method. Note that these coefficients are only applicable if the time step is fixed. Usually $N = 2$ seems to be a good choice, in which case $\beta_{1,2} = 2, -1$. The coefficients are given by Pascal's triangle. To test the implementation of the nonlinear solver, it is used to solve an initial value problem with an implicit time stepper. The idea is to construct a problem and manufacture a solution (method of manufactured solutions, or MMS), such that the problem can be solved for a known solution, which allows measuring the numerical error. For this procedure the BDF method discussed in Section 3.2.3 with the Anderson accelerator as the inner solver is applied to the problem, allowing for testing the time integrator and nonlinear solver at the same time. The validity of the time integration is to see whether the reduction in error reduces with the order of the method. The test of the Anderson acceleration is in the fact that it converges to the correct solution. The MMS is:

$$\frac{\partial}{\partial t} T(t,x,y) = \eta \nabla^2 T(t,x,y) + \cos(t) T(t,x,y) + S \tag{3.48}$$

With a manufactured solution:

$$T(t,x,y) = \sin(t)\exp(-2\eta t)\sin(x)\sin(y) \tag{3.49}$$

Which gives a source:

$$S = \cos(t)\exp(-2\eta t)\sin(x)\sin(y)(1 - sin(t)) \tag{3.50}$$

The test is such that the simulation is run until a fixed time, and the number of steps taken to get there is varied meaning the time step size is varied. As the number of time steps used to integrate over a fixed interval increases, the error is expected to decrease as $err \propto n_{ts}^{-N}$ where $N$ is the order of the method and $n_{ts}$ is the number of time steps used for the fixed interval. The convergence results are shown in Fig. 3.1. Here the error of the solution relative to the exact solution is shown as a function of the number of time steps used to resolve the same time interval. It is seen that for each spatial order there is a minimal error in the time integration that can be obtained. E.g., for first-order spatial resolution, the first-order temporal method obtains the desired reduction in error as a function of the number of time steps whereas higher-order temporal methods do not see the desired reduction in error. They do however obtain a smaller error than the first order. As the spatial order is increased it is seen that the correct order of reduction is obtained concluding in the sixth order spatial discretisation that all temporal orders achieve the correct error reduction scaling. An exception is the second and third-order spatial discretisation where the temporal error reduction order is not obtained. The cause seems to be that despite the order in space, the error in the spatial discretisation is still so large that it is dominating. In general, it should be noted that there is a 'competition' between the spatial discretisation error and the temporal. This means, e.g., that it is possible to see the full effect of a $6^{th}$ order BDF method when using a third-order spatial method but one needs to use either very large time steps, which gives a large temporal error or a very fine grid which gives a small spatial error. If none of these is the case the error introduced by the spatial discretisation will dominate.

## 3.3 Possible Future implementations

In the previous two sections, the Feltor library and the implementation of the MIHESEL model into it were discussed. When running the MIHESEL code, the experience is often that the bottleneck in the performance is the linear inversion of Eq. (3.2). Especially when turbulent dynamics are evolving, the number of iterations on each grid become large. Some possible considerations to alleviate this could be to use a pure multigrid method instead as the convergence of the method scales linearly with the size of the system. Furthermore, the preconditioning used for the system in the form of the inverse weights is rather crude. Hence, it might be beneficial to examine better preconditioners such as e.g. multigrid preconditioned conjugate gradient. Both methods have recently become available in the library, but have not been implemented in the solution of the MIHESEL equations.

In regards to the nonlinear solver, the Anderson acceleration has proven to be a decent nonlinear solver that is easy to implement. However, it does sometimes stagnate causing a breakdown in the simulation or require a large number of iterations. In many other libraries, it is common to use a variation of Newton's method [88]. The exact formulation of this method requires the inverse Jacobian. This is often quite impractical as the calculation of

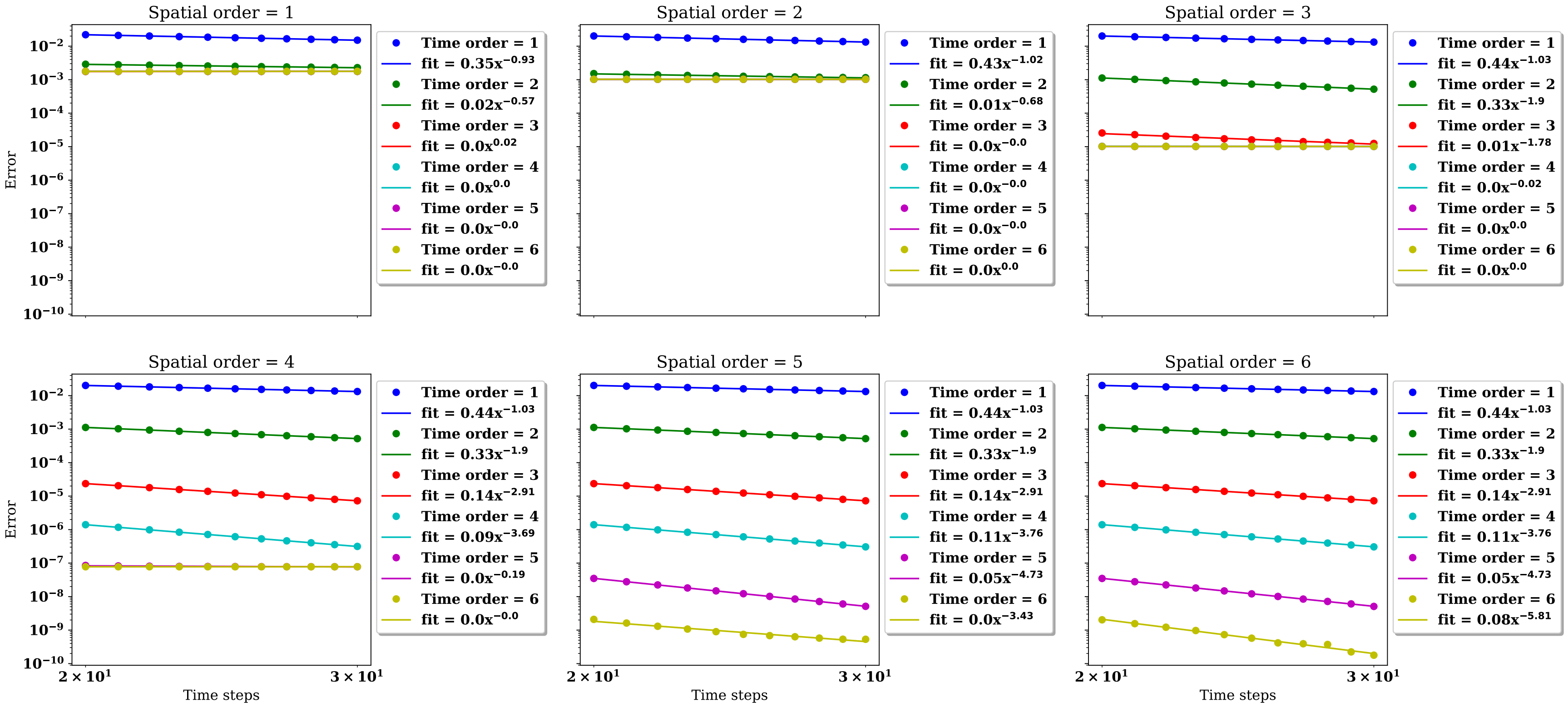

Figure 3.1: Error in time integration for spatial and temporal orders one to six

the inverse Jacobian matrix can be very expensive and memory intensive. Another approach is to approximately solve the system for the inverse Jacobi in an iterative fashion using a matrix-free Krylov inversion scheme. This method is known as a Newton-Krylov method and should in many cases have better convergence properties [89][81]. Since this only requires matrix-vector products and basic linear algebra operations the FELTOR library is well suited for this kind of problem. Additionally, the linear problems involved with approximating the inverse Jacobian, can be asymmetric and not necessarily positive definite. Hence a linear solver that works for these problems is needed. A version of GMRES [90] and BICGSTAB [91], both of which work for nonsymmetric and indefinite problems, have recently been implemented as part of this project, making the future implementation of the Newton method easier.

# Chapter 4

# Results

In the previous two sections, a multiple ion-species drift fluid model was derived. It is an extension of the HESEL model developed in house and used to study turbulence transport in the edge/SOL at the outboard midplane. Furthermore, the numerical implementation of the model in the FELTOR library, with the addition of fully implicit time integrators with non-linear solvers was discussed in the previous chapter on the numerical methods. In this section, the model will be employed to investigate physics related to transport at the outboard midplane. This section contains two overarching themes, seeded 2D blobs and 2D turbulent transport, with the goal of investigating the influence of isotope mixtures on transport in the edge/SOL. The first part on seeded 2D blobs contains the first paper on the MIHESEL model, that introduces the model and examines the effects of a deuterium-tritium mixture on the radial propagation of the blob. Additionally, the effect of ion charge on the blob propagation is examined by simulating a deuterium helium mix, where the latter is double charged. The second part is focused on turbulence in general. This is done by simulating edge profiles with certain mixtures of deuterium and tritium using realistic density and temperature profiles resembling what can be found in medium-sized tokamaks such as EAST, ASDEX-Upgrade, K-STAR or TCV.

## 4.1 Seeded 2D Filaments - Blobs

In this section seeded filaments - or blobs - are studied. Seeded blob filaments are a well-studied topic in regards to understanding the transport through blobs. Studies have been performed using a variety of modelling approaches such as drift fluid, gyro fluid, particle in cell and hybrid models, see e.g. [21], [52], [92]–[95]. They provide a simple look at the interchange dynamics of edge transport in a simplified setting. As such, they allow for a qualitative understanding of the turbulence driving mechanisms, while also providing some quantitative understanding of how the dynamics of the filaments are affected by the filament width, amplitude, ion temperature etc. [92].

## 4.1.1 Deuterium tritium Blobs

### 4.1.1.1 Prelude

The first paper produced regarding this work introduces the MIHESEL model and goes through many of the steps given in Chapter 2 used to derive the model. At the time of writing, the paper has been submitted to Physics of Plasmas and is in review of the first revision. In the seeded blobs, only the dynamics perpendicular to the magnetic field are accounted for in the paper. As such it is a pure 2D simulation. This means that the parallel parametrisations and sources terms are not part of the paper. With the model derived, the paper presents to first numerical results produced with the model by investigating the influence of a deuterium-tritium isotope mix on the radial propagation of seeded blobs. The initial mixture is divided into the background mix and the perturbation mix. A parameters scan over different compositions with varying background and perturbation mixes allows for a scaling of the maximum radial velocity of the centre of mass of the blob. The initialisation of the blobs is such that the electric potential is zero.

While this is somewhat idealised, it still gives insight into transport properties. The idealised nature comes is as it does not take into account how the blob was materialised in the first place. It turns out that the initialisation of the potential can have a significant impact on the propagation of the blob. A study of the effect of the initial potential can be found in [23].

# Collisional Multispecies Drift Fluid Model

A. Poulsen,[1, a)] J. Juul Rasmussen, M. Wiesenberger, and V. Naulin
*Department of Physics, Technical University of Denmark, DK-2800 Kgs. Lyngby. Denmark*

(Dated: January 29, 2020)

Transport in the edge and scrape-off layer mediated by turbulent fluctuations is often studied using drift fluid models. In this work, we expand previous work on a two-fluid single ion species drift model to a multi-ion-species model that incorporates collisional interactions between the individual species while conserving energy. The model is simplified into a set of equations that are computationally realisable. This is used to study the dependency of seeded blob propagation on different mixes of deuterium and tritium isotopes in the background and blob respectively. We find that the background mix is initially the dominant driver that determines propagation, but that the blob mix becomes the dominating factor for the continued evolution. It is found that the maximum velocity of the blob scales stronger with the initial blob mix than the background mix.

## I. INTRODUCTION

A fusion plasma is inherently composed of multiple ion species due to the fusion of two particles into a third of a different type. In future fusion reactor plasmas the reaction will be based on deuterium and tritium that fuses into in helium. How species of all kinds interact and how these interactions carry over to transport coefficients, particularly in regards to impurity transport, has been studied theoretically[1–4]. The importance of multi-component plasmas has become evident from experimental results that show how transport, and consequently confinement, is changed when the ion mix changes[5,6]. Numerically, this has been studied using gyro-kinetic codes by comparing simulations with different single species main ions[7] and in some cases also with heavy impurities[8]. Drift wave turbulence modeling[9] has also been employed, but again this was only with a single main ion species. True multi-component mixtures have been numerically studied focusing on impurities and their influence on turbulent behaviour using a drift fluid approach[10] but only with lower-order drifts in the direction perpendicular to the magnetic field. Other approaches used single ion species models to simulate mixes by using an effective mass and charge[11–13]. This limits the studies to plasmas with a uniform ratio of ion densities as well as equal temperatures. These assumptions are not valid when considering, e.g., fuelling with a single species, or when ion cyclotron resonance heating (ICRH) is used to heat the plasma. Here the resonance frequency predominantly leads to heating of particles with the same mass-charge ratio, such as deuterium and doubly charged helium 4. None of these approaches include the dynamics arising from the collisional interactions between all species.

In toroidally confined plasmas much of the turbulent transport occurs where the edge of the core with closed magnetic field lines, meets the scrape-off layer (SOL) with open magnetic field lines, at the last closed flux surface (LCFS). In this paper, we present a drift fluid turbulence model for the perpendicular dynamics in a 2D slab geometry of the SOL/EDGE at the outboard midplane[14]. The model seeks to accurately include the interactions between all plasma species through collisions resulting in resistive drifts for each species. The model uses the Zhdanov closure[2] for plasma mixes with multiple ion species of arbitrary mass and charge. The model is to be considered an extension of the HESEL[14,15] model and allows for solving for the evolution of the individual densities and pressures of an arbitrary number of species. In this regard, we note that the HESEL model is based on the Braginskii closure[16], which uses the Chapman-Enskog approximation with two Laguerre-Sonine polynomials, whereas the Zhdanov closure uses Grad's 21 moment method. It should be emphasized that for a single ion species the Zhdanov and Braginskii closures approaches yield identical results for the transport coefficients. The Zhdanov closure naturally assumes a multi-component plasma making it useful for our model. Similar results can be obtained using the Chapman-Enskog approach as done in refs. 4 and 1 at the cost of a heavy mathematical formalism. For the pressure equations, the closure limits us to studying near equal temperatures in the ion species.

The remainder of this paper is organised as follows: In Section II we outline the theoretical steps towards a multispecies model with collisional effects and derive the associated energy theorem. This is simplified into a computationally efficient model named MIHESEL in Section III. The model is tested by simulating a range of DT mixes in seeded blobs in Section IV. Finally, in Section V we summarize and discuss our findings.

## II. MULTISPECIES DRIFT FLUID MODEL WITH COLLISIONAL EFFECTS

The starting point for the derivation of the multispecies drift fluid model is the general momentum equation for an arbitrary plasma species[1], denoted with subscripts $s$:

$$m_s n_s \frac{d}{dt}\boldsymbol{u}_s = n_s q_s\left(\boldsymbol{E}+\boldsymbol{u}_s\times\boldsymbol{B}\right)+\boldsymbol{R}_s-\nabla p_s-\nabla\cdot\overleftrightarrow{\boldsymbol{\pi}}_s, \quad (1)$$

where $m_s$, $q_s$, $n_s$, $\boldsymbol{u}_s$ are the mass, charge, density and fluid velocity of species $s$, $d/dt=\partial_t+\boldsymbol{u}_s\cdot\nabla$ is the total derivative, $\boldsymbol{E}$, $\boldsymbol{B}$ are the electric and magnetic field respectively, $p_s$ is the scalar pressure and $\overleftrightarrow{\boldsymbol{\pi}}_s$ the viscous stress tensor. The quantity

---

[a)] Electronic mail: aslakp@fysik.dtu.dk

$\boldsymbol{R}_s$ is the total resistive force acting on the species due to collisions with other species. In general we can split this resistive force into a frictional $\boldsymbol{R}_{s,u}$ part and a thermal $\boldsymbol{R}_{s,T}$ part. The perpendicular frictional part for a species $s'$ acting on species $s$ is given by[2]

$$\boldsymbol{R}_{s'\to s,u,\perp} = -n_s m_s \nu_{s'\to s}\left(\boldsymbol{u}_{\perp,s} - \boldsymbol{u}_{\perp,s'}\right), \tag{2}$$

while the thermal force is given by:

$$\boldsymbol{R}_{s'\to s,T,\perp} = \frac{3}{2} m_s n_s \nu_{s'\to s} \mu_{s's}\left(\frac{\boldsymbol{b}\times\nabla T_s}{m_s q_s B} - \frac{\boldsymbol{b}\times\nabla T_{s'}}{m_{s'} q_{s'} B}\right), \tag{3}$$

where $T_s$ is the species temperature and $\nu_{s'\to s}$ is the collision frequency between two species defined below and $\mu_{ss'} = m_s m_{s'}/(m_s + m_{s'})$. Furthermore, we have introduced the magnetic unit vector $\boldsymbol{b} = \boldsymbol{B}/B$ where the magnetic field in a Cartesian coordinate system is assumed to be of the form:

$$\boldsymbol{B}(x) = \frac{B_0 R}{R + r + x}\hat{\boldsymbol{z}}, \tag{4}$$

where $B_0$ is the magnetic field at the major radius $R$, $r$ is the minor radius and $\hat{\boldsymbol{z}}$ is the unit vector pointing in the z-direction parallel to the magnetic field. We assume the magnetic field to be straight and that. Assuming a tokamak with a large aspect ratio and small q-factor this can be viewed as an approximation of the magnetic field at the outboard midplane. Furthermore, due to the large aspect ratio, this does not take into account the magnetic field shear. Summing over all species $s'$ gives the total resistive force acting on species $s$. In the case of electron-ion interactions, we will consider the large mass ratio and make appropriate approximations. In the current case, this means neglecting the ion gradient term in Eq. 3 when dealing with ion-electron resistive forces. In the derivation of the total resistive force[2] it is assumed that $T_\alpha - T_\beta \ll T_\alpha$ for ion-ion interactions. Throughout the paper, we use the species indices $s$ and $s'$ for ions and electrons alike, while $\alpha$ and $\beta$ will be used for ions only and likewise $e$ for electrons. This is to distinguish terms where there are different approximations for ions and electron due to, e.g., the mass ratio.

The stress tensor $\overleftrightarrow{\pi}$ is comprised of a parallel component, a perpendicular collisional component and a gyro viscous component. Since we only consider a 2D slab geometry, we leave out the parallel component of the stress tensor. With $\boldsymbol{b}$ along the z-axis in an $(x,y,z)$ coordinate system, the perpendicular collisional part of the ion stress tensor is given by:

$$\overleftrightarrow{\pi}_{\perp,\alpha} = -\eta_{\perp,\alpha}\begin{bmatrix} (\partial_x u_x - \partial_y u_y) & (\partial_x u_y + \partial_y u_x) \\ (\partial_x u_y + \partial_y u_x) & (-\partial_x u_x + \partial_y u_y) \end{bmatrix}, \tag{5}$$

where the coefficient is given by summing over all ion species:

$$\eta_{\perp,\alpha} = \sum_\beta \eta_{\perp,\beta\to\alpha} = \frac{1}{4}\frac{p_\alpha}{\Omega_{c,\alpha}^2}\sum_\beta \frac{m_\alpha m_\beta}{\left(m_\alpha + m_\beta\right)^2} \cdot \nu_{\beta\to\alpha}\left(\frac{6}{5}\frac{m_\beta}{m_\alpha} + 2 - \frac{4}{5}\frac{m_\beta}{m_\alpha}\frac{Z_\alpha}{Z_\beta}\right), \tag{6}$$

with the ion gyro-frequency

$$\Omega_{c,\alpha} = \frac{Z_\alpha e B}{m_\alpha}, \tag{7}$$

where $Z_\alpha$ is the charge number. We have here only considered the ion viscous stress tensor due to the mass dependency. The electron stress tensor is therefore neglected.

The non-collisional gyro-viscous part of the tensor is given by:

$$\overleftrightarrow{\pi}_{gy,\alpha} = \eta_{\alpha,gy}\begin{bmatrix} -(\partial_x u_y + \partial_y u_x) & (\partial_x u_x - \partial_y u_y) \\ (\partial_x u_x - \partial_y u_y) & (\partial_x u_y + \partial_y u_x) \end{bmatrix}, \tag{8}$$

with the coefficient given by:

$$\eta_{\alpha,gy} = \frac{p_\alpha}{2\Omega_{c,\alpha}}. \tag{9}$$

Again the electron stress tensor is small compared to the ion stress tensor due to the small mass and so it is neglected.
For the collisional parts of the resistive force and stress tensor the collision frequency is defined as[2]:

$$\nu_{s'\to s} = \frac{2^{1/2} n_{s'} Z_s^2 Z_{s'}^2 e^4 \ln\Lambda_{ss'}\left(1 + \frac{m_s}{m_{s'}}\right)}{12\pi^{3/2}\varepsilon_0^2 m_s^2\left(\frac{T_s}{m_s} + \frac{T_{s'}}{m_{s'}}\right)^{3/2}}. \tag{10}$$

The Coulomb logarithm is defined such that:

$$\Lambda_{ss'} = \frac{12\pi\varepsilon_0}{|Z_s Z_{s'} e^2|}\frac{\mu_{ss'}}{\gamma_{ss'}}\lambda_d, \tag{11}$$

with $\gamma_{ss'} = \gamma_s\gamma_{s'}/(\gamma_s + \gamma_{s'})$ where $\gamma_s = m_s/T_s$. Finally, the Debye length is given as:

$$\lambda_d = \left(\sum_s \frac{n_s Z_s^2 e^2}{\varepsilon_0 T_s}\right)^{-\frac{1}{2}}. \tag{12}$$

Numerically solving the momentum equation requires resolving all time and lengths scales including electron gyro-motion scales. Turbulent transport occurs on time and length scales much larger than these scales. Hence, we use a reduced fluid model that resolves the proper scales and captures the physics of interest while being numerically accessible. With all elements defined, we follow Ref.14 and proceed to the drift ordering. Here, we employ the usual assumptions of the characteristic time scales being longer than the reference ion (such as deuterium) gyro period and perpendicular lengths scales being longer than the ion gyro radius:

$$\frac{\omega}{\Omega_{c,Ref}} \ll 1 \quad \text{and} \quad \frac{\rho_\alpha^2}{L_\perp^2} \ll 1, \tag{13}$$

where

$$\rho_\alpha = \sqrt{\frac{T_\alpha}{m_\alpha \Omega_{c,\alpha}^2}}. \tag{14}$$

The lowest order drifts following this are the electric and diamagnetic drift, which are given by:

$$\boldsymbol{u}_{s,0} = \boldsymbol{u}_E + \boldsymbol{u}_{D,s} = \frac{\boldsymbol{b}\times\nabla\phi}{B} + \frac{\boldsymbol{b}\times\nabla p_s}{q_s n_s B}. \tag{15}$$

The plasma at the outboard midplane is weakly collisional, meaning the resistive force can be assumed to be next order (denoted order 1). Following Ref. 16, the same goes for the viscous stress tensor. Consequently, for the next order drift we find the polarisation, resistive and viscous drift:

$$\begin{aligned}\boldsymbol{u}_{s,1} &= \boldsymbol{u}_{p,s} + \boldsymbol{u}_{R,s} + \boldsymbol{u}_{\pi,s} \\ &= \Omega_{c,s}^{-1}\boldsymbol{b} \times \frac{d}{dt}\boldsymbol{u}_{s,0} - \frac{\boldsymbol{b}\times\boldsymbol{R}_s}{q_s n_s B} + \frac{\boldsymbol{b}\times\nabla\cdot\overleftrightarrow{\pi}_s}{q_s n_s B}. \end{aligned} \tag{16}$$

The resistive and viscous drifts depend on the velocity $\boldsymbol{u}_s$, but the respective drifts are first order meaning we use only zeroth order drifts $\boldsymbol{u}_{s,0}$ when evaluating them.

We now turn our attention to the equations for density, vorticity and pressure. Inserting the expression for the fluid velocities into the continuity equation[1], yields the perpendicular density equation for ions:

$$\frac{\partial}{\partial t}n_\alpha + \nabla\cdot\left(n_\alpha\left[\boldsymbol{u}_E + \boldsymbol{u}_{D,\alpha} + \boldsymbol{u}_{p,\alpha} + \boldsymbol{u}_{R,\alpha} + \boldsymbol{u}_{\pi,\alpha}\right]\right) = 0. \tag{17}$$

We impose quasi-neutrality $\sum_\alpha Z_\alpha n_\alpha = n_e$, meaning there is no need to solve an electron density equation explicitly. As a result, multiplying the density equation for all species by their charge state $Z_s$ (with $Z_e = -1$) and summation under the quasi neutrality condition yields the vorticity equation:

$$\begin{aligned}\sum_s Z_s\left(\frac{\partial}{\partial t}n_s + \nabla\cdot(n_s\boldsymbol{u}_s)\right) &= \\ \sum_\alpha Z_\alpha\nabla\cdot\left(n_\alpha\left[\boldsymbol{u}_{D,\alpha} + \boldsymbol{u}_{p,\alpha} + \boldsymbol{u}_{\pi,\alpha}\right]\right) - \nabla\cdot\left(n_e\left[\boldsymbol{u}_{D,e}\right]\right) &= 0\end{aligned} \tag{18}$$

Here, we have used that the viscosity and polarisation terms are mass dependent and so are negligible for electrons. Also we employed that the resistive force conserves momentum, $\boldsymbol{R}_{s'\to s} = -\boldsymbol{R}_{s\to s'}$ and consequently that all $\nabla\cdot Z_s n_s \boldsymbol{u}_{R,s}$ terms cancel.

Finally, the pressure equations are found from the multi-species pressure moment equation[1]. For electrons this gives:

$$\begin{aligned}&\frac{3}{2}\frac{\partial}{\partial t}p_e + \frac{3}{2}\nabla\cdot\left(p_e\left[\boldsymbol{u}_E + \boldsymbol{u}_{D,e} + \boldsymbol{u}_{R,e}\right]\right) \\ &+ p_e\nabla\cdot\left(\boldsymbol{u}_E + \boldsymbol{u}_{D,e} + \boldsymbol{u}_{R,e}\right) + \nabla\cdot\boldsymbol{q}_e = \tilde{Q}_e,\end{aligned} \tag{19}$$

and for each ion species $\alpha$:

$$\begin{aligned}&\frac{3}{2}\frac{\partial}{\partial t}p_\alpha + \frac{3}{2}\nabla\cdot\left(p_\alpha\left[\boldsymbol{u}_E + \boldsymbol{u}_{D,\alpha} + \boldsymbol{u}_{p,\alpha} + \boldsymbol{u}_{R,\alpha} + \boldsymbol{u}_{\pi,\alpha}\right]\right) \\ &\quad + p_\alpha\nabla\cdot\left(\boldsymbol{u}_E + \boldsymbol{u}_{D,\alpha} + \boldsymbol{u}_{p,\alpha} + \boldsymbol{u}_{R,\alpha} + \boldsymbol{u}_{\pi,\alpha}\right) \\ &\quad + \overleftrightarrow{\pi}_\alpha : \nabla\boldsymbol{u}_{0,\alpha} + \nabla\cdot\boldsymbol{q}_\alpha = \tilde{Q}_\alpha.\end{aligned} \tag{20}$$

Here, the total collisional energy exchange is $\tilde{Q}_s = \sum_{s'}\tilde{Q}_{s'\to s}$. The interspecies collisional energy exchange is given as $\tilde{Q}_{s'\to s} = Q_{s'\to s} - \boldsymbol{u}_s\cdot\boldsymbol{R}_{s'\to s}$ with $Q_{s'\to s} = -Q_{s\to s'}$, which is required for energy conservation. As the resistive force is order 1 due to low collisionality, it is evaluated using the lowest order drifts, which gives $-\boldsymbol{u}_s\cdot\boldsymbol{R}_{s'\to s} \simeq -\boldsymbol{u}_{s,0}\cdot\boldsymbol{R}_{s'\to s} = -\boldsymbol{u}_{R,s'\to s}\cdot(q_s n_s\nabla\phi + \nabla p_s)$. Finally, the thermal energy exchange is given by[2]:

$$Q_{s'\to s} = \frac{3 n_s m_s \nu_{s'\to s}\left(T_{s'} - T_s\right)}{m_s + m_{s'}}. \tag{21}$$

By using the expression for the collision frequency in equation (10) it is easily verified that this satisfies the required energy conservation condition $Q_{s'\to s} = -Q_{s\to s'}$. For the ion pressure equation (20) the collisional energy exchange and the resistive drifts can be combined to read:

$$\begin{aligned}&\frac{3}{2}\nabla\cdot\left(p_\alpha\boldsymbol{u}_{R,\alpha}\right) + p_\alpha\nabla\cdot\boldsymbol{u}_{R,\alpha} - \tilde{Q}_\alpha \\ &= \frac{5}{2}\nabla\cdot\left(p_\alpha\boldsymbol{u}_{R,\alpha}\right) - \sum_s Q_{s\to\alpha} + \boldsymbol{u}_{R,\alpha}\cdot\left(q_\alpha n_\alpha\nabla\phi\right).\end{aligned} \tag{22}$$

We now turn our attention to the heat flux $\boldsymbol{q}_s$. In general it can be split into a parallel $\boldsymbol{q}_{\|,s}$, perpendicular collisional $\boldsymbol{q}_{\perp,s}$ and diamagnetic heat flux $\boldsymbol{q}_{\times,s}$. For ions, omitting the parallel component, these are given by[2]

$$\boldsymbol{q}_{\times,\alpha} = \frac{5}{2}\frac{p_\alpha}{q_\alpha B}\boldsymbol{b}\times\nabla T_\alpha, \tag{23}$$

$$\begin{aligned}\boldsymbol{q}_{\perp,\alpha} = \frac{p_\alpha}{m_\alpha^2\Omega_{c,\alpha}^2}\sum_\beta \mu_{\alpha\beta}\nu_{\beta\to\alpha}&\left(\frac{3}{2}\left[\frac{\nabla p_\alpha}{n_\alpha} - \frac{Z_\alpha\nabla p_\beta}{Z_\beta n_\beta}\right]\right. \\ - \frac{m_\alpha}{m_\alpha + m_\beta}&\left.\left[\left(\frac{13}{4}\frac{m_\beta}{m_\alpha} + 4 + \frac{15}{2}\frac{m_\alpha}{m_\beta}\right)\nabla T_\alpha - \frac{27}{4}\frac{Z_\alpha}{Z_\beta}\nabla T_\beta\right]\right).\end{aligned} \tag{24}$$

Although the expression is lengthy, it should be noted that in the case of a single ion species, it reduces to the expression found in Braginskii[16].

For electrons similar expressions are given in Ref. 2. When using the mass disparity between ions and electrons this can be written in a compact form[4]:

$$\boldsymbol{q}_{\times,e} = -\frac{5}{2}\frac{p_e}{eB}\boldsymbol{b}\times\nabla T_e \tag{25}$$

$$\begin{aligned}\boldsymbol{q}_{\perp,e} = \frac{p_e}{m_e\Omega_{c,e}^2}\sum_\alpha \nu_{\alpha\to e}&\left(\frac{3}{2}\left[\frac{\nabla p_e}{n_e} + \frac{\nabla p_\alpha}{Z_\alpha n_\alpha}\right]\right. \\ &\left. - \left[\left(\frac{13}{4} + \frac{\sqrt{2}}{Z_\alpha}\right)\nabla T_e\right]\right).\end{aligned} \tag{26}$$

From the resistive force Eq. 2 and 3 in the large mass ratio limit and using the lowest order drifts, the electron resistive drift becomes:

$$\begin{aligned}\boldsymbol{u}_{R,u,e} &= -\sum\frac{\nu_{\alpha\to e}}{m_e\Omega_{c,e}^2}\left(\frac{\nabla p_e}{n_e} + \frac{\nabla p_\alpha}{Z_\alpha n_\alpha}\right) \quad \text{and} \\ \boldsymbol{u}_{R,T,e} &= \frac{3}{2}\sum\frac{\nu_{\alpha\to e}}{m_e\Omega_{c,e}^2}\nabla T_e.\end{aligned} \tag{27}$$

With this it is instructive to write the perpendicular collisional heat flux as:

$$\boldsymbol{q}_{\perp,e} = \boldsymbol{q}_{\perp,u,e} + \boldsymbol{q}_{\perp,T,e} =$$

$$-\frac{3}{2}p_e\boldsymbol{u}_{R,u,e}-\sum_\alpha p_e\left(\frac{13}{4}+\frac{\sqrt{2}}{Z_\alpha}\right)\frac{2}{3}\boldsymbol{u}_{R,T,\alpha\rightarrow e}. \tag{28}$$

Combining Eq. (28) with the collisional energy exchange and the resistive drift terms in the electron pressure equation we obtain:

$$\begin{aligned}\frac{3}{2}\nabla\cdot\left(p_e\boldsymbol{u}_{R,e}\right)+p_e\nabla\cdot\boldsymbol{u}_{R,e}+\nabla\cdot\boldsymbol{q}_{\perp,e}-\tilde{Q}_e=\\ \nabla\cdot\left(p_e\boldsymbol{u}_{R,e}\right)-\nabla\cdot\sum_\alpha p_e\left(1+\frac{\sqrt{2}}{Z_\alpha}\right)\frac{2}{3}\boldsymbol{u}_{R,T,e}\\ -Q_e+\boldsymbol{u}_{R,e}\cdot\left(q_e n_e\nabla\phi\right).\end{aligned} \tag{29}$$

Lastly, we simplify the polarisation term by employing the gyro-viscous cancellation in which part of the gyro viscous tensor component cancels out the diamagnetic contribution to the advection velocity in the polarisation term giving a simpler expression. Since the gyro-viscous part of the stress tensor is non-collisional it is independent of other species and as such the cancellation holds regardless of the number of ion species. A commonly used form of this cancellation is expressed as[17]:

$$\nabla\cdot\boldsymbol{\pi}_{gy,\perp,\alpha}+n_\alpha\left(\boldsymbol{u}_{D,\alpha}\cdot\nabla\right)\boldsymbol{u}_{\perp,\alpha,0}=\nabla_\perp\chi. \tag{30}$$

The term on the right hand side represents the remainder of the gyro-viscous cancellation. As this is commonly neglected, which we will also do, we will not consider it in detail. The polarisation term then reads:

$$\begin{aligned}&\nabla\cdot\left(n_\alpha\left[\boldsymbol{u}_{p,\alpha}+\boldsymbol{u}_{\pi,gy,\alpha}\right]\right) \qquad (31)\\ &=-\nabla\cdot\frac{n_\alpha}{\Omega_{c,\alpha}}\frac{d'}{dt}\left(\frac{\nabla_\perp\phi}{B}+\frac{\nabla_\perp p_\alpha}{q_\alpha n_\alpha B}\right)+\nabla\cdot n_\alpha\boldsymbol{u}_{\chi,\alpha},\end{aligned}$$

where the term $\boldsymbol{u}_{\chi,\alpha}$ is the drift associated with the remainder of the gyro-viscous cancellation stated in Eq. (30) and where the total derivative is given by:

$$\frac{d'}{dt}=\frac{\partial}{\partial t}+\left(\boldsymbol{u}_E+\boldsymbol{u}_{p,\alpha}+\boldsymbol{u}_{R,\alpha}+\boldsymbol{u}_{\pi,\alpha}\right)\cdot\nabla. \tag{32}$$

We note that due to the appearance of the polarisation drift in the advective part of the total derivative, the drift is recursively defined by itself, making it impractical for numerical implementations. As such it is commonly dropped. We do the same when deriving the numerically implementable model.

It should be noted that due to the drift fluid expansion, and subsequent truncation, the ion density, ion pressure and vorticity equations contain an asymmetry when adding the ion densities together. This means that multiple identical ion species with equal temperature, but with different densities, do not add exactly to give the same as if they were represented by one combined density distribution unless $n_\alpha/n_\beta=$ const. everywhere. Correct summing of the ion species is a fundamental requirement for multispecies modelling, and so should always be considered carefully. Taking e.g. the ion density equation this would imply that

$$\sum_\alpha\left(\frac{\partial}{\partial t}n_\alpha+\nabla\cdot n_\alpha\boldsymbol{u}_\alpha\right)=\frac{\partial}{\partial t}n_i+\nabla\cdot n_i\boldsymbol{u}_i \tag{33}$$

where $n_i=\sum_\alpha n_\alpha$. For our drift fluid version of the continuity equation this equality does not hold. The source of inequality occurs in the vorticity and ion pressure equations and are related to terms associated with polarisation and viscosity drifts. This is because the terms are non-linear in $n_\alpha$ as e.g

$$\begin{aligned}\sum_\alpha\nabla\cdot n_\alpha\boldsymbol{u}_{p,\alpha}&=\sum_\alpha\nabla\cdot n_\alpha\Omega_{c,\alpha}\boldsymbol{b}\times\frac{d}{dt}\left(\frac{\boldsymbol{b}\times\nabla\phi}{B}+\frac{\boldsymbol{b}\times\nabla p_\alpha}{q_\alpha n_\alpha B}\right)\\ &\neq\nabla\cdot\sum_\alpha n_\alpha\Omega_{c,\alpha}\boldsymbol{b}\times\frac{d}{dt}\left(\frac{\boldsymbol{b}\times\nabla\phi}{B}+\frac{\boldsymbol{b}\times\nabla\sum_\alpha p_\alpha}{q_\alpha\sum_\alpha n_\alpha B}\right),\end{aligned} \tag{34}$$

which in turn is due to the inclusion of the diamagnetic drift as a lowest order drift as seen in equation (15). The validity of the occurrence of the diamagnetic drift at this order is discussed in Ref. 18. As the polarization and viscosity drift are of higher order the effect is expected to be small and therefore negligible, which has been confirmed by numerical experiments (see last paragraph of IV).

### A. Energy conservation

In this section we derive the energy theorem for the collisional multispecies drift fluid model expressed in equation Eqs. (17) to (20). Similar to Refs. 14 and 19 we start by multiplying the vorticity equation (18) with $e\phi$ followed by integrating over all space while neglecting the surface terms. Combining all this together yields the global fluid kinetic energy:

$$\begin{aligned}\int \mathrm{d}V e\phi\sum_\alpha\nabla\cdot Z_\alpha n_\alpha\boldsymbol{u}_{p,\alpha}+e\phi\sum_\alpha\nabla\cdot Z_\alpha n_\alpha\boldsymbol{u}_{D,\alpha}\\ -e\phi\nabla\cdot n_e\boldsymbol{u}_{D,e}+e\phi\sum_\alpha\nabla\cdot Z_\alpha n_\alpha\boldsymbol{u}_{\pi,\alpha}\\ =\int\mathrm{d}V\boldsymbol{u}_E\cdot\sum_\alpha m_\alpha n_\alpha\frac{d}{dt}\left(\boldsymbol{u}_E+\boldsymbol{u}_{D,\alpha}\right)\\ +\boldsymbol{u}_E\cdot\left(\sum_\alpha\nabla p_\alpha+\nabla p_e\right)+\boldsymbol{u}_E\cdot\sum_\alpha\nabla\cdot\boldsymbol{\pi}=0.\end{aligned} \tag{35}$$

The next part of the energy theorem is the thermal energy given by the pressures. Integrating the electron pressure equation (19) over space and neglecting surface terms yet again, gives:

$$\int\mathrm{d}V\frac{3}{2}\frac{\partial}{\partial t}p_e-\boldsymbol{u}_E\cdot\nabla p_e+\boldsymbol{u}_{R,e}\cdot\left(q_e n_e\nabla\phi\right)-Q_e=0. \tag{36}$$

Finally, we perform the same procedure for the ion pressure equations Eq. (20):

$$\begin{aligned}\int\mathrm{d}V\frac{3}{2}\frac{\partial}{\partial t}p_\alpha+n_\alpha m_\alpha\boldsymbol{u}_{D,\alpha}\frac{d}{dt}\left(\boldsymbol{u}_E+\boldsymbol{u}_{D,\alpha}\right)\\ -\boldsymbol{u}_E\cdot\nabla p_\alpha+\left(\nabla\cdot\boldsymbol{\pi}_\alpha\right)\cdot\boldsymbol{u}_{D,\alpha}+\boldsymbol{u}_{R,\alpha}\cdot\left(q_\alpha n_\alpha\nabla\phi\right)\\ +\boldsymbol{\pi}_\alpha:\nabla\boldsymbol{u}_{\alpha,0}-Q_\alpha=0.\end{aligned} \tag{37}$$

With the above equations at hand we proceed to sum everything together. To this end we first look at the interaction terms between ion species, i.e. the resistive and heat exchange term. Starting with the resistive fluid drift for ions we have:

$$\boldsymbol{u}_{R,\alpha} = \boldsymbol{u}_{R,e\to\alpha} + \sum_{\beta} \boldsymbol{u}_{R,\beta\to\alpha}. \tag{38}$$

Evaluating the frictional force given in Eq. (2) with the lowest order drifts we have that the resistive drift is linear in $n_s$ and that $n_s u_{R,s'\to s}$ is antisymmetric in $s$ and $s'$. Consequently, all terms related to $\boldsymbol{u}_R$ cancel when summing all pressure equations. As for the heat exchange term (Eq. (21)), since $m_s n_s \nu_{s'\to s} = m_{s'} n_{s'} \nu_{s\to s'}$ it becomes evident that $Q_{s'\to s} = -Q_{s\to s'}$ and consequently that all ion-ion heat exchange terms cancel when summed and similar for ion-electron heat exchange. Integration by parts of the $\boldsymbol{\pi}_\alpha : \nabla \boldsymbol{u}_{\alpha,0}$ term allows for the diamagnetic part to cancel the fourth term in Eq. (37). The total ion thermal energy contribution to the energy theorem then becomes:

$$\begin{aligned}\int \mathrm{d}V \frac{3}{2}\frac{\partial}{\partial t}\sum_\alpha p_\alpha + \sum_\alpha m_\alpha n_\alpha \boldsymbol{u}_{D,\alpha}\cdot \frac{d}{dt}\left(\boldsymbol{u}_E + \boldsymbol{u}_{D,\alpha}\right)\\ -\sum_\alpha \boldsymbol{u}_E \cdot \nabla p_\alpha - \sum_\alpha \left(\nabla\cdot \boldsymbol{\pi}_\alpha\right)\cdot \boldsymbol{u}_E + \sum_\alpha \boldsymbol{u}_{R,e\to\alpha}\cdot\left(q_\alpha n_\alpha \nabla\phi\right)\\ -\sum_\alpha Q_{e\to\alpha} = 0.\end{aligned} \tag{39}$$

The final energy theorem is now obtained by adding the contributions from the vorticity (35), electron (36) and ion pressure (39), and invoking the density equation to put the density under the time derivative. In conclusion, the energy theorem reads:

$$\frac{\partial}{\partial t}\int \mathrm{d}V\left(\frac{3}{2}p_e + \sum_\alpha\left(\frac{3}{2}p_\alpha + \frac{1}{2}m_\alpha n_\alpha u_{\alpha,0}^2\right)\right) = 0. \tag{40}$$

This is the general energy theorem and so the total energy given as the sum of the thermal and kinetic energy as we expect.

## III. COMPUTATIONALLY IMPLEMENTABLE MODEL: MIHESEL-MODEL

The system of equations presented in Section II is numerically cumbersome to implement and so we seek to simplify the equations to get a numerically workable model. In this section we also discus the influence of the approximations on the energy theorem and the summability of the equations in regards to the asymmetry in summation discussed earlier. As mentioned, we consider a 2D slab geometry with $x$ and $y$ as the radial and poloidal directions respectively with the magnetic field given by equation (4). The process of simplifying the model starts with the terms involving the polarisation and gyro viscosity drifts. As mentioned in equation (30), the sum of these terms results in the gyro viscous cancellation. The remainder term $\boldsymbol{u}_{\chi,\alpha}$ from the cancellation is dropped in (32) and for computational convenience we employ the thin layer approximation[14]. The terms involving the polarisation drift, which only concerns ions, are thus reduced to:

$$\nabla\cdot\left(n_\alpha\left[\boldsymbol{u}_{p,\alpha} + \boldsymbol{u}_{\pi,gy,\alpha}\right]\right) \simeq -\frac{n_{\alpha,0}}{\Omega_{c,\alpha,0}}\nabla\cdot\left(d_t^0 \nabla_\perp \phi_\alpha^*\right), \tag{41}$$

$$\nabla\cdot\left(p_\alpha\left[\boldsymbol{u}_{p,\alpha} + \boldsymbol{u}_{\pi,gy,\alpha}\right]\right) \simeq -\nabla\cdot\frac{p_\alpha}{\Omega_{c,\alpha,0}}\left(d_t^0 \nabla_\perp \phi_\alpha^*\right), \tag{42}$$

$$p_\alpha \nabla\cdot\left(\boldsymbol{u}_{p,\alpha} + \boldsymbol{u}_{\pi,gy,\alpha}\right) \simeq -\frac{p_\alpha}{\Omega_{c,\alpha,0}}\nabla\cdot\left(d_t^0 \nabla_\perp \phi_\alpha^*\right), \tag{43}$$

with

$$\phi_\alpha^* = \frac{\phi}{B_0} + \frac{p_\alpha}{q_\alpha n_{\alpha,0} B_0} \quad \text{and} \quad d_t^0 = \partial_t + \boldsymbol{u}_{E,0}\cdot\nabla. \tag{44}$$

Here, $n_{s,0}$ is the characteristic reference value for density. The expression in Eq. (42) is formally small[14], and is consequently left out of the ion pressure equation. The exclusion of this term does not violate the energy theorem. The similarity of the approximations in Eq (41) and (43) is required for energy conservation.

Moving on to the collisional terms and starting with the frictional resistive component we evaluate them using the lowest order drifts $\boldsymbol{u}_E$ and $\boldsymbol{u}_{D,\alpha}$, in which case the electric drifts cancel, leaving only the diamagnetic contribution. The total resistive drift is then approximated as:

$$\begin{aligned}\boldsymbol{u}_{R,s} = -\sum_{s'}\frac{\nu_{s'\to s}}{m_s \Omega_{c,s}^2}\left(\frac{\nabla p_s}{n_s} - \frac{q_s}{q_{s'}}\frac{\nabla p_{s'}}{n_{s'}}\right)\\ +\frac{3}{2}\sum_{s'}\frac{\nu_{s'\to s}}{m_s \Omega_{c,s}^2}\mu_{ss'}\left(\frac{\nabla T_s}{m_s} - \frac{q_s}{q_{s'}}\frac{\nabla T_{s'}}{m_{s'}}\right).\end{aligned} \tag{45}$$

Similar to Ref. 14 we see that the thermal gradient terms partially cancel and so we neglect them giving the approximation:

$$\boldsymbol{u}_{R,s} \simeq -\sum_{s'}\frac{\nu_{s'\to s}v_{th,s}^2}{\Omega_{c,s}^2 T_s}\left(T_s\frac{\nabla n_s}{n_s} - \frac{q_s}{q_\alpha}T_{s'}\frac{\nabla n_{s'}}{n_{s'}}\right) \tag{46}$$

$$\simeq -\sum_{s'}\frac{D_{s'\to s,0}n_{s'}}{n_{s',0}T_{s,0}}\left(T_s\frac{\nabla n_s}{n_s} - \frac{q_s}{q_{s'}}T_{s'}\frac{\nabla n_{s'}}{n_{s'}}\right) = \boldsymbol{u}_{R,s,0}, \tag{47}$$

where we define the diffusion coefficient as:

$$D_{s'\to s,0} \equiv \rho_{0,s}^2 \nu_{s'\to s,0}. \tag{48}$$

For the density equation and pressure equation this results in:

$$\begin{aligned}\nabla\cdot n_s \boldsymbol{u}_{R,s} \simeq \nabla\cdot n_s \boldsymbol{u}_{R,s,0} = -\sum_{s'}\frac{D_{s'\to s,0}}{n_{s',0}T_{s,0}}\\ \Big(T_s \nabla n_{s'}\cdot\nabla n_s + n_{s'}\nabla T_s\cdot\nabla n_s + T_s n_{s'}\nabla^2 n_s\\ -\frac{Z_s}{Z_{s'}}\left[T_{s'}\nabla n_s\cdot\nabla n_{s'} + n_s \nabla T_{s'}\cdot\nabla n_{s'} + T_{s'}n_s\nabla^2 n_{s'}\right]\Big),\end{aligned} \tag{49}$$

$$\begin{aligned}\nabla\cdot p_s \boldsymbol{u}_{R,s} \simeq \nabla\cdot T_{0,s} n_s \boldsymbol{u}_{R,s,0} = -\sum_{s'}\frac{D_{s'\to s,0}}{n_{s',0}}\\ \Big(T_s \nabla n_{s'}\cdot\nabla n_s + n_{s'}\nabla T_s\cdot\nabla n_s + T_s n_{s'}\nabla^2 n_s\end{aligned}$$

$$- \frac{Z_s}{Z_{s'}} \left[ T_{s'} \nabla n_s \cdot \nabla n_{s'} + n_s \nabla T_{s'} \cdot \nabla n_{s'} + T_{s'} n_s \nabla^2 n_{s'} \right] \Bigg), \quad (50)$$

$$\boldsymbol{u}_{R,s} \cdot (q_s n_s \nabla \phi) \simeq \boldsymbol{u}_{R,s,0} \cdot (q_s n_s \nabla \phi)$$

$$= - \sum_{s'} \frac{D_{s' \to s,0}}{n_{s',0} T_{s,0}} \left( T_s n_{s'} \nabla n_s - \frac{q_s}{q_{s'}} T_{s'} n_s \nabla n_{s'} \right) \cdot (q_s \nabla \phi). \quad (51)$$

These approximations do not change the energy conservation as the two first terms appear as surface terms in the integral and as such are intergrated out. Eq. 51 is symmetric in indices and all terms cancel when summing over all species. For the electron pressure equation the resistive contributions from Eq. (29) are approximated as:

$$\nabla \cdot (p_e \boldsymbol{u}_{R,e}) - \nabla \cdot \sum_\alpha p_e \left( 1 + \frac{\sqrt{2}}{Z_\alpha} \right) \frac{2}{3} \boldsymbol{u}_{R,T,e}$$

$$\simeq \nabla \cdot (p_e \boldsymbol{u}_{R,e,0}) - \sum_\alpha D_{\alpha \to e,0} \left( 1 + \frac{\sqrt{2}}{Z_\alpha} \right) \nabla \cdot (n_e \nabla T_e). \quad (52)$$

The ion heat conduction is approximated as:

$$\nabla \cdot q_{\perp,\alpha} \simeq \sum_\beta \frac{D_{\beta \to \alpha,0}}{m_\alpha n_{0,\beta}} \mu_{\alpha\beta} \nabla \cdot \Bigg( \frac{3}{2} \left[ n_\beta \nabla p_\alpha - \frac{Z_\alpha}{Z_\beta} n_\alpha \nabla p_\beta \right]$$

$$- \frac{m_\alpha}{m_\alpha + m_\beta} n_\alpha n_\beta \left[ \left( \frac{13}{4} \frac{m_\beta}{m_\alpha} + 4 + \frac{15}{2} \frac{m_\alpha}{m_\beta} \right) \nabla T_\alpha - \frac{Z_\alpha}{Z_\beta} \frac{27}{4} \nabla T_\beta \right] \Bigg). \quad (53)$$

Again, this does not alter the energy theorem.

Finally, we consider terms related to the ion viscous stress tensor. When calculating the stress tensor, we evaluate the velocities using the lowest order drifts and use the same approximation used in the polarisation drift. Furthermore, the viscosity coefficients $\eta_{\perp,\alpha}$ are computed using reference values for the pressure and magnetic field. The tensor finally reads:

$$\overleftrightarrow{\pi}_{\perp,\alpha} \simeq - \eta_{\perp,\alpha} \begin{bmatrix} -2\partial_{xy} \phi_\alpha^* & (\partial_{xx} - \partial_{yy}) \phi_\alpha^* \\ (\partial_{xx} - \partial_{yy}) \phi_\alpha^* & 2\partial_{xy} \phi_\alpha^* \end{bmatrix}. \quad (54)$$

In the approximations of terms including the viscosity drift we evaluate $\eta_{\perp,\alpha}$ and $n_\alpha$ in the denominator at reference values as done in, e.g., Eqs. (57) to (60). For the dyadic product of the stress tensor and the zeroth order drifts entering the ion pressure equation, the perpendicular collisional part is then approximated using reference values for pressure, collision frequency and magnetic field in the viscosity coefficient. Likewise the lowest order drift is given approximated as $\boldsymbol{u}_{\perp,\alpha,0} = \boldsymbol{b} \times \nabla \phi_\alpha^*$. In the end this gives:

$$\boldsymbol{\pi}_{\perp,\alpha,0} : \nabla \boldsymbol{u}_{\perp,\alpha,0}$$

$$\simeq - \sum_\beta m_\alpha n_{\alpha,0} D_{\pi,\beta \to \alpha,0} \left[ \left( \partial_x^2 \phi_\alpha^* - \partial_y^2 \phi_\alpha^* \right)^2 + 4 \left( \partial_{xy} \phi_\alpha^* \right)^2 \right], \quad (55)$$

$$\boldsymbol{\pi}_{gy,\alpha,0} : \nabla \boldsymbol{u}_{\perp,\alpha,0} = 0, \quad (56)$$

where the stress tensor diffusion coefficient is defined as:

$$D_{\pi,\beta \to \alpha,0} \equiv \frac{\eta_{\perp,\beta \to \alpha,0}}{n_{\alpha,0} m_{\alpha,0}}$$

$$= D_{\beta \to \alpha,0} \frac{m_\alpha m_\beta}{\left( m_\alpha + m_\beta \right)^2} \left( \frac{3}{10} \frac{m_\beta}{m_\alpha} + \frac{1}{2} - \frac{1}{5} \frac{m_\beta}{m_\alpha} \frac{Z_\alpha}{Z_\beta} \right). \quad (57)$$

The remaining terms involving the stress tensor are approximated as:

$$\nabla \cdot n_\alpha \boldsymbol{u}_{\pi,\perp,\alpha} \simeq \sum_\beta \frac{n_{\alpha,0} D_{\pi,\beta \to \alpha,0}}{\Omega_{c,\alpha,0}} \nabla^2 \nabla^2 \phi_\alpha^*, \quad (58)$$

$$\nabla \cdot p_\alpha \boldsymbol{u}_{\pi,\perp,\alpha} \simeq \sum_\beta \frac{p_{\alpha,0} D_{\pi,\beta \to \alpha,0}}{\Omega_{c,\alpha,0}} \nabla^2 \nabla^2 \phi_\alpha^*, \quad (59)$$

$$p_\alpha \nabla \cdot \boldsymbol{u}_{\pi,\perp,\alpha} \simeq p_\alpha \sum_\beta \frac{D_{\pi,\beta \to \alpha,0}}{\Omega_{c,\alpha,0}} \nabla^2 \nabla^2 \phi_\alpha^*. \quad (60)$$

The term given in Eq. (59) is left out as $\nabla \cdot (p_\alpha \boldsymbol{u}_{\pi,\alpha}) / \nabla \cdot \boldsymbol{q}_\alpha \sim \rho_\alpha^2 / L_\perp^2 \ll 1$. The two other terms in Eqs. (58) and (60) are approximated so that together with Eq. (56) energy is conserved.

Having done all the approximations above we employ neoclassical corrections to the equations by multiplying the diffusion coefficients by a correction factor[14]:

$$D_{s' \to s} \to \left( 1 + \frac{R}{r} q_{95}^2 \right) D_{s' \to s}, \quad (61)$$

where $R$ is the major radius, $r$ is the minor radius and $q_{95}$ is the safety factor. In principle, the neoclassical correction should only be applied to the averaged fields on closed field lines as it assumes longer timescales than what is found in intermittent turbulent transport. However, to simplify the implementation of open and closed field lines the correction is kept for the whole domain.

For numerical convenience we perform gyro-Bohm normalisation giving the dynamic variables:

$$\frac{T_s}{T_{e,0}} \to T_{\alpha,e}, \ \frac{x}{\rho_D} \to x, \ \Omega_{c,D,0} t \to t, \ \frac{e\phi}{T_{e,0}} \to \phi, \ \frac{n_s}{n_{e,0}} \to n_{\alpha,e}, \quad (62)$$

and the static values:

$$\frac{m_s}{m_D} \to \mu_s, \ \frac{n_{s,0}}{n_{e,0}} \to a_s, \ \frac{T_{s,0}}{T_{e,0}} \to \tau_s. \quad (63)$$

Here $\Omega_{c,D,0} = eB_0/m_D$, $\rho_D = \sqrt{T_{e,0}/m_D \Omega_{c,D,0}^2}$, with the subscript $D$ indicating deuterium. In general it can be any normalisation but for this work we will use Deuterium as the normalising species. We can now write down the final MIHESEL-model equations:

$$\frac{d}{dt} n_\alpha + n_\alpha \mathscr{C}(\phi) + \frac{1}{Z_\alpha} \mathscr{C}(p_\alpha)$$

$$- a_\alpha \frac{\mu_\alpha}{Z_\alpha} \nabla \cdot \left( \frac{d^0}{dt} \nabla_\perp \phi_\alpha^* \right) = \Lambda_{n_\alpha}, \quad (64)$$

$$\sum_\alpha a_\alpha \mu_\alpha \nabla \cdot \left( \frac{d^0}{dt} \nabla_\perp \phi_\alpha^* \right) - \mathscr{C} \left( \sum_\alpha p_\alpha + p_e \right) = \Lambda_w, \quad (65)$$

$$\frac{3}{2}\frac{d}{dt}p_\alpha+\frac{5}{2}p_\alpha\mathscr{C}(\phi)+\frac{5}{2}\frac{1}{Z_\alpha}\mathscr{C}\left(\frac{p_\alpha^2}{n_\alpha}\right)$$
$$-p_\alpha\frac{\mu_\alpha}{Z_\alpha}\nabla\cdot\left(\frac{d^0}{dt}\nabla_\perp\phi_\alpha^*\right)=\Lambda_{p_\alpha}, \qquad (66)$$

$$\frac{3}{2}\frac{d}{dt}p_e+\frac{5}{2}p_e\mathscr{C}(\phi)-\frac{5}{2}\mathscr{C}\left(\frac{p_e^2}{n_e}\right)=\Lambda_{p_e}. \qquad (67)$$

Here $\phi_\alpha^*=\phi+p_\alpha/q_\alpha a_\alpha$ is the generalised potential. The right hand side contains all terms related to collisions and viscosity and are given by:

$$\begin{aligned}\Lambda_{n_\alpha}=&\sum_s\frac{D_{s\to\alpha,0}}{a_s\tau_\alpha}\Bigg(T_\alpha\nabla n_s\cdot\nabla n_\alpha+n_s\nabla T_\alpha\cdot\nabla n_\alpha+T_\alpha n_s\nabla^2 n_\alpha\\&-\frac{Z_\alpha}{Z_s}\left[T_s\nabla n_\alpha\cdot\nabla n_s+n_\alpha\nabla T_s\cdot\nabla n_s+T_s n_\alpha\nabla^2 n_s\right]\Bigg)-\sum_\beta\frac{a_\alpha D_{\pi,\beta\to\alpha,0}}{\Omega_{c,\alpha,0}}\nabla^2\nabla^2\phi_\alpha^*, \end{aligned}\qquad (68)$$

$$\Lambda_w=\sum_\alpha\sum_\beta Z_\alpha\frac{a_\alpha D_{\pi,\beta\to\alpha,0}}{\Omega_{c,0,\alpha}}\nabla^2\nabla^2\phi_\alpha^*, \qquad (69)$$

$$\begin{aligned}\Lambda_{p_\alpha}=&\frac{5}{2}\sum_s\frac{D_{s\to\alpha,0}}{a_s}\Bigg(T_\alpha\nabla n_s\cdot\nabla n_\alpha+n_s\nabla T_\alpha\cdot\nabla n_\alpha+T_\alpha n_s\nabla^2 n_\alpha\\&-\frac{Z_\alpha}{Z_s}\left[T_s\nabla n_\alpha\cdot\nabla n_s+n_\alpha\nabla T_s\cdot\nabla n_s+T_s n_\alpha\nabla^2 n_s\right]\Bigg)-p_\alpha\sum_\beta\frac{D_{\pi,\beta\to\alpha,0}}{\Omega_{c,\alpha,0}}\nabla^2\nabla^2\phi_\alpha^*\\&-\sum_\beta\frac{D_{\beta\to\alpha,0}}{\mu_\alpha a_\beta}\mu_{\alpha\beta}\nabla\cdot\Bigg(\frac{3}{2}\left[n_\beta\nabla p_\alpha-\frac{Z_\alpha}{Z_\beta}n_\alpha\nabla p_\beta\right]\\&-\frac{\mu_\alpha}{\mu_\alpha+\mu_\beta}n_\alpha n_\beta\left[\left(\frac{13}{4}\frac{\mu_\beta}{\mu_\alpha}+4+\frac{15}{2}\frac{\mu_\alpha}{\mu_\beta}\right)\nabla T_\alpha-\frac{Z_\alpha}{Z_\beta}\frac{27}{4}\nabla T_\beta\right]\Bigg)\\&+\sum_s\frac{D_{s\to\alpha,0}}{a_s\tau_\alpha}\left(T_\alpha n_s\nabla n_\alpha-\frac{q_\alpha}{q_s}T_s n_\alpha\nabla n_s\right)\cdot(q_\alpha\nabla\phi)\\&+\sum_\beta\mu_\alpha a_\alpha D_{\pi,\beta\to\alpha,0}\left[\left(\partial_x^2\phi_\alpha^*-\partial_y^2\phi_\alpha^*\right)^2+4\left(\partial_{xy}\phi_\alpha^*\right)^2\right]+\sum_s\frac{3n_\alpha n_s\nu_{s\to\alpha,0}\mu_\alpha\left(T_s-T_\alpha\right)}{a_s(\mu_\alpha+\mu_s)}, \end{aligned}\qquad (70)$$

$$\begin{aligned}\Lambda_{p_e}=&\sum_s\frac{D_{s\to e,0}}{a_s}\Bigg(T_e\nabla n_s\cdot\nabla n_e+n_s\nabla T_e\cdot\nabla n_e+T_e n_s\nabla^2 n_e\\&-\frac{Z_e}{Z_s}\left[T_s\nabla n_e\cdot\nabla n_s+n_e\nabla T_s\cdot\nabla n_s+T_s n_e\nabla^2 n_s\right]\Bigg)+\sum_\alpha\left(1+\frac{\sqrt{2}}{Z_\alpha}\right)D_{\alpha\to e,0}\nabla\cdot(n_e\nabla T_e)\\&+\sum_s\frac{D_{s\to e,0}}{a_s\tau_e}\left(T_e n_s\nabla n_e-\frac{q_e}{q_s}T_s n_e\nabla n_s\right)\cdot(q_e\nabla\phi)+\sum_s\frac{3n_e n_s\nu_{s\to e,0}\mu_e\left(T_s-T_e\right)}{a_s(\mu_e+\mu_s)}. \end{aligned}\qquad (71)$$

The advective derivatives are defined as:

$$\frac{d}{dt}=\frac{\partial}{\partial t}+\frac{1}{B}\{\phi,\cdot\}\quad\text{and}\quad\frac{d^0}{dt}=\frac{\partial}{\partial t}+\{\phi,\cdot\}, \qquad (72)$$

where $\{f,g\}=\partial_x f\partial_y g-\partial_y f\partial_x g$ is the Poisson bracket. The curvature operator is given as:

$$\mathscr{C}(f)\equiv\nabla\cdot\left(\frac{\boldsymbol{b}\times\nabla_\perp f}{B}\right)=-\frac{\rho_D}{R}\partial_y f. \qquad (73)$$

Lastly, we revisit the energy conservation. We have already discussed how none of the approximations lead to a violation of the energy conservation and redoing the calculation of the energy theorem with these approximations yields:

$$\frac{\partial}{\partial t}\int \mathrm{d}V\left(\frac{3}{2}p_e+\left(\sum_\alpha\frac{3}{2}p_\alpha+a_\alpha\mu_\alpha\frac{|\nabla\phi_\alpha^*|^2}{2}\right)\right)=0 \qquad (74)$$

As mentioned, models such as the HESEL model[14] that use only one ion species have been extensively used to study the evolution of the dynamics in the edge/SOL. The MIHESEL model naturally reduces to a single ion species model. In this case the sum over species $s$ involves only one ion species and the electrons, while the sums over $\alpha$ and $\beta$ reduce to a single ion species term each. In the latter case, one has $\alpha=\beta$, meaning that, e.g., $\mu_\alpha=\mu_\beta$.

## IV. SIMULATIONS OF SEEDED BLOB DYNAMICS

As a first test and demonstration of the model we solve the above equations with seeded blobs as the initial condition where we introduce a Gaussian perturbation in the density:

$$n_\alpha(x,y,t=0) = n_{\alpha,bg} + n_{\alpha,b}\exp\left(-\frac{(x-x_c)^2}{2\sigma_{x,\alpha}^2} - \frac{(y-y_c)^2}{2\sigma_{y,\alpha}^2}\right). \tag{75}$$

Here $n_{\alpha,bg}$ is the background density and $n_b$ is the blob amplitude. For the width of the blob we use $\sigma_{x,\alpha} = \sigma_{y,\alpha} = 10\rho_D$ for all species. For reference values we have $n_{e,0} = 1.5 \cdot 10^{19} m^{-3}$, $T_{e,0} = T_{\alpha,0} = 20eV$ and $B_0 = 2T$. In the poloidal (y) direction we employ periodic boundaries while we use Dirichlet and Neumann boundaries for the inner and outer radial (x) boundaries respectively. The equations are numerically solved using the FELTOR discontinuous Galerkin library[20]. Here we have $N_x = 2N_y = 192$ grid cells and use three polynomial coefficients for a third order method. The box size is $L_x = 2L_y = 200\rho_D$. The time integration is done using a third order implicit backward differentiation formula (BDF) method with a time step of $dt = 0.5$. The resulting non-linear system of equations is solved using Anderson acceleration[21], where for each Anderson iteration we solve the system of equation for the partial derivative. This means we need to perform an inner inversion of the potential and ion pressure equations since these are intricately coupled in the time derivative. To do so we cast them in the form:

$$\begin{pmatrix} -\sum_\alpha a_\alpha \mu_\alpha \nabla^2 & -\frac{\mu_1}{Z_1}\nabla^2 & -\frac{\mu_2}{Z_2}\nabla^2 & \cdots \\ -\frac{\mu_1}{Z_1}\nabla^2 & \frac{3}{2}\frac{1}{p_1} - \frac{\mu_1}{Z_1^2 a_1}\nabla^2 & 0 & \\ -\frac{\mu_2}{Z_2}\nabla^2 & 0 & \frac{3}{2}\frac{1}{p_2} - \frac{\mu_2}{Z_2^2 a_2}\nabla^2 & \\ \vdots & & & \ddots \end{pmatrix} \cdot \begin{pmatrix} \partial_t \phi \\ \partial_t p_1 \\ \partial_t p_2 \\ \vdots \end{pmatrix} =$$

$$\begin{pmatrix} -\left(\Lambda_w + \mathscr{C}\left(\sum_\alpha p_\alpha + p_e\right) - \sum_\alpha a_\alpha \mu_\alpha \nabla\cdot\{\phi, \nabla_\perp \phi_\alpha^*\}\right) \\ \left(\Lambda_{p_1} - \frac{5}{2}p_1 \mathscr{C}(\phi) - \frac{5}{2}\frac{1}{Z_1}\mathscr{C}\left(\frac{p_1^2}{n_1}\right) + p_1 \frac{\mu_1}{Z_1}\nabla\cdot\{\phi, \nabla_\perp \phi_1^*\}\right)/p_1 \\ \left(\Lambda_{p_2} - \frac{5}{2}p_2 \mathscr{C}(\phi) - \frac{5}{2}\frac{1}{Z_2}\mathscr{C}\left(\frac{p_2^2}{n_2}\right) + p_2 \frac{\mu_2}{Z_2}\nabla\cdot\{\phi, \nabla_\perp \phi_2^*\}\right)/p_2 \\ \vdots \end{pmatrix} \tag{76}$$

Because of the complex form of the matrix we invert this system with a matrix-free approach. We consider a two ion-species plasma of deuterium and tritium, which is split into different configurations for the background and perturbation mix. The collection of configurations are all possible combinations of 'Background mix' and 'Perturbation mix' given in table I. The sum of ion densities is such that in normalised units, $n_{tot,bg} = \sum_\alpha n_{\alpha,bg} = 1$ and $n_{tot,b} = \sum_\alpha n_{\alpha,b} = 1$ for all runs.

An example of the evolution of the electron density profile is shown in Fig. 1 for the case of 50%D and 50%T in both background and perturbation with the center of mass position superimposed on top. Here we see the characteristic 'pluming' behaviour of seeded blobs moving radially outward. Additionally, there is an asymmetrical evolution of the blob in the poloidal direction. This asymmetry is a consequence of finite ion temperature effects. Both the radial and poloidal motions are very similar to what is seen in e.g. Ref. 22 and 23 for single ion species simulations. The electron density is shown, as it is the sum of the ion densities and as such, serves as an indicator of the overall plasma evolution.

In Fig. 2 left, we show the radial center of mass position for the blob as a function of time. In Fig. 2 right, we show the radial center of mass normalized to the case of 50%-50% DT in both background and blob. The center of mass is defined as:

$$\boldsymbol{X}_c \equiv \frac{1}{M}\int \boldsymbol{x} \sum_\alpha m_\alpha \left(n_\alpha - n_{\alpha,bg}\right) \mathrm{d}V, \tag{77}$$

where M is the mass of the blob given as

$$M = \int \sum_\alpha m_\alpha \left(n_\alpha - n_{\alpha,bg}\right) \mathrm{d}V. \tag{78}$$

The electron mass is neglected since it is much smaller. From the left figure, we observe that the blobs overall follow much the same trend with the light mixes moving faster. This picture eventually becomes less clear as light blobs in heavy backgrounds appear to have moved further at the end of the simulation. From the right figure, we see that the initial development is grouped within the seven distinct background mixes (see Table I) but quickly separates according to the perturbation mix. At around $t\Omega_{ciD} \sim 1800$ this picture is switched as we observe a grouping corresponding to the perturbation mix after which they will start to separate again. Overall it is evident that initial mixes with more deuterium (green) in general move faster radially than with tritium (purple) while the dependency on the perturbation mix increases over time.

| | D | T | D | T | D | T | D | T | D | T | D | T | D | T |
|---|---|---|---|---|---|---|---|---|---|---|---|---|---|---|
| Background mix | 12,5 | 87,5 | 25 | 75 | 37,5 | 62,5 | 50 | 50 | 62,5 | 37,5 | 75 | 25 | 87,5 | 12,5 |
| Pertubation mix | 12,5 | 87,5 | 25 | 75 | 37,5 | 62,5 | 50 | 50 | 62.5 | 37.5 | 75 | 25 | 87,5 | 12,5 |

Table I: Table of setups for mixes in background and perturbation with 49 unique initial conditions in total.

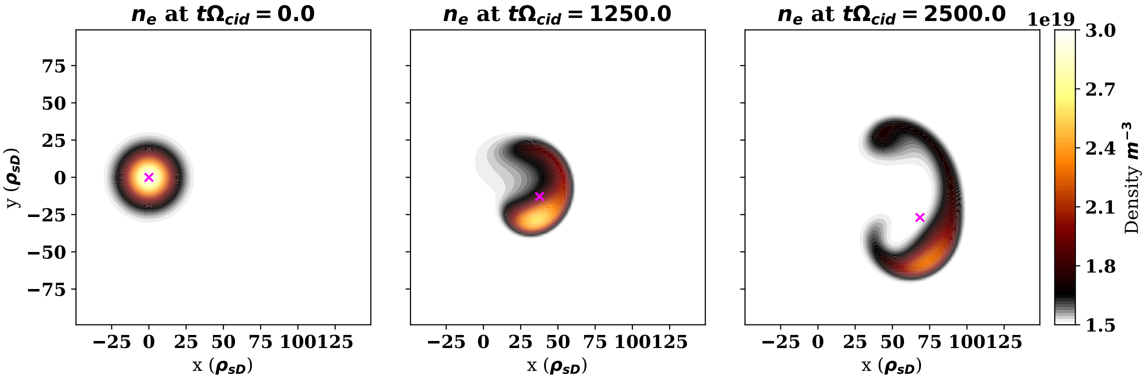

Figure 1: Electron density for the case of 50% D, 50% T in both background and perturbation taken at different snapshots with the center of mass superimposed as magenta crosses.

Taking the time derivative of the center of mass position yields the radial velocity of the center of mass. This is related to the flux given by[24]:

$$\Gamma(t) = \int \sum_{\alpha} m_\alpha n_\alpha \boldsymbol{u}_\alpha \mathrm{d}V = M\boldsymbol{V}_C = M\frac{d}{dt}\boldsymbol{X}_C. \tag{79}$$

Consequently, it is interesting to look at the (maximum) velocity as it indicates the (maximum) flux. The radial velocity is shown in fig. 3. Here it is observed that mixes with more deuterium especially in the blob have higher initial radial velocity and reach their maximum earlier than for tritium dominated simulations. However, over time, this picture will reverse with tritium dominated blobs having higher velocity in the end. Taking a closer look at the maximum velocity in fig. 3 right, it becomes clear that the moment at which the maximum value is obtained is highly dependent on the background density illustrated by the seven groupings. Comparing each group we see that overall the maximum velocity decreases as the amount of tritium in the background increases. Within each group, it is clear that the amount of tritium in the perturbation significantly affects the maximum velocity.

To quantitatively estimate the influence of the mixture we perform a simple scaling analysis. From previous scaling studies of the maximum blob velocity we know that it scales as $v_{max} \propto m^{-0.5}$ (see e.g. Ref. 13) and so we expect something similar in our case. However, since the mix in the background can differ from the blob mix we use a composite scaling of the form $v_{max} \propto m^a_{eff,bg} m^b_{eff,b}$ where we have introduced an ion effective mass given by:

$$m_{eff} = \frac{\sum_\alpha n_\alpha m_\alpha}{\sum_\alpha n_\alpha}. \tag{80}$$

With this the dependency of the effective mass of the initial blob and background on the maximum radial velocities is found to scale as:

$$\begin{aligned} &V_{max}(m_{eff,b}, m_{eff,bg}) \\ &\quad = 0.055(\pm 0.001)\left(m_{eff,b}^{-0.34(\pm 0.01)} + m_{eff,bg}^{-0.25(\pm 0.01)}\right). \end{aligned} \tag{81}$$

From this velocity scaling we observe that the maximum radial velocity scales strongest with the perturbation mix, but also that the background mix plays a significant role. It should be noted that in the case of uniform initial ratio the background and the perturbation effective masses are the same. With this we get a scaling of $V_{max}(m_{eff}) \propto m_{eff}^{-0.589}$. This differs slightly from the theoretical $m_{eff}^{-0.5}$ scaling, however, the magnitude of blob put us in an energy-limited regime, as discussed in Ref. 25, giving the slightly higher mass dependency. Naturally, this scaling only works with the initial conditions presented earlier. The dependency of the effective mass in the blob is expected to also scale with, e.g., the magnitude of the blob.

Lastly, we consider how the mix in the blob evolves. Within the model equations, we have included interactions between all species through collisions, which are contained within the resistive drift terms as seen in Eq. (45). Here it is observed that the resistive force will result in an equilibration of the mix such that $n_\alpha \to c_\alpha n_\beta$ where $c_\alpha$ is some constant. We examine this by looking at the ratio of tritium in the blob over time normalized to the background ratio with the result being shown in Fig. 4. In this figure, there is a clear tendency for all mixes to converge to the background mix as a consequence of the resistive force. As a result, it is to be expected that in a plasma where this is a dominating force, the plasma will tend towards a homogeneously mixed plasma that can be described by an effective mass approach. Up to now, we have only considered the center of mass propagation. We now discuss the differences in the density distribution for the 50%D 50%T case. In

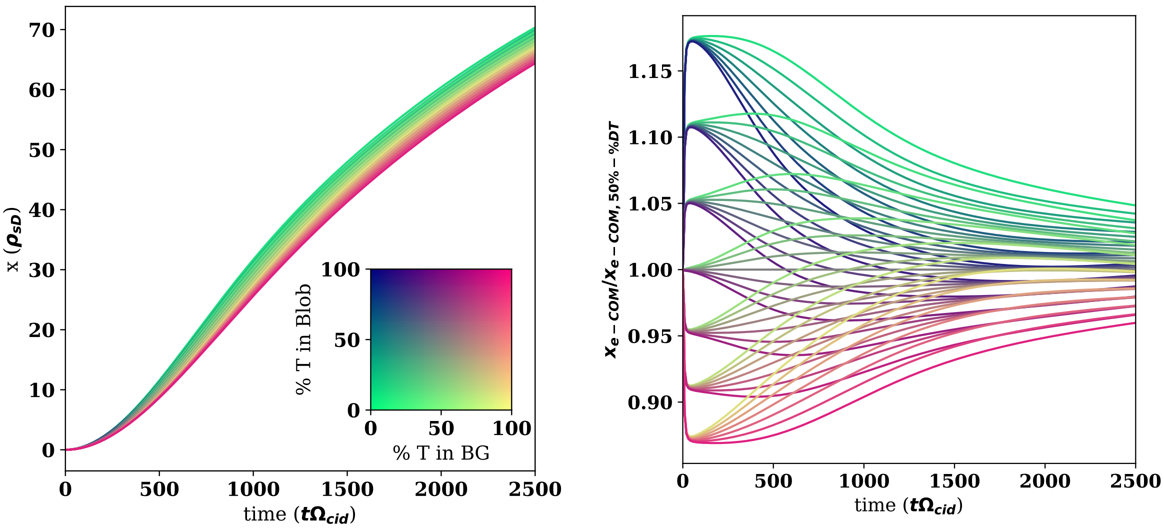

Figure 2: Left: Radial center of mass of electron density. Right: Radial center of mass normalised to 50% D, 50% T.

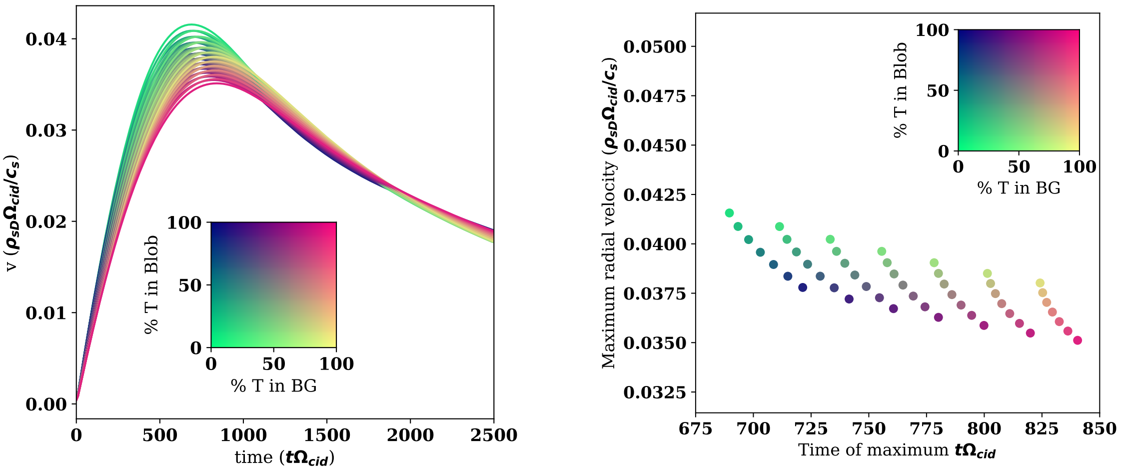

Figure 3: Left: Radial center of mass velocity. Right: Maximum radial velocity against time of occurrence.

Fig. 5 we show the difference both with and without the terms involving ion-ion resistivity at different points in time. We notice that, regardless of the resistivity, the difference between the two species is very small compared to the initial blob perturbation meaning there is little separation between the two species. Comparing the two cases with and without resistive drift (top and bottom) it is evident that the resistive force has a smoothing effect on the species as the differences in the resistive scheme are a factor five smaller than the non-resistive counterpart. This supports our earlier observation in Fig. 4 where we saw a tendency to equilibrate towards a global ratio. It should be noted that the evolution of the electron density distribution is the same for both cases as it equals the sum of ion densities and ion-ion resistive drifts cancel each other.

Earlier in Section II we discussed the issue with asymmetry in $n_\alpha$ when adding densities (see Eq. (34)) that could cause different outcomes when splitting a single species into two. We have therefore performed simulations similar to the above but with a mix of pure deuterium in order to gauge the error introduced by this non-physical artefact. From these simulations, the error amounts to small deviations in the position of blob over time. The errors are of a magnitude of below $10^{-4}$ when normalised to a single species simulation. In regards to the DT runs this can be considered negligible and can not be attributed to the mass effects we see. Furthermore, runs with the same mix ratio in blob and background show errors up to $10^{-7}$. As the resistive drift drives the ratio of the blob and background mix towards equality the error introduced by the asymmetry in summation will diminish over time in general and so the error level is considered acceptable.

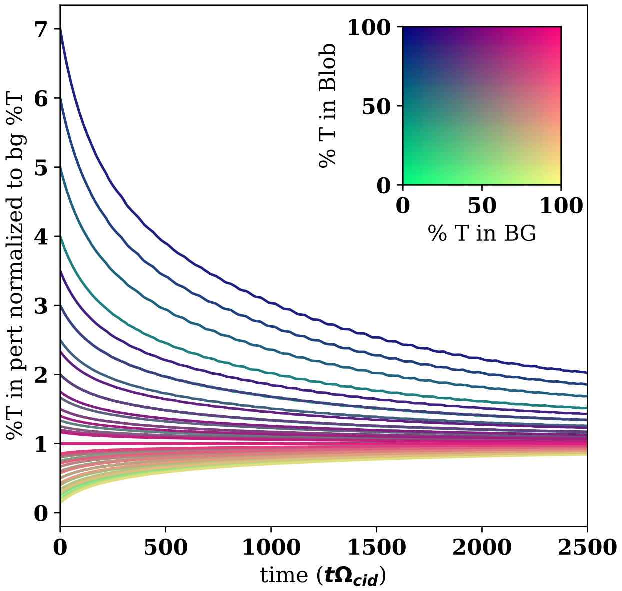

Figure 4: Tritium percentage in blob normalised to background tritium percentage.

## V. DISCUSSION

Based on the Zhdanov 21 moment closure, we have derived a drift ordered fluid model that incorporates multiple ion species and describes the evolution of the density, vorticity and pressure. The model includes consistent ion-ion and electron-ion collisional interactions while maintaining energy conservation. Based on the drift fluid equations for density, vorticity and pressure a computationally workable model was derived and studied through seeded blobs with different mixtures of deuterium and tritium in both the background and blob. We discussed how the mix in the background and blob affect the propagation of the blob individually and found that initially, the deuterium dominated mixes developed the fastest with the background mix playing a leading role. However, as time progresses the mixture in the blob became dominant. We found that both parameters are important for the scaling of the maximum velocity but with the blob mix playing a larger role. Furthermore, we discussed how the resistive forces between the mixes tend to equilibrate so that the mixing ratio is the same everywhere in the plasma. As time progresses the plasma is expected to converge to a system that can be modelled with an effective mass. The asymmetry in summation discussed in II was examined and found to be inconsequential. The mass dependency on the blob propagation suggests that radial transport will decrease as the isotope mix increases the overall mass. In future studies, we plan to investigate the isotope dependency on cross-field particle and energy transport in the edge in a fully developed turbulent plasma. In these studies, we will furthermore account for parametrisation of parallel losses as in Ref. 15.

## VI. ACKNOWLEDGEMENTS

This work has been carried out within the framework of the EUROfusion Consortium and has received funding from the Euratom research and training programme 2014-2018 and 2019-2020 under grant agreement No 633053. The views and opinions expressed herein do not necessarily reflect those of the European Commission.

## REFERENCES

[1] S. P. Hirshman and D. J. Sigmar, “Neoclassical transport of impurities in tokamak plasmas,” Nuclear Fusion **21**, 1079–1201 (1981).

[2] V. M. Zhdanov, “Transport processes in multicomponent plasma,” Plasma Physics and Controlled Fusion **44**, 2283–2283 (2002).

[3] Y. Igitkhanov, “Modelling of Multi-Component Plasma for TOKES (KIT Scientific Reports ; 7564),” (2011).

[4] F. L. Hinton, “Collisional transport in plasma,” Basic plasma physics. 1 (1983).

[5] C. F. Maggi, H. Weisen, J. C. Hillesheim, A. Chankin, E. Delabie, L. Horvath, F. Auriemma, I. S. Carvalho, G. Corrigan, J. Flanagan, L. Garzotti, D. Keeling, D. King, E. Lerche, R. Lorenzini, M. Maslov, S. Menmuir, S. Saarelma, A. C. C. Sips, E. R. Solano, E. Belonohy, F. J. Casson, C. Challis, C. Giroud, V. Parail, C. Silva, and M. V. and, “Isotope effects on l-h threshold and confinement in tokamak plasmas,” Plasma Physics and Controlled Fusion **60**, 014045 (2017).

[6] M. Bessenrodt-Weberpals, F. Wagner, O. Gehre, L. Giannone, J. Hofmann, A. Kallenbach, K. McCormick, V. Mertens, H. Murmann, F. Ryter, B. Scott, G. Siller, F. Soldner, A. Stabler, K.-H. Steuer, U. Stroth, N. Tsois, H. Verbeek, and H. Zoohm, “The isotope effect in ASDEX,” Nuclear Fusion **33**, 1205–1238 (1993).

[7] N. Bonanomi, C. Angioni, P. Crandall, A. D. Siena, C. Maggi, P. Schneider, the ASDEX Upgrade Team, the EUROFusion MST1 Team, and the JET Contributors, “Effect of the isotope mass on the turbulent transport at the edge of l-mode plasmas in ASDEX upgrade and JET-ILW,” Nuclear Fusion **59**, 126025 (2019).

[8] P. Schneider, A. Bustos, P. Hennequin, F. Ryter, M. Bernert, M. Cavedon, M. Dunne, R. Fischer, T. Görler, T. Happel, V. Igochine, B. Kurzan, A. Lebschy, R. McDermott, P. Morel, M. Willensdorfer, and and, “Explaining the isotope effect on heat transport in l-mode with the collisional electron-ion energy exchange,” Nuclear Fusion **57**, 066003 (2017).

[9] B. Scott, “Self-consistent drift wave turbulence, paradigm for transport,” Plasma Physics and Controlled Fusion **34**, 1977–1983 (1992).

[10] H. Bufferand, P. Tamain, S. Baschetti, J. Bucalossi, G. Ciraolo, N. Fedorczak, P. Ghendrih, F. Nespoli, F. Schwander, E. Serre, and Y. Marandet, “Three-dimensional modelling of edge multi-component plasma taking into account realistic wall geometry,” Nuclear Materials and Energy **18**, 82–86 (2019).

[11] O. H. H. Meyer and A. Kendl, “Isotope effect on gyro-fluid edge turbulence and zonal flows,” Plasma Physics and Controlled Fusion **58**, 115008 (2016).

[12] O. H. H. Meyer and A. Kendl, “Isotope effect on blob-statistics in gyrofluid simulations of scrape-off layer turbulence,” Nuclear Fusion **57**, 126066 (2017).

[13] O. H. H. Meyer and A. Kendl, “Isotope effect on filament dynamics in fusion edge plasmas,” Plasma Physics and Controlled Fusion **59**, 065001 (2017).

[14] J. Madsen, V. Naulin, A. H. Nielsen, and J. J. Rasmussen, “Collisional transport across the magnetic field in drift-fluid models,” Physics of Plasmas **23**, 032306 (2016).

[15] A. H. Nielsen, J. J. Rasmussen, J. Madsen, G. S. Xu, V. Naulin, J. M. B. Olsen, M. Løiten, S. K. Hansen, N. Yan, L. Tophøj, and B. N. Wan, “Numerical simulations of blobs with ion dynamics,” Plasma Physics and Controlled Fusion **59**, 025012 (2017).

[16] S. I. Braginskii, “Transport Processes in a Plasma,” Reviews of Plasma Physics **1**, 205 (1965).

[17] E. V. Belova, “Nonlinear gyroviscous force in a collisionless plasma,” Physics of Plasmas **8**, 3936–3944 (2001).

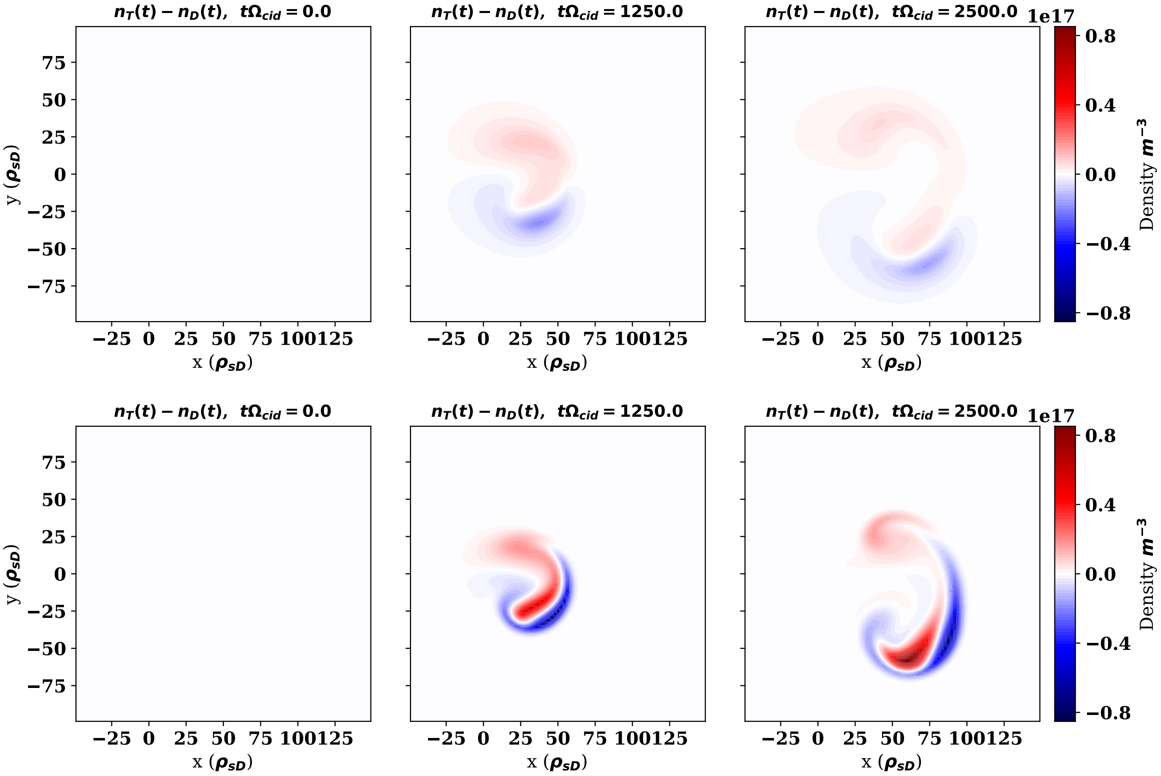

Figure 5: Ion density difference for the case of 50% D, 50% T in both background and perturbation taken at different snapshots. Top three are with ion-ion resistivity drift enabled while bottom three are without ion-ion resistivity.

[18] J. Gath and M. Wiesenberger, “Consistency in drift-ordered fluid equations,” Physics of Plasmas **26**, 032304 (2019).

[19] A. Zeiler, J. F. Drake, and B. Rogers, “Nonlinear reduced Braginskii equations with ion thermal dynamics in toroidal plasma,” Physics of Plasmas **4**, 2134–2138 (1997).

[20] M. Wiesenberger, L. Einkemmer, M. Held, A. Gutierrez-Milla, X. Sáez, and R. Iakymchuk, “Reproducibility, accuracy and performance of the Feltor code and library on parallel computer architectures,” Computer Physics Communications **238**, 145–156 (2019).

[21] H. F. WALKER and P. NI, “Anderson acceleration for fixed-point iterations,” SIAM Journal on Numerical Analysis **49**, 1715–1735 (2011).

[22] J. Olsen, J. Madsen, A. H. Nielsen, J. J. Rasmussen, and V. Naulin, “Temperature dynamics and velocity scaling laws for interchange driven, warm ion plasma filaments,” Plasma Physics and Controlled Fusion **58**, 044011 (2016).

[23] M. Held, M. Wiesenberger, J. Madsen, and A. Kendl, “The influence of temperature dynamics and dynamic finite ion larmor radius effects on seeded high amplitude plasma blobs,” Nuclear Fusion **56**, 126005 (2016).

[24] J. Madsen, O. E. Garcia, J. Stærk Larsen, V. Naulin, A. H. Nielsen, and J. J. Rasmussen, “The influence of finite Larmor radius effects on the radial interchange motions of plasma filaments,” Physics of Plasmas **18**, 112504 (2011).

[25] R. Kube, O. E. Garcia, and M. Wiesenberger, “Amplitude and size scaling for interchange motions of plasma filaments,” Physics of Plasmas **23**, 122302 (2016).

[26] R. D. Hazeltine, “Coulomb collision operator,” Tech. Rep., University of Texas , 27 (2006).

[27] W. Fundamenski and O. E. Garcia, “Comparison of Coulomb Collision Rates in the Plasma Physics and Magnetically Confined Fusion Literature,” EFDA-JET-R. , 17 (2007).

#### 4.1.1.3 Postlude

The paper introduced the MIHESEL model derived from the moment equations the drift fluid expansion of the momentum equation. In relation to this, it was shown that the model was energy conserving in the form given in the paper:

$$\int \mathrm{d}V \sum_{\alpha} \left( m_\alpha n_{\alpha,0} \frac{|\nabla_\perp \phi|^2}{2} + \frac{3}{2} p_\alpha \right) + \frac{3}{2} p_e = 0 \tag{4.1}$$

Hence the full energy, in the form of fluid kinetic and thermal energy, is conserved. For the full MIHESEL model given in Eqs. (2.143) to (2.146), which contain the parallel parametrisation, the conservation of energy contains a non-zero right-hand side due to the inclusion of parallel loss terms and sources. Following the theoretical discussion, the first use of the model was presented. In this, simulations of seeded blobs with a variety of mixes of deuterium and tritium in background and perturbation were investigated. It was found that overall the inclusion of tritium slowed down the blob propagation compared to a deuterium dominated blob. The exact dependency was found to be on whether the deuterium was in the background or the perturbation initially. A velocity scaling of the effect of the background and perturbation mix on the maximum radial velocity of the blobs was found as:

$$\begin{aligned} &V_{max}(m_{\mathit{eff},b}, m_{\mathit{eff},bg}) \\ &= 0.055(\pm 0.001) \left( m_{\mathit{eff},b}^{-0.34(\pm 0.01)} + m_{\mathit{eff},bg}^{-0.25(\pm 0.01)} \right). \end{aligned} \tag{4.2}$$

This shows that while the maximum velocity depends on both types of mixes, the perturbation mix is slightly more dominant. That the background is also important, reveals itself in the fact that the perturbation mix tends towards the background mix as seen in fig. 4 in the paper. This homogenisation of the mixture ratio is caused by the resistive force between species. Overall, it can be concluded that for the case of uniform ratio in the initial perturbation and background, the velocity scaling falls well in line with the scaling found in [23].

**Poloidal motion** In the paper, the radial propagation of the blob was the primary focus of the numerical simulation. The MIHESEL model does, like its predecessor the HESEL model, contain lower-order finite Larmor radius effects through the gyro-viscous stress tensor and the generalised vorticity. The resulting behaviour is that there is a poloidal motion of the blob. This is also seen in [52], [92], [96] where the blob moves in the negative $\boldsymbol{B} \times \nabla B$

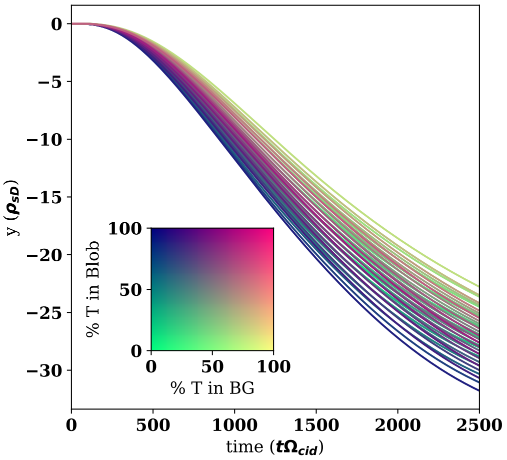

Figure 4.1: Poloidal center of mass position over time for DT simulations.

direction. In the particle picture, this motion results from a gyrating particle transversing a non-uniform electric field. The variation of the electric field happens on the scale of the blob width. As a reminder, the gyro-radius is given as:

$$\rho_\alpha = \frac{m_\alpha v_{\perp,\alpha}}{|q_\alpha|B} = \frac{\sqrt{T_\alpha m_\alpha}}{|q_\alpha|B} \tag{4.3}$$

which shows that higher mass means larger gyro-radius. This implies that a heavy particle would experience a more varied electric field compared to a lighter particle and so should cause increased poloidal motion. In Fig. 4.1 the centre-of-mass position in the poloidal direction over time is shown. In this, it is observed that it is the isotope mixture in the blob that is the determining value regarding the magnitude of the poloidal centre-of-mass position. This falls well in line with the notion that heavier particles have larger gyro-radii than lighter (assuming the same charge) and so exhibit more pronounced poloidal motion. Interestingly, it is the mixtures where the background is deuterium dominated and the perturbation is tritium dominated that experiences the largest poloidal propagation.

### 4.1.2 Deuterium helium blobs

In the previous subsection, blobs with mixes of deuterium and tritium were studied as these are the main components of a burning plasma. Naturally, in a true burning plasma, Helium will also be a main component of the plasma mix as it is the ash of the DT fusion reaction as stated in Eq. (1.1).

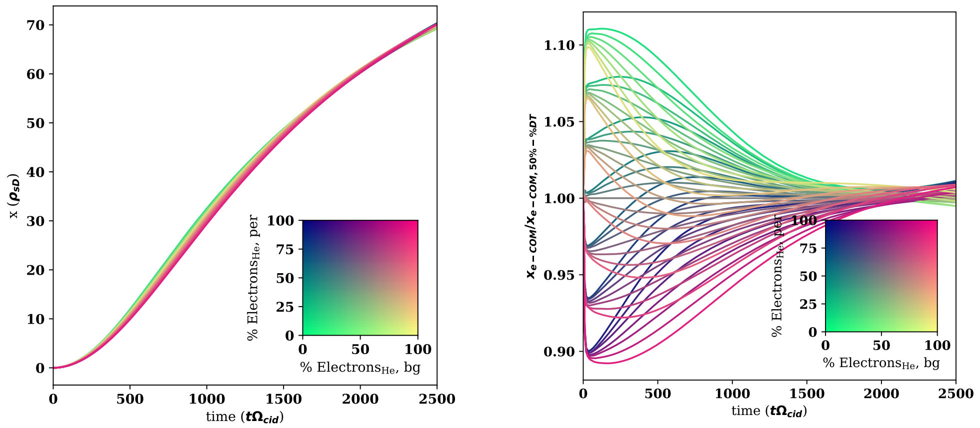

Figure 4.2: Left: Deuterium helium radial center-of-mass position over time. Right: Normalised center of mass.

Furthermore, doubly ionised helium four is interesting as it has the same mass charge ratio as deuterium, meaning it is the same gyro frequency for both species. In this section, a similar simulation scan of 49 individual mixtures as the one found in the paper is performed but with helium instead of tritium. To make a comparable situation, the electron density is the same for all blob simulation. This means that when helium substitutes tritium, the helium density will only be half what it would be if it were tritium. The density of deuterium is unchanged.

The radial position of the centre-of-mass is shown in Fig. 4.2 along with normalisation regarding the case where 50% of the electrons are contributed by the deuterium and the rest from the helium. Moving forward, the mixtures will be referred to by the amount of electrons each species supplied, e.g., $75\% - 25\%$ means the helium supplied 25% of the electrons. In Fig. 4.2 left it is observed that the difference in the evolution of the centre-of-mass for all mixtures is less pronounced than what was observed in the DT case presented in the paper. This is also supported in the Fig. 4.2 right with the normalised positions where the initial deviation goes up to about 1.12 where for the DT case it was around 1.17. Subsequently, all curves tend towards 1.0. From Fig. 4.2 right it is also seen that there is an initial grouping according to the perturbation mix where groups with large amounts of deuterium have higher initial acceleration, and vice versa. In the very beginning, the background mix has a minor influence on the acceleration. However, as time progresses, the combination of the background mix and perturbation mix plays an increasing role.

Looking into the velocity of the centre of mass, shown in Fig. 4.3 left,

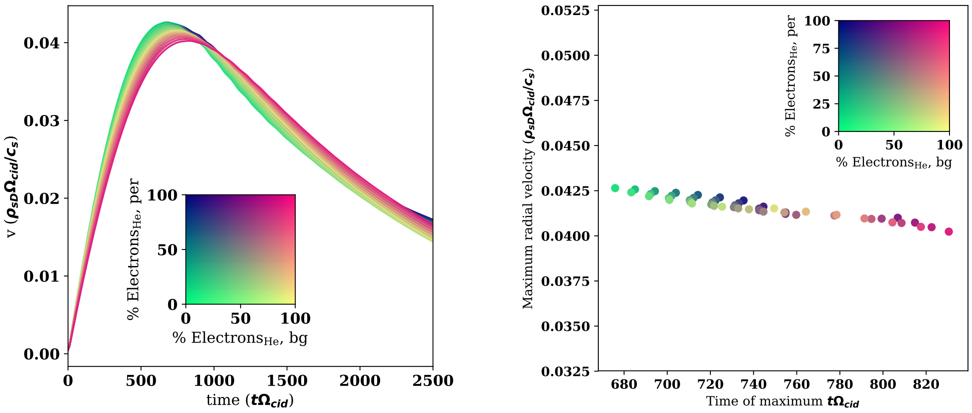

Figure 4.3: Left: Deuterium-Helium radial centre of mass velocity. Right: Maximum center of mass velocity against time of occurence.

it is evident that the behaviour is very similar to that of DT, i.e. that the more deuterium, the higher the maximum radial velocity is. From a simple balance of terms, a scaling law can be found from the vorticity equation when neglecting the viscosity term. Assuming equal width for all species, the scaling comes to:

$$\boldsymbol{u}_{rad,blob} \sim \sqrt{\frac{\sigma}{R}\frac{\sum_\alpha \delta p_\alpha + \delta p_e}{\sum_\alpha m_\alpha n_{\alpha,0}}} \tag{4.4}$$

where $\sigma$ is the width of the blob, $\delta p_s$ is the amplitude of the of species perturbation. From this scaling, it can be seen that for a pure helium plasma, the maximum blob velocity should be a factor 3/4 slower than a similar situation containing pure deuterium. However, from Fig. 4.3 right, it is observed that the ratio of magnitudes of the maximum velocity of the deuterium and helium dominated simulations, is close to unity. Here it is also found that the helium dominated mixes reach their maximum velocity later than a deuterium dominated mix. This shows that the helium mix has a slower acceleration, but also that in accelerated over a longer time period. A possible explanation for the discrepancy in the velocity scaling can be found when taking into account the poloidal motion.

Regarding the poloidal motion, it was previously discussed that the magnitude of the poloidal motion depends on the gyro-radius compared to the blob width. As the gyro-radius of doubly ionised helium-four is a factor $\sqrt{2}$ smaller than deuterium it is expected that the poloidal motion is decreased as the amount of Helium increases. The results of the poloidal centre of mass are shown in Fig. 4.4 where this point is clear. The deuterium dominated mix

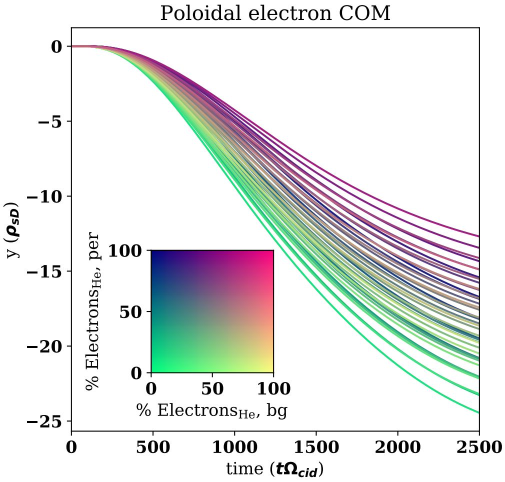

Figure 4.4: Poloidal centre of mass position

exhibits the most pronounced poloidal motion. When the deuterium dominated both background and perturbation the blob experiences most poloidal motion. This is in contrast to the DT simulations where a tritium dominated blob in a deuterium dominated background showed to most poloidal behaviour. Hence, the background mix can either enhance or diminish the effect that the perturbation mix has on the poloidal behaviour. Since deuterium is favoured in the scaling compared to helium, it seems to enhance the poloidal motion of the deuterium (or tritium in case of DT mix) dominated perturbation. Returning to the matter of the maximum radial blob velocity scaling, it was noted that in general helium blobs were not slower than the deuterium by the amount prescribed by the scaling. However, this scaling only considers the radial motion. But as it was just seen, the deuterium also exhibits more poloidal motion than the helium counterpart, meaning their trajectories are different. This could account for the discrepancy between the scaling and the observed behaviour of the maximum radial velocity.

Regarding transport in the SOL/edge, it is evident that while doubly charged helium is heavier than deuterium, the higher charge nearly cancels the transport reducing effect of the increased mass. Hence, for a helium deuterium plasma, it is to be expected that the transport across the last closed flux surface is comparable to that of a pure deuterium plasma.

## 4.2 2D Turblence

In the previous section, isotope effects on seeded blobs were investigated. Seeded blobs are an idealised area of study, although much can be inferred with regards to transport. However, to get statistics of the transport in the outer edge blob simulations are no longer sufficient. In the region of the plasma where the edge of the core plasma with closed magnetic field lines meets the scrape-off-layer, with open magnetic field lines, the plasma dynamics is highly dominated by turbulent transport. Understanding turbulent transport is highly important in the realisation of a future fusion power plant. It is therefore of interest to study the effects of isotope mixtures in such a setting. Turbulence has been studied in a variety of settings in regards to transport in the edge/SOL region, e.g.,[16], [18], [20]. In particular, the influence of ion temperature dynamics [62] and neutrals [51] on the development of turbulent transport have been studied using the HESEL model. Additionally, gyro-fluid approaches have also been employed in the study of the edge turbulence [21].

### 4.2.1 Simulation setup

In turbulence simulations, the domain is a 2D slab, perpendicular to the magnetic field, located at the outboard midplane of a tokamak. As such, the simulation domain can be divided into two main regions, namely the edge and the sol. Within each region, there are further two regions [62]. For the closed field line region, which corresponds to the edge, there is an inner edge region where an initial profile is forced, while the outer edge region allows for turbulence evolution. The open region contains the scrape-off-layer (SOL) and the wall shadow region where there is damping according to the parallel parametrisation given in Section 2.2.3.2. The difference between these two regions is the strength of the parallel loss terms, where the wall region will have much higher losses. A schematic of the domain is seen in Fig. 4.5.

The density and temperature profiles are initialised as:

$$n_\alpha = n_{bg} + \left(n_{inner,\alpha} - n_{bg,\alpha}\right)\frac{1}{2}\tanh\left(1 + \operatorname{sign}\left[\frac{x - x_{n_\alpha,c}}{a_{n_\alpha}}\right]\right) \tag{4.5a}$$

$$\begin{aligned} T_s = &\left(-\frac{\sqrt{T_{inner,s}} - 1}{x_{inner}}(x)\right) \\ &\cdot\left(T_{s,bg} + \left(\sqrt{T_{s,inner}} - T_{s,bg}\right)\frac{1}{2}\tanh\left(1 + \operatorname{sign}\left[\frac{x - x_{T_s c}}{a_{T_s}}\right]\right)\right) \end{aligned} \tag{4.5b}$$

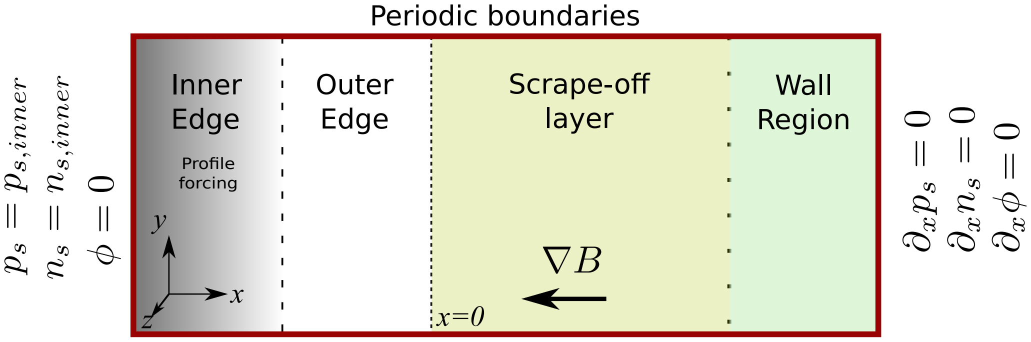

Figure 4.5: Setup of simulation domain with the closed field lines edge region and open field lines SOL and wall region.

where $n_{bg}$ is the background density and $n_{inner}$ is the density at the inner boundary. The shift $x_{n/T,c}$ caries little importance as the initial profile will degrade and become unstable. Hence, for this work, it is simply set as the midpoint between the profile forcing region. The parameter $a$ specifies the width of the profile. Naturally $n_{inner} > n_{bg}$. The same goes for the temperature. As the MIHESEL model doesn't evolve the temperature, but instead the pressure, an initial condition for the pressure is needed. This is simply obtained by multiplying the density and temperature profiles. For the ion temperature, it is required from the closure that $T_\alpha = T_\beta$, while the electron temperature does not have to equal the ion temperature. The potential is initially zero everywhere. In the way the profiles are given in Eq. (4.5) turbulence will only develop due fluctuations arising from finite numerics of a computer. Since these fluctuations are small, turbulence will only develop over long periods of time. To accelerate the initial destabilisation of the profile, a small perturbation, or blob, is introduced onto the initial density profile. Following [62] the inner boundary of the domain contain a forcing region where the profiles are forced toward the prescribed profiles in order to maintain the turbulent behaviour. For a generic field $f$ this is expressed as:

$$\frac{\partial}{\partial t} f = \cdots + \frac{f_{init} - f}{\tau_{force}} \tag{4.6}$$

where $\tau_{force}$ is the forcing time. In effect, this is a source terms that emulates a continuous injection of particles and energy into the edge from the core. Furthermore, as mentioned in Section 2.2.3.2, the parallel dynamics are parametrised with closed field line losses (Eqs. (2.133) and (2.134)) and open field line losses (Eqs. (2.129) to (2.132)). To enforce these regions, each terms is multiplied by a tanh function corresponding to their region.

To keep the simulation stable it has been found that forcing a minimum background in the SOL and wall region is necessary. The way this is done is by adding a term to the right hand side of the MIHESEL equations:

$$f_{min,force} = \begin{cases} \frac{f-f_{min}}{\tau_{bg}}, & \text{if} f < f_{min} \\ 0, & \text{otherwise} \end{cases} \tag{4.7}$$

where $f$ is the field and $\tau_{bg}$ is some relaxation time. This means that if the, e.g., the density drops below some minimum, it will be forced towards this minimum. As such, it is similar to the profile forcing in the inner edge region with the difference that the forcing is not active when the values are above the minimum. In principle the SOL and wall region are rather dilute in both density and temperature expect when filaments are ejected into the SOL from the edge. Additionally, some amount of recycling does occur which 'feeds' the SOL and so the background forcing implemented with Eq. (4.7) can be viewed as a recycling source.

Taking this into account, the dependence of isotope composition on the turbulent transport is examined with a parameter scan over both the inner boundary composition and the minimum background composition in the SOL/wall region.

For all simulations, the electron density is set such such that the value at the inner boundary is $n_{inner,e} = 1.5n_0$ where $n_0 = 1.5 \cdot 10^{21} m^{-3}$ is the reference density. The background floor in the SOL/wall region is $n_{floor,e} = 0.25n_0$. The ions are comprised of deuterium and tritium and the mixes in the inner boundary and the minimum background are given in Table 4.1.

The reference temperature is set to be $T_0 = 20eV$ with the inner electron and ion temperatures set at $T_s = 4T_0$ for all species. For the background floor value, it is set at $T_{s,bg} = 0.25T_0$. The dimension are $l_x = 10.5cm = 250\rho_D$ in the radial direction and $l_y = 8.4cm = 200\rho_D$ in the poloidal direction where $\rho_D = \sqrt{(Te/m_D)}$ is the reference length. The magnetic field at the last closed flux surface is $B_0 = 2T$ with a major radius $R = 1.65$, minor radius $r = 0.5$ and safety factor of $q = q_{95} = 6$. In regards to Fig. 4.5, the edge region is set to have a width of $100\rho_D = 4.2cm$. The same goes for the SOL region while the wall region has a width of $2.1cm$. The widths of the initial profiles are set to $a = 10$ for both density and temperature. For the radial direction, the inner boundary conditions are Dirichlet, while the outer are Neumann for $n_\alpha$, $p_s$ and $\phi$. The poloidal direction features periodic boundary conditions.

For the numerical domain, the grid size was chosen to be $N_x = 480$ and $N_y = 384$ for a grid spacing of $\Delta x = \Delta y = 0.52\rho_D$. The number of polynomial coefficients was chosen to be 1. The optimal choice would have been a higher order such as 3, but this case proved to be prohibitively expensive in the inversion of the potential ion pressure coupling matrix (Eq. (3.2)). The jump

| Inner mixture composition | | Outer background minimum | |
|---|---|---|---|
| $\%D$ | $\%T$ | $\%D$ | $\%T$ |
| 75 | 25 | 75 | 25 |
| 75 | 25 | 50 | 50 |
| 75 | 25 | 25 | 75 |
| 50 | 50 | 75 | 25 |
| 50 | 50 | 50 | 50 |
| 50 | 50 | 25 | 75 |
| 25 | 75 | 75 | 25 |
| 25 | 75 | 50 | 50 |
| 25 | 75 | 25 | 75 |

Table 4.1: Table of setups for mixes on inner boundaries and background minimum floor with a total of 9 mixtures

factor (see Eq. (3.36)) in the elliptic operator was set to $\alpha = 2.2$. This was chosen as it was observed to introduce sufficient numerical diffusion to avoid oscillations particularly in $\nabla^2\phi$. Lastly, the time resolution was chosen to be $\Delta t = 0.25\Omega_{c,D}^{-1}$ where the parameters for the nonlinear solver are in given in Table 3.2. Snapshots of the density, pressure and temperature at $t = 0.4ms$ are shown in Fig. 4.6. It is observed that the structure of the plasma if dominated by filaments. This is in agreement with other results presented in e.g. [62]. This filamentary structure is seen in both density and pressure profiles. The same also holds for the electron temperature, whereas the ion temperature displays far more diffusion, with less clear structures.

In the initial phase, when the turbulence is initiated by a perturbation in the initial profile, a large amount of material and energy are expelled from the edge. This initial transient event is rather extreme and is not a recuring event seen in general in turbulence simulation. To show this, it is instructive to study the advective flux of the particles and thermal energy. The advective flux of some quantity $C$ is given by:

$$\boldsymbol{\Gamma}_{\boldsymbol{n}} = C\boldsymbol{u} \tag{4.8}$$

For this work, it is the transport across the last closed flux surface that is of interest as it gives a measure of the amount of material and energy that is transported from the closed field lines to the open. The main velocity driver of the radial flux is the $E \times B$ drift. Considering this, and using Eq. (4.8),

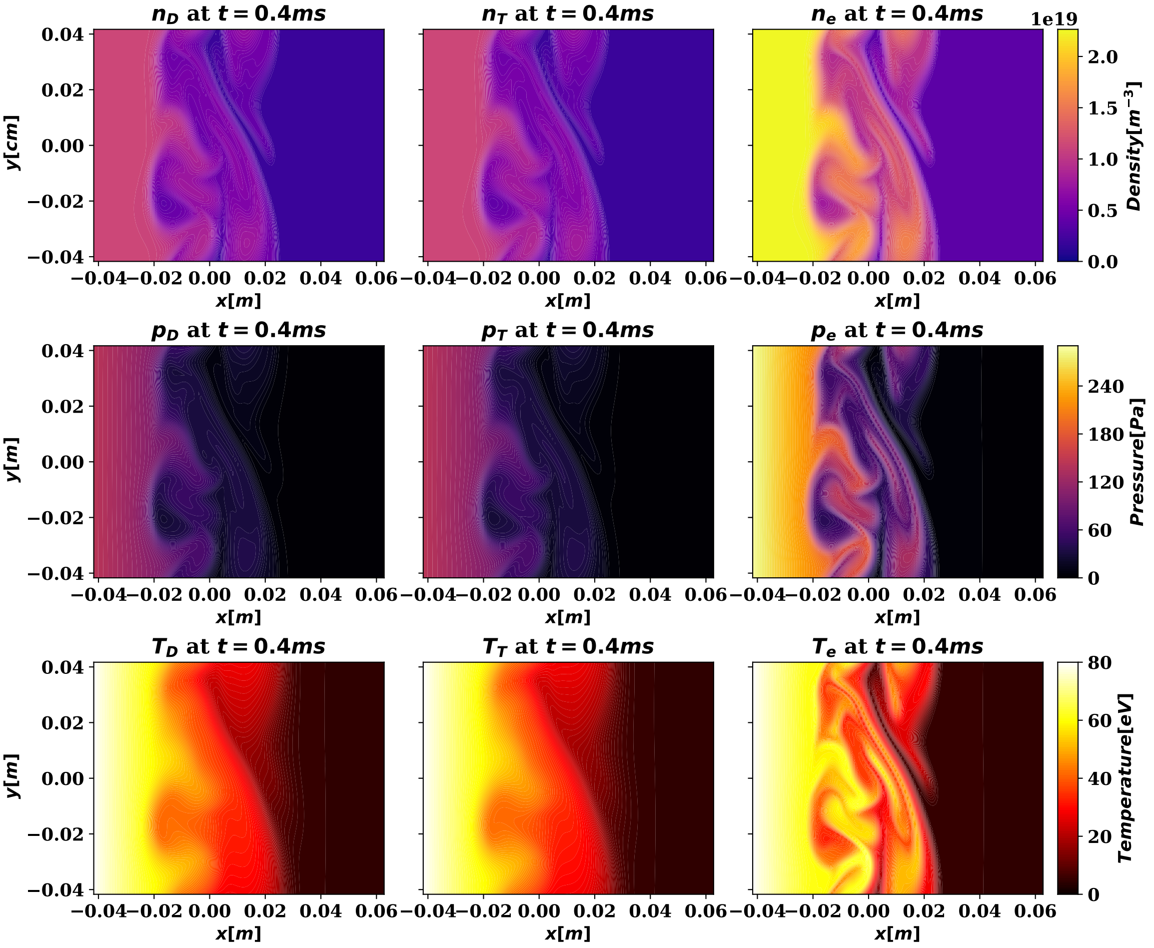

Figure 4.6: Snapshots of density (top), pressure (middle) and temperature (bottom) at $t = 0.4ms$ for deuterium (left), tritium (middle), electrons (right). Simulation mix is Inner: 50%D 50%T; BG: 50%D 50%T,

the radial particle and heat flux are given as:

$$\Gamma_n(x,y,t) = -n\frac{\partial_y \phi}{B} \quad \text{and} \quad \Gamma_p(x,y,t) = -p\frac{\partial_y \phi}{B} \tag{4.9}$$

where $\phi$ is the electric potential. The poloidally averaged radial flux across the LCFS for possible mixes in Table 4.1 is shown in figure Fig. 4.7.

It is observed that the initial phase, up to $t \sim 0.2ms$, exhibit large fluctuations in the flux. This is particularly clear for the Inner: $75\%D, 25\%T$ mixes seen in the top row. This is the extreme transient event discussed before. It is noted that such an event does not occur again after this. Curiously, for each subgroup of the mixes in the inner region (rows Fig. 4.7), it is the compositions where the inner mix is the same as the outer background mix, that have the largest initial spikes within each row. This seems to indicate that the composition in SOL/wall regions has some amount of influence on the processes happening in the inner region. Disregarding the initial phase, it is evident that the flux is governed by large fluctuations, which is characteristic of intermittent turbulence.

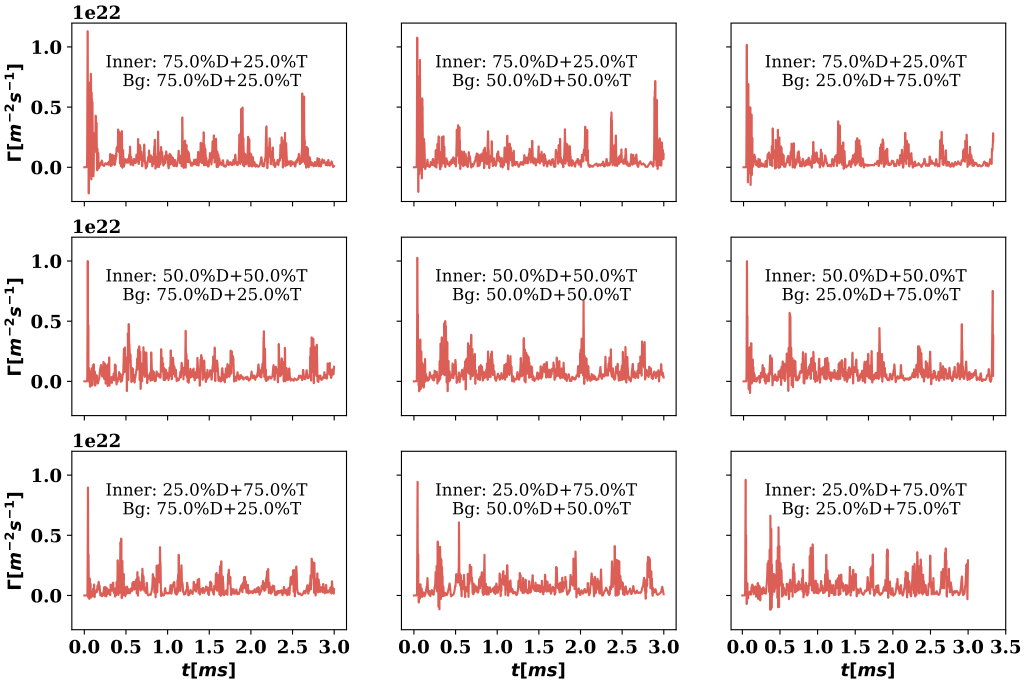

Figure 4.7: Electron particle flux for each composition.

To investigate the influence of the mixtures on the radial flux, a probability density function of the radial flux is produced using Gaussian kernel density estimation[1]. Only the flux data after $t = 0.2ms$ are included to exclude the initial erratic fluctuations mentioned above. The results are compared according to the mixes in the inner region and the outer background. The resulting comparisons are shown in Fig. 4.8 for the density flux with the six comparisons (corresponding to three row-wise comparisons and three column-wise comparisons of Fig. 4.7).

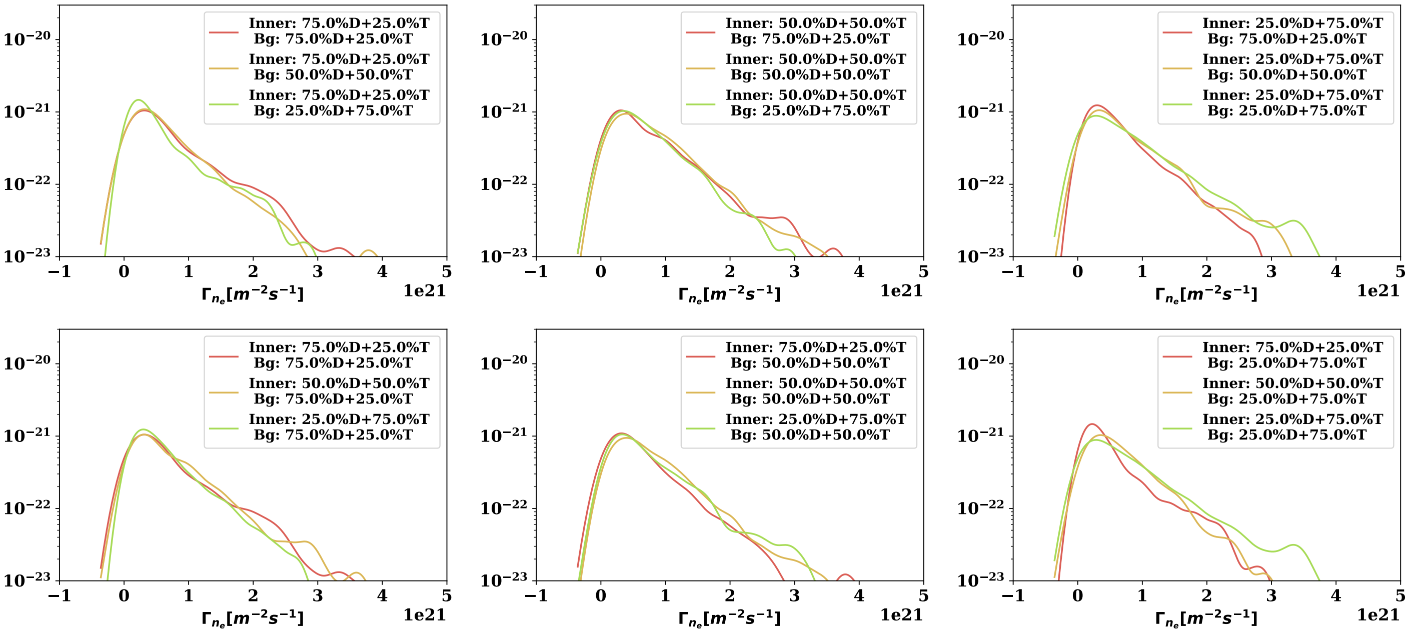

Figure 4.8: PDFs for electron flux across the last closed flux surface with row wise and column wise comparisons in relation to Fig. 4.7.

Descriptors of each pdf of both particle and heat flux are given in Tables 4.2 and 4.3. From the descriptors of both flux distributions, it is observed that the particle and heat flux across the LCFS increases as the amount of tritium in the inner region forcing composition compared to deuterium, increases. E.g. the deuterium dominated mix (top left in Fig. 4.8) has a mean flux of $7.3 \cdot 10^{20} m^{-2} s^{-1}$ against $8.3 \cdot 10^{20} m^{-2} s^{-1}$ for the tritium dominated mixture (bottom right in Fig. 4.8). Within each subgroup of the inner mixture, it is further observed that when the inner mixture is equal to that of the mixture of the outer minimum, the flux is at its highest. This corresponds to the diagonal from top left to bottom right in Fig. 4.7. That the flux across the last closed flux surface increases as the mass increases is in contrast to what was observed in the simulations of the DT blobs in Section 4.1.1 and what

---

[1] Computations performed using Scipy's Gaussian Kernel density estimation function.

| Mixture<br>Inner: %D, %T, BG:%D, %T | Mean<br>$10^{20}m^{-2}s^{-1}$ | Standard dev.<br>$10^{20}m^{-2}s^{-1}$ | Skewness | Kurtosis |
|---|---|---|---|---|
| 75.0, 25.0; 75.0, 25.0 | 7.3 | 7.09 | 2.43 | 8.87 |
| 75.0, 25.0; 50.0, 50.0 | 6.79 | 7.1 | 3.28 | 16.89 |
| 75.0, 25.0; 25.0, 75.0 | 5.75 | 5.48 | 1.86 | 4.08 |
| 50.0, 50.0; 75.0, 25.0 | 7.33 | 6.92 | 1.79 | 4.11 |
| 50.0, 50.0; 50.0, 50.0 | 8.2 | 7.11 | 2.19 | 8.02 |
| 50.0, 50.0; 25.0, 75.0 | 7.33 | 7.05 | 2.96 | 15.15 |
| 25.0, 75.0; 75.0, 25.0 | 6.59 | 6.0 | 2.05 | 5.96 |
| 25.0, 75.0; 50.0, 50.0 | 7.39 | 6.77 | 1.97 | 5.97 |
| 25.0, 75.0; 25.0, 75.0 | 8.31 | 8.09 | 1.89 | 5.22 |

Table 4.2: PDF descriptors for electron particle flux across the last closed flux surface.

| Mixture | Mean<br>$kJm^{-2}s^{-1}$ | Standard dev.<br>$kJm^{-2}s^{-1}$ | Skewness | Kurtosis |
|---|---|---|---|---|
| 75.0, 25.0; 75.0, 25.0 | 8.27 | 8.49 | 2.61 | 10.42 |
| 75.0, 25.0; 50.0, 50.0 | 8.05 | 8.76 | 3.16 | 15.47 |
| 75.0, 25.0; 25.0, 75.0 | 7.54 | 7.48 | 1.94 | 4.52 |
| 50.0, 50.0; 75.0, 25.0 | 9.03 | 8.8 | 1.83 | 4.15 |
| 50.0, 50.0; 50.0, 50.0 | 9.63 | 8.54 | 2.19 | 7.68 |
| 50.0, 50.0; 25.0, 75.0 | 8.98 | 8.96 | 2.73 | 12.07 |
| 25.0, 75.0; 75.0, 25.0 | 9.28 | 8.83 | 2.21 | 6.8 |
| 25.0, 75.0; 50.0, 50.0 | 9.37 | 8.93 | 2.0 | 5.55 |
| 25.0, 75.0; 25.0, 75.0 | 9.89 | 9.86 | 1.87 | 4.78 |

Table 4.3: PDF descriptors for electron heat flux across the last closed flux surface.

has been found using gyro-fluid models [21]. In the blob simulations, it was found that the maximum radial velocity scaled inversely with the mass of the ion in the blob. I.e. the more deuterium the faster the blob. This was related to the flux and it was stated that a deuterium dominated plasma would lead to higher flux. However, it should be noted that the 2D blob simulations, only involved 2D effects, while these simulations also contain parametrisation of the parallel dynamics. In particular, the drift wave parametrisation given in Eq. (2.134), affects the electron density and pressure, and consequently, it appears in the vorticity equation. Since the ion density and pressure are coupled to the vorticity, the drift waves also affect the ion pressure and density profiles where it acts as a damping term. While the deuterium dominated simulation has a smaller flux it is, however, observed both from the flux in Fig. 4.7 and its statistical descriptors in Table 4.2 that more extreme events appear in the deuterium case. This shows up as increasingly large spikes in the flux signal, and as a larger kurtosis for the deuterium dominated mix. Hence, this indicates that if there are large amounts of deuterium in the inner region and the outer region, then the plasma will be prone to more extreme events. Additionally, the deuterium dominated plasmas appear to be more dilute in density and energy. This is seen in Figs. 4.9 and 4.10 where the poloidally and time-averaged profiles are lower than the tritium dominated profiles. The time averaging is done over time entire simulation run, except for the initial phase. This suggests that the deuterium mixes are not able to build up profiles that could lead to large fluxes.

A simple test of pure deuterium and pure tritium has also been performed as a simple test of the model in a single species case. The results for the fluxes are shown in fig. Fig. 4.11, although these are for a shorter time than the DT mix. The average particle flux in these cases after the initial transient phase are $7.8 \cdot 10^{20} m^{-2} s^{-1}$ with standard deviation of $7.1 \cdot 10^{20} m^{-2} s^{-1}$ for deuterium and $5.15 \cdot 10^{20} m^{-2} s^{-1}$ with standard deviation $\pm 6.02 \cdot 10^{20} m^{-2} s^{-1}$ for tritium. This is a substantial difference that is more in line with the expected decrease in transport when the mass increases. This goes against the results obtained with the mixtures presented above. In this regard, it is hard to imagine that the flux would vary as such in between the pure D and T runs but should rather follow the same trend with decreased flux with increased mass.

That the flux increased as the amount of tritium in the inner region increased deviates from what is expected and should be further tested. In this regard, it should be noted that the number of large events for e.g. the deuterium dominated simulation, is $\sim 10$ suggesting that the simulation needs to be run for longer times to get better statistics on the large events. That there is possibly too few large events is also evident when examining the kurto-

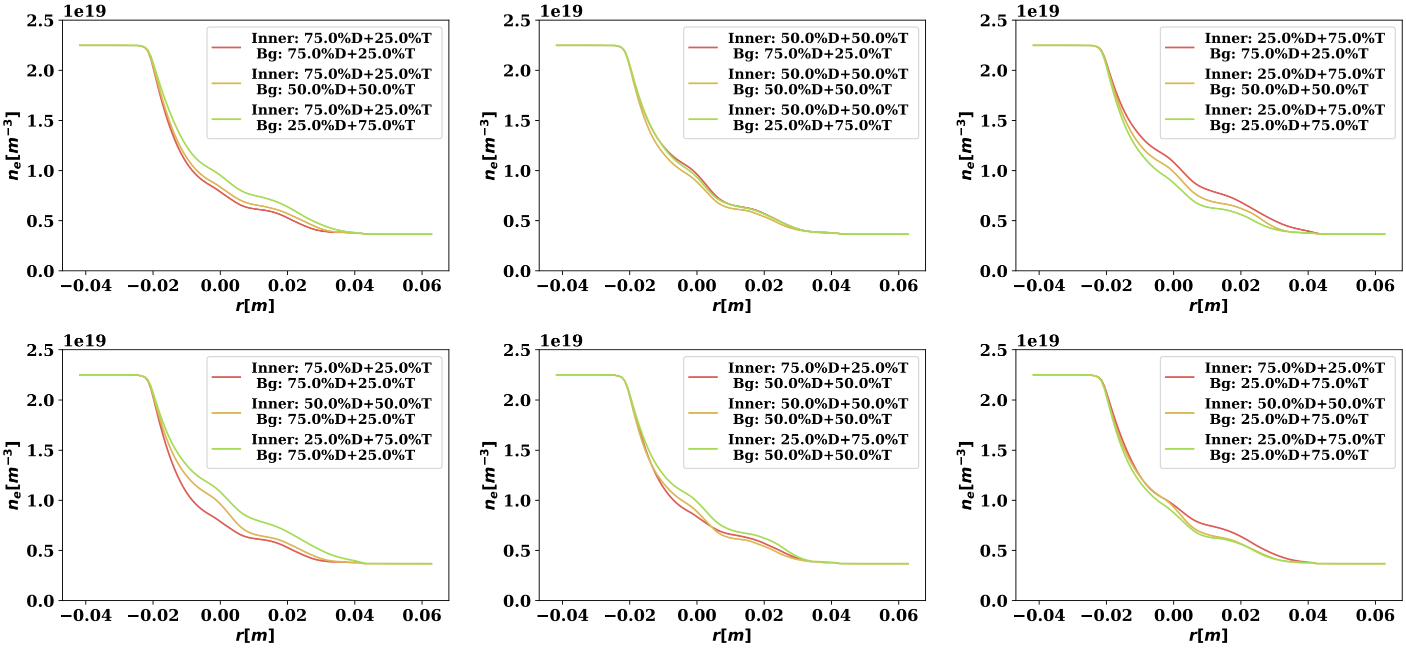

Figure 4.9: Temporally and poloidally averaged radial electron density profiles with row wise and column wise comparisons in relation to Fig. 4.7.

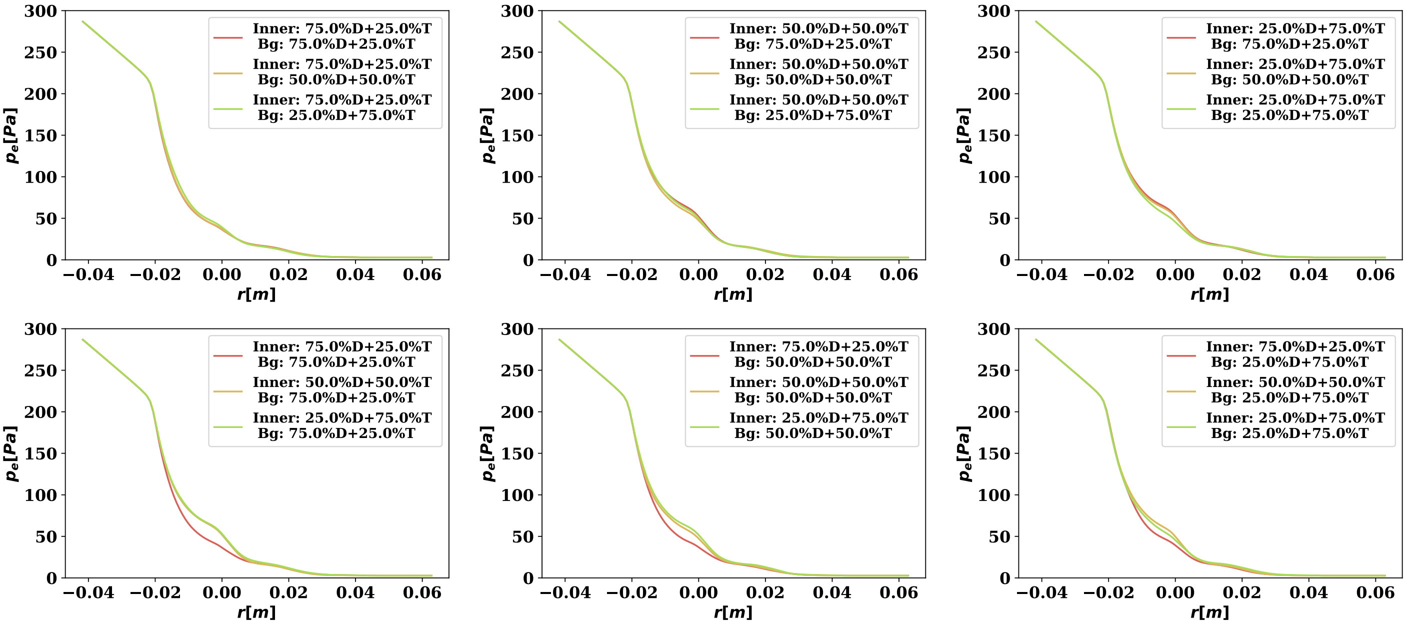

Figure 4.10: Temporally and poloidally averaged radial electron pressure profiles with row wise and column wise comparisons in relation to Fig. 4.7.

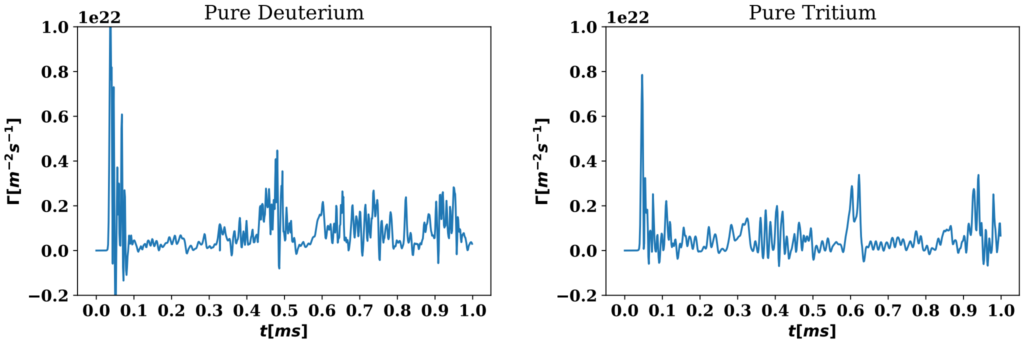

Figure 4.11: Particle flux for pure deuterium (left) and pure tritium (right).

sis. This appears to vary substantially from simulation to simulation. Hence the distribution does not seem to properly represent the extreme events. It was noted that the blob simulations suggested increased flux with decreased mass and that the model differences between these simulations and the blob simulation were the parallel parametrisation. In this regard, it would be beneficial to investigate the exact role of particularly the drift wave damping. Additionally, the number of simulation mixes was rather small, more simulations should be performed to get better statistics on the influence of the mixture on the fluxes. Lastly, the numerical setup could be tested with higher resolution to see if it is the problem was with e.g. the resolution or that the jump factor in the elliptic operator introduces too much numerical diffusion.

## 4.3 Section conclusion and Ideas for future studies

In this section two main themes were studied, namely seeded blob and turbulence simulations. For the seeded blobs, the first submitted paper with the model was discussed, along with the results of mixtures of deuterium and tritium in the propagation of blobs. Here it was found that overall, the more tritium there is in the blob the slower it evolves. In addition, the compositions of deuterium and double ionized helium in blobs were examined. Here it was found that, while the helium is much heavier than tritium and deuterium, the double charged nature of the helium counteracted the increased weight. This was seen in the radial blob velocity, where, the helium dominated blobs were only slightly slower than the deuterium dominated blob.

The turbulence studies were a first look into the influence of isotope mixtures on the transport in the edge/SOL using the MIHESEL model. Here it was found that the particle flux increased as the particle mass increased. This is in constrast to what is to be expected. Hence more studies are needed to cast light on what might be the cause of this discrepancy. Looking beyond this problem, there is still much more to explore with a multi species model.

The effect of isotopes on the LH transition has been studied experimentally[24], [97], [98]. It has been shown that the HESEL model, which is the basis of the MIHESEL model, can show a transition in confinement that resembles the LH-transition [99]. How mixtures affect this transition could provide new insights into the LH transition and is particularly interesting in regards to the upcoming DT campaign at the Joint European Torus (JET). Furthermore, EAST has shown that the extensive use of lithium has produces good confinement results and reduces e.g. ELMs [27]. This has also been numerically studied and shown that the inner profiles are raised when lithium is introduced [100]. This is similar to the results shown here, where a mismatch in the inner forcing mix and the outer minimum mix leads to raised profiles. Using the MIHESEL model, the effect of various isotopes on edge transport mitigators could be studied.

# Chapter 5

# Conclusion and Outlook

On the path to clean abundant and reliable energy, the fusion of light nuclei such as deuterium and tritium has been proposed as a viable solution to produce energy. This was discussed in Chapter 1 of the thesis, where the basic theory of the plasma confinement device known as a tokamak was given. In conjunction with this, the problems facing the fusion community in realising a workable fusion reactor was presented. In particular, the instabilities arising from fluctuations in the edge and the resulting turbulent transport were discussed. To overcome this problem, it first needs to be understood. In this regard, the influence of multiple ion species mixtures on turbulent transport has not been studied extensively in the existing literature. Therefore, the goal of this thesis has been threefold. First, to derive a multi-ion species model based on the drift fluid expansion approach. Second, to numerically implement the model and implement numerical methods to solve the equations, and third, to use this implementation to study first seeded density perturbations, known as blobs, and second fully developed turbulence in a setting emulating the outboard midplane of a tokamak.

## 5.1 Conclusions

In chapter 2, the multi-ion species drift fluid model, called the MIHESEL model, was derived. The starting point of the derivation was the Boltzmann single-particle equation. From this, equations for the evolution of the individual species fluid density, velocity and pressure were derived by taking moments of the Boltzmann equation. The equations obtained by purely taking moments of the Boltzmann equation contain quantities from the next higher-order moment. Hence a closure is needed. For this work, the Zhdanov closure was employed, which uses Grad's method, to close the equations.

While the closed set of equations for each plasma species contain all the necessary information, they are not practical for studying turbulent transport in the edge of the tokamak. To obtain equations well suited for this study, an approach known as drift fluid expansion was employed. From this, expressions for individual drift were obtained, which in turn could be used in the density and pressure equation. From these, a number of approximations, in the form of linearisations, were used to obtain equations that are numerically implementable. These final equations constitute the MIHESEL model.

In chapter 3, the numerical implementation of the MIHESEL model equations, derived in the previous chapter, was discussed. To solve the MIHESEL equations numerically it was found that a linear problem had to be solved first. This was due to coupling in the potential and pressure time derivatives resulting in a linear Helmholtz type system. This was cast in a symmetric positive definite form suitable for the conjugate gradient solver implemented in the numerical library FELTOR. In regards to the numerical library the numerical discretisation method, known as discontinuous Galerkin, was discussed. The MIHESEL equations contain non-linear diffusive terms and so to make the library capable of solving the MIHESEL equations in a reasonable time frame, a backward difference formula (BDF) fully implicit time integrator was implemented. This is an iterative procedure and since the MIHESEL equations are non-linear a solver was implemented. The non-linear solver is based on the Anderson Acceleration of the non-linear Richardson iteration. The combined time integrator and non-linear solver were tested using the method of manufactured solutions and found to give correct results and in particular that the solvers converge with the expected order.

In Chapter 4, the numerical implementation of the MIHESEL model was used to study seeded density perturbation, known as blobs, and turbulent transport. For the blobs, two kinds of mixtures were studied, a deuterium-tritium mix (presented in the first submitted paper) and a deuterium helium mix. For both cases, several mixture compositions were studied. The mixtures were split into two a background mix and perturbation mix and the influence of both mixes on the radial centre of mass propagation was investigated. For the DT simulations, it was found that more deuterium in general increases the maximum radial centre of mass velocity. In regards to the individual influence of the background mix and perturbation mix, it was found that the maximum velocity scaled stronger with the perturbation mix than the background. In the deuterium helium case, it was found that the influence of the increased mass was counteracted by the double charged nature of the helium. In particular, the maximum radial centre of mass velocity was found to be nearly equal, with helium being slightly lower. In this regard, it was expected, based on a velocity scaling, that the helium dominated blobs would have a factor 3/4 smaller maximum velocity compared to deuterium dominated. In respect to this, it was noted that the poloidal movement of the perturbations was more pronounced in the case of a deuterium dominated plasma especially if the deuterium was in the perturbation. This is a possible explanation for the helium velocity overshooting the scaling estimate. The second part of the chapter focused on turbulence simulations. Here mixtures of deuterium and tritium were investigated. To keep the simulations stable, a minimum background on the open field lines was enforced. To study the influence of the mixtures two parameters were varied, namely the mixture of the inner forcing region and the mixture of the outer minimum background. From the simulations, the temporal and poloidally averaged flux over the last closed flux surface was calculated. Here it was found that the flux increased as the amount of tritium also increased. This is in contrast to what is expected and suggests more studies are needed.

## 5.2 Outlook

In the derivation of the MIHESEL model from the Boltzmann equation, the Zhdanov closure was used to obtain a closed set of equations. For this closure it is assumed that $T_\alpha \approx T_\beta$. This could be expanded upon in the future to include arbitrary temperatures for the ions, which would be of use for studying, e.g., ICRH heating of multi-ion plasmas. To obtain the MIHESEL equations a number of approximations were employed to make the numerical implementation easier. As numerical libraries expand in capabilities, more problems are possible to solve. Hence it could be interesting to implement a full model with approximations. Lastly, the drift fluid expansion results in a small symmetry problem for the densities. I.e., a single ion plasma arbitrarily split into two (identical) ion species does not necessarily add exactly to what the single ion plasma would give. It was argued that the effect is minor, however, some more study into this would be beneficial.

In regards to the numerical methods, the non-linear Anderson acceleration solver was implemented for use in the implicit BDF method. In the future, other non-linear solvers could be implemented giving a wider range of tools to solve a wide range of problems. One such method could be a Newton-Krylov method which is known to be robust when solving non-linear equations. In regards to the linear solver, the current go-to method in the FELTOR library is the preconditioned conjugate gradient. However, for the MIHESEL implementation, it is often found the bottleneck is in the inversion of the linear problem of the coupled pressure and potential. Implementations of other efficient methods should also be considered.

Naturally, the issues discussed above in regards to transport should be investigated more closely to find the possible cause of the discrepancy that increased mass leads to increased flux. These studies should focus on the effect of the parallel parametrisations and the numerical setup. As a multi-ion model, the MIHESEL model can study many topics related to the dynamics of turbulence in the edge/SOL. One such topic could be the influence of the ion mixture on the LH transition where it has been found that the LH threshold decreases as the mixture mass increases. Moreover, the use of transport mitigators such as lithium in the SOL as it is used at EAST has experimentally shown great results in improving the confinement of the plasma. This too could be studied with a multi-ion species model. In connection with this, the MIHESEL model also includes source and sink terms, which can also be made to include ionisation of neutral particles. As such the injection of neutral lithium and subsequent ionisation could be studied with the model.

Naturally, it is expected that as the model is applied to different areas of study, more topics of interest will present itself. The continued use of the model will hopefully reveal areas where the MIHESEL model can be improved with new additions and features, all of which can contribute to further the understanding of the dynamics of the tokamak edge and scrape-off-layer.

# Bibliography

[1] S. R. James, R. W. Dennell, A. S. Gilbert, H. T. Lewis, J. A. J. Gowlett, T. F. Lynch, W. C. McGrew, C. R. Peters, G. G. Pope, A. B. Stahl, and S. R. James, “Hominid use of fire in the lower and middle pleistocene: A review of the evidence [and comments and replies]”, *Current Anthropology*, vol. 30, no. 1, pp. 1–26, Feb. 1989. DOI: `10.1086/203705`. [Online]. Available: `https://doi.org/10.1086/203705`.

[2] *Fusion Physics*. International Atomic Energy Agency, Dec. 2012, ISBN: 9201304102. [Online]. Available: `https://www.xarg.org/ref/a/9201304102/`.

[3] C. W. Kamienski, D. P. McDonald, M. W. Stark, and J. R. Papcun, “Lithium and Lithium Compounds”, en, in *Kirk-Othmer Encyclopedia of Chemical Technology*, American Cancer Society, 2004, ISBN: 978-0-471-23896-6. DOI: `10.1002/0471238961.1209200811011309.a01.pub2`. [Online]. Available: `https://onlinelibrary.wiley.com/doi/abs/10.1002/0471238961.1209200811011309.a01.pub2` (visited on 02/05/2020).

[4] *Fuelling the Fusion Reaction*, en. [Online]. Available: `http://www.iter.org/sci/fusionfuels` (visited on 02/05/2020).

[5] J. Wesson and D. J. Campbell, *Tokamaks*, 4th ed, ser. Oxford science publications 149. Oxford ; New York: Oxford University Press, 2011, OCLC: ocn751505944, ISBN: 978-0-19-959223-4.

[6] R. Arnoux, *Which was the first ’tokamak’—or was it ’tokomag’?*, en, 2008. [Online]. Available: `http://www.iter.org/newsline/55/1194` (visited on 02/05/2020).

[7] *Milestones around the world*, en. [Online]. Available: `http://www.iter.org/sci/beyonditer` (visited on 02/05/2020).

[8] EUROfusion, *Tokamak principle*, en, 2011. [Online]. Available: `https://www.euro-fusion.org/news/detail/detail/News/tokamak-principle/` (visited on 02/05/2020).

[9] D. o. P. U. o. York, Heslington, York, Y. 5dd, and U. T. w. |. F. fax +441904 322214, *Advancing our understanding of low-temperature plasma physics for optimising future fusion energy reactors*, en, 2016. [Online]. Available: `https://www.york.ac.uk/physics/news/departmentalnews/optimising-future-fusion-energy-reactors/` (visited on 02/05/2020).

[10] G. Manfredi, *How to model quantum plasmas*, Dec. 2005. DOI: `10.1090/fic/046/10`. [Online]. Available: `https://doi.org/10.1090/fic/046/10`.

[11] A. Dinklage, T. Klinger, G. Marx, L. Schweikhard, R. Beig, W. Beiglböck, W. Domcke, B.-G. Englert, U. Frisch, P. Hänggi, G. Hasinger, K. Hepp, W. Hillebrandt, D. Imboden, R. L. Jaffe, R. Lipowsky, H. v. Löhneysen, I. Ojima, D. Sornette, S. Theisen, W. Weise, J. Wess, and J. Zittartz, Eds., *Plasma Physics: Confinement, Transport and Collective Effects*, en, ser. Lecture Notes in Physics. Berlin, Heidelberg: Springer Berlin Heidelberg, 2005, vol. 670, ISBN: 978-3-540-25274-0 978-3-540-31521-6. DOI: `10.1007/b103882`. [Online]. Available: `http://link.springer.com/10.1007/b103882` (visited on 01/23/2020).

[12] A. J. Wootton, B. A. Carreras, H. Matsumoto, K. McGuire, W. A. Peebles, C. P. Ritz, P. W. Terry, and S. J. Zweben, “Fluctuations and anomalous transport in tokamaks”, *Physics of Fluids B: Plasma Physics*, vol. 2, no. 12, pp. 2879–2903, Dec. 1990, ISSN: 0899-8221. DOI: `10.1063/1.859358`. [Online]. Available: `https://aip.scitation.org/doi/10.1063/1.859358` (visited on 01/08/2020).

[13] S. J. Zweben, J. A. Boedo, O Grulke, C Hidalgo, B LaBombard, R. J. Maqueda, P Scarin, and J. L. Terry, “Edge turbulence measurements in toroidal fusion devices”, *Plasma Physics and Controlled Fusion*, vol. 49, no. 7, S1–S23, Jun. 2007. DOI: `10.1088/0741-3335/49/7/s01`. [Online]. Available: `https://doi.org/10.1088%2F0741-3335%2F49%2F7%2Fs01`.

[14] V. Naulin, “Turbulent transport and the plasma edge”, *Journal of Nuclear Materials*, vol. 363-365, pp. 24–31, Jun. 2007. DOI: `10.1016/j.jnucmat.2006.12.058`. [Online]. Available: `https://doi.org/10.1016/j.jnucmat.2006.12.058`.

[15] B. D. Scott, “Tokamak edge turbulence: Background theory and computation”, *Plasma Physics and Controlled Fusion*, vol. 49, no. 7, S25–S41, Jul. 2007, ISSN: 0741-3335, 1361-6587. DOI: `10.1088/0741-3335/49/7/S02`. [Online]. Available: `http://stacks.iop.org/0741-3335/49/i=7/a=S02?key=crossref.e5c26cd36e1707fba46e210fb2b6d27c` (visited on 01/24/2020).

[16] O. E. Garcia, V. Naulin, A. H. Nielsen, and J. J. Rasmussen, “Turbulence and intermittent transport at the boundary of magnetized plasmas”, *Physics of Plasmas*, vol. 12, no. 6, p. 062 309, Jun. 2005. DOI: `10.1063/1.1925617`. [Online]. Available: `https://doi.org/10.1063/1.1925617`.

[17] J. Madsen, V. Naulin, A. H. Nielsen, and J. J. Rasmussen, “Collisional transport across the magnetic field in drift-fluid models”, *Physics of Plasmas*, vol. 23, no. 3, p. 032 306, Mar. 2016, ISSN: 1070-664X. DOI: `10.1063/1.4943199`. [Online]. Available: `https://aip.scitation.org/doi/10.1063/1.4943199` (visited on 04/29/2019).

[18] P Ricci, F. D. Halpern, S Jolliet, J Loizu, A Mosetto, A Fasoli, I Furno, and C Theiler, “Simulation of plasma turbulence in scrape-off layer conditions: The GBS code, simulation results and code validation”, *Plasma Physics and Controlled Fusion*, vol. 54, no. 12, p. 124 047, Nov. 2012. DOI: `10.1088/0741-3335/54/12/124047`. [Online]. Available: `https://doi.org/10.1088%2F0741-3335%2F54%2F12%2F124047`.

[19] L. Easy, F. Militello, J. Omotani, B. Dudson, E. Havlíčková, P. Tamain, V. Naulin, and A. H. Nielsen, “Three dimensional simulations of plasma filaments in the scrape off layer: A comparison with models of reduced dimensionality”, *Physics of Plasmas*, vol. 21, no. 12, p. 122 515, Dec. 2014. DOI: `10.1063/1.4904207`. [Online]. Available: `https://doi.org/10.1063/1.4904207`.

[20] P. Tamain, H. Bufferand, G. Ciraolo, C. Colin, P. Ghendrih, F. Schwander, and E. Serre, “3d properties of edge turbulent transport in full-torus simulations and their impact on poloidal asymmetries”, *Contributions to Plasma Physics*, vol. 54, no. 4-6, pp. 555–559, Jun. 2014. DOI: `10.1002/ctpp.201410017`. [Online]. Available: `https://doi.org/10.1002/ctpp.201410017`.

[21] O. H. H. Meyer and A. Kendl, “Isotope effect on gyro-fluid edge turbulence and zonal flows”, *Plasma Physics and Controlled Fusion*, vol. 58, no. 11, p. 115 008, Sep. 2016, ISSN: 0741-3335. DOI: `10.1088/0741-3335/58/11/115008`. [Online]. Available: `https://doi.org/10.1088%2F0741-3335%2F58%2F11%2F115008` (visited on 04/29/2019).

[22] ——, “Isotope effect on blob-statistics in gyrofluid simulations of scrape-off layer turbulence”, *Nuclear Fusion*, vol. 57, no. 12, p. 126 066, Nov. 2017, ISSN: 0029-5515. DOI: `10.1088/1741-4326/aa8e33`. [Online]. Available: `https://doi.org/10.1088%2F1741-4326%2Faa8e33` (visited on 04/29/2019).

[23] ——, “Isotope effect on filament dynamics in fusion edge plasmas”, *Plasma Physics and Controlled Fusion*, vol. 59, no. 6, p. 065 001, Apr. 2017, ISSN: 0741-3335. DOI: `10.1088/1361-6587/aa6947`. [Online]. Available: `https://doi.org/10.1088%2F1361-6587%2Faa6947` (visited on 04/29/2019).

[24] C. F. Maggi, H Weisen, J. C. Hillesheim, A Chankin, E Delabie, L Horvath, F Auriemma, I. S. Carvalho, G Corrigan, J Flanagan, L Garzotti, D Keeling, D King, E Lerche, R Lorenzini, M Maslov, S Menmuir, S Saarelma, A. C. C. Sips, E. R. Solano, E Belonohy, F. J. Casson, C Challis, C Giroud, V Parail, C Silva, and M. V. and, “Isotope effects on l-h threshold and confinement in tokamak plasmas”, *Plasma Physics and Controlled Fusion*, vol. 60, no. 1, p. 014 045, Nov. 2017. DOI: `10.1088/1361-6587/aa9901`. [Online]. Available: `https://doi.org/10.1088%2F1361-6587%2Faa9901`.

[25] M. McRae, *China’s Nuclear Fusion Machine Just Smashed Temperature Records by Getting 6 Times Hotter Than The Sun*, en-gb, 2018. [Online]. Available: `https://www.sciencealert.com/china-s-artificial-sun-has-officially-become-hot-enough-for-nuclear-fusion` (visited on 02/05/2020).

[26] C. A. of Sciences, *China’s ’artificial sun’ sets world record with 100 second steady-state high performance plasma*, en-us, 2017. [Online]. Available: `https://phys.org/news/2017-07-china-artificial-sun-world-steady-state.html` (visited on 02/05/2020).

[27] R. Maingi, J. Hu, Z. Sun, K. Tritz, G. Zuo, W. Xu, M. Huang, X. Meng, J. Canik, A. Diallo, R. Lunsford, D. Mansfield, T. Osborne, X. Gong, Y. Wang, and Y. L. and, “ELM elimination with li powder injection in EAST discharges using the tungsten upper divertor”, *Nuclear Fusion*, vol. 58, no. 2, p. 024 003, Jan. 2018. DOI: `10.1088/1741-4326/aa9e3f`. [Online]. Available: `https://doi.org/10.1088/1741-4326/aa9e3f`.

[28] M. Wiesenberger, L. Einkemmer, M. Held, A. Gutierrez-Milla, X. Sáez, and R. Iakymchuk, “Reproducibility, accuracy and performance of the Feltor code and library on parallel computer architectures”, *Computer Physics Communications*, vol. 238, pp. 145–156, May 2019,

ISSN: 0010-4655. DOI: `10.1016/j.cpc.2018.12.006`. [Online]. Available: `http://www.sciencedirect.com/science/article/pii/S0010465518304223` (visited on 04/29/2019).

[29] D. J. Griffiths, *Introduction to electrodynamics; 4th ed.* Boston, MA: Pearson, 2013, Re-published by Cambridge University Press in 2017. DOI: `1108420419`. [Online]. Available: `https://cds.cern.ch/record/1492149`.

[30] M. Magnussen, "Global numerical modeling of magnetized plasma in a linear device", English, PhD thesis, 2017.

[31] C. K. Birdsall and A. B. Langdon, *Plasma physics via computer simulation*, eng, ser. Series in plasma physics. New York [u.a.] Taylor & Francis, 2005, OCLC: 255024486, ISBN: 978-0-7503-1025-3.

[32] D. Tong, *Kinetic Theory.* Cambridge, UK: University of Cambridge Graduate Course, 2012. [Online]. Available: `https://www.damtp.cam.ac.uk/user/tong/kinetic.html` (visited on 01/23/2020).

[33] R. Balescu, *Transport processes in plasmas.* Amsterdam ; New York : New York, NY, USA: North-Holland ; Sole distributors for the USA and Canada, Elsevier Science Pub. Co, 1988, ISBN: 978-0-444-87093-3 978-0-444-87091-9 978-0-444-87092-6.

[34] V. M. Zhdanov, "Transport processes in multicomponent plasma", *Plasma Physics and Controlled Fusion*, vol. 44, no. 10, pp. 2283–2283, Sep. 2002. DOI: `10.1088/0741-3335/44/10/701`. [Online]. Available: `https://doi.org/10.1088%2F0741-3335%2F44%2F10%2F701`.

[35] R. Fitzpatrick, *Plasma Physics: An Introduction*, en. [Online]. Available: `https://www.crcpress.com/Plasma-Physics-An-Introduction/Fitzpatrick/p/book/9781466594265` (visited on 01/23/2020).

[36] R. D. Hazeltine, "Coulomb collision operator", *Tech. Rep., University of Texas*, p. 27, 2006. [Online]. Available: `http://w3fusion.ph.utexas.edu/ifs/ifsreports/1140_Hazeltine.pdf`.

[37] S. I. Braginskii, "Transport Processes in a Plasma", *Reviews of Plasma Physics*, vol. 1, p. 205, 1965. [Online]. Available: `http://adsabs.harvard.edu/abs/1965RvPP....1..205B` (visited on 04/29/2019).

[38] F. L. Hinton, "Collisional transport in plasma", *Basic plasma physics. 1*, 1983. [Online]. Available: `http://inis.iaea.org/Search/search.aspx?orig_q=RN:15068889` (visited on 04/29/2019).

[39] W Fundamenski and O. E. Garcia, “Comparison of Coulomb Collision Rates in the Plasma Physics and Magnetically Confined Fusion Literature”, *EFDA-JET-R.*, p. 17, 2007.

[40] R. D. Hazeltine and J. D. Meiss, *Plasma confinement*, eng, ser. Dover Books on Physics. Mineola, NY: Dover, 2003, ISBN: 978-0-486-15103-8 978-0-486-43242-7.

[41] S. Chapman and T. G. Cowling, “The mathematical theory of non-uniform gases. an account of the kinetic theory of viscosity, thermal conduction, and diffusion in gases. by sydney chapman and t. g. cowling. 2nd edn., pp. ix, 431. 60s. 1952. (cambridge university press)”, *The Mathematical Gazette*, vol. 38, no. 323, 63–64, 1954. DOI: `10.2307/3609795`.

[42] H. Grad, “On the kinetic theory of rarefied gases”, *Communications on Pure and Applied Mathematics*, vol. 2, no. 4, pp. 331–407, 1949. DOI: `10.1002/cpa.3160020403`. [Online]. Available: `https://app.dimensions.ai/details/publication/pub.1049725519`.

[43] D. Pfefferlé, E. Hirvijoki, and M. Lingam, “Exact collisional moments for plasma fluid theories”, en, *Physics of Plasmas*, vol. 24, no. 4, p. 042 118, Apr. 2017, ISSN: 1070-664X, 1089-7674. DOI: `10.1063/1.4979992`. [Online]. Available: `http://aip.scitation.org/doi/10.1063/1.4979992` (visited on 01/24/2020).

[44] P. Porytsky, I. Krivtsun, V. Demchenko, U. Reisgen, O. Mokrov, A. Zabirov, S. Gorchakov, A. Timofeev, and D. Uhrlandt, “Transport properties of multicomponent thermal plasmas: Grad method versus Chapman-Enskog method”, en, *Physics of Plasmas*, vol. 20, no. 2, p. 023 504, Feb. 2013, ISSN: 1070-664X, 1089-7674. DOI: `10.1063/1.4790661`. [Online]. Available: `http://aip.scitation.org/doi/10.1063/1.4790661` (visited on 01/24/2020).

[45] S. P. Hirshman and D. J. Sigmar, “Neoclassical transport of impurities in tokamak plasmas”, *Nuclear Fusion*, vol. 21, no. 9, pp. 1079–1201, Sep. 1981, ISSN: 0029-5515. DOI: `10.1088/0029-5515/21/9/003`. (visited on 04/29/2019).

[46] H. Bufferand, P. Tamain, S. Baschetti, J. Bucalossi, G. Ciraolo, N. Fedorczak, P. Ghendrih, F. Nespoli, F. Schwander, E. Serre, and Y. Marandet, “Three-dimensional modelling of edge multi-component plasma taking into account realistic wall geometry”, *Nuclear Materials and Energy*, vol. 18, pp. 82–86, Jan. 2019, ISSN: 2352-1791. DOI: `10.1016/j.nme.2018.11.025`. [Online]. Available: `http://www.`

`sciencedirect.com/science/article/pii/S2352179118302035` (visited on 04/29/2019).

[47] Y. Igitkhanov, *Modelling of Multi-Component Plasma for TOKES (KIT Scientific Reports ; 7564)*, 2011. DOI: `10.5445/KSP/1000022049`. [Online]. Available: `https://publikationen.bibliothek.kit.edu/1000022049` (visited on 04/29/2019).

[48] F. I. Parra, "Braginskii fluid equations", en, p. 19, [Online]. Available: `http://www-thphys.physics.ox.ac.uk/people/FelixParra/CollisionalPlasmaPhysics/notes/` (visited on 01/23/2020).

[49] D. D. Schnack, *Lectures in magnetohydrodynamics: with an appendix on extended MHD*, ser. Lecture notes in physics 780. Dordrecht ; New York: Springer, 2009, OCLC: ocn310400946, ISBN: 978-3-642-00687-6 978-3-642-00688-3.

[50] A. Thrysøe, Personal conversation, Dec. 2019.

[51] A. Thrysøe, M. Løiten, J. Madsen, V. Naulin, A. Nielsen, and J. Rasmussen, "Plasma particle sources due to interactions with neutrals in a turbulent scrape-off layer of a toroidally confined plasma", English, *Physics of Plasmas*, vol. 25, no. 3, 2018, ISSN: 1070-664X. DOI: `10.1063/1.5019662`.

[52] J. Madsen, O. E. Garcia, J. Stærk Larsen, V. Naulin, A. H. Nielsen, and J. J. Rasmussen, "The influence of finite Larmor radius effects on the radial interchange motions of plasma filaments", *Physics of Plasmas*, vol. 18, no. 11, p. 112 504, Nov. 2011, ISSN: 1070-664X, 1089-7674. DOI: `10.1063/1.3658033`. [Online]. Available: `http://aip.scitation.org/doi/10.1063/1.3658033` (visited on 06/25/2019).

[53] F. L. Hinton, "Amplitude Limitation of a Collisional Drift Wave Instability", en, *Physics of Fluids*, vol. 14, no. 1, p. 116, 1971, ISSN: 00319171. DOI: `10.1063/1.1693260`. [Online]. Available: `https://aip.scitation.org/doi/10.1063/1.1693260` (visited on 01/23/2020).

[54] J. Olsen, "Studies of coherent lamentary structures in magnetically conned plasmas", English, PhD thesis, 2018.

[55] O. E. Garcia, "Collective motions in non-uniformly magnetized plasmas", *European Journal of Physics*, vol. 24, no. 4, pp. 331–339, May 2003. DOI: `10.1088/0143-0807/24/4/351`. [Online]. Available: `https://doi.org/10.1088%2F0143-0807%2F24%2F4%2F351`.

[56] A. N. Simakov and P. J. Catto, “Drift-ordered fluid equations for field-aligned modes in low-β collisional plasma with equilibrium pressure pedestals”, en, *Physics of Plasmas*, vol. 10, no. 12, pp. 4744–4757, Dec. 2003, ISSN: 1070-664X, 1089-7674. DOI: `10.1063/1.1623492`. [Online]. Available: `http://aip.scitation.org/doi/10.1063/1.1623492` (visited on 01/23/2020).

[57] E. V. Belova, “Nonlinear gyroviscous force in a collisionless plasma”, *Physics of Plasmas*, vol. 8, no. 9, pp. 3936–3944, Aug. 2001, ISSN: 1070-664X. DOI: `10.1063/1.1389093`. [Online]. Available: `https://aip.scitation.org/doi/10.1063/1.1389093` (visited on 04/29/2019).

[58] A. Smolyakov, “Gyroviscous forces in a collisionless plasma with temperature gradients”, *Canadian Journal of Physics*, vol. 76, no. 4, pp. 321–331, 1998, ISSN: 12086045, 00084204. DOI: `10.1139/cjp-76-4-321`. [Online]. Available: `http://www.nrc.ca/cgi-bin/cisti/journals/rp/rp2_abst_e?cjp_p98-012_76_ns_nf_cjp76-98` (visited on 01/23/2020).

[59] Z. Chang and J. D. Callen, “Generalized gyroviscous force and its effect on the momentum balance equation”, en, *Physics of Fluids B: Plasma Physics*, vol. 4, no. 7, pp. 1766–1771, Mar. 1992, ISSN: 0899-8221. DOI: `10.1063/1.860032`. [Online]. Available: `http://aip.scitation.org/doi/10.1063/1.860032` (visited on 01/24/2020).

[60] S. I. Krasheninnikov, D. A. D’ippolito, and J. R. Myra, “Recent theoretical progress in understanding coherent structures in edge and SOL turbulence”, en, *Journal of Plasma Physics*, vol. 74, no. 5, pp. 679–717, Oct. 2008, ISSN: 1469-7807, 0022-3778. DOI: `10.1017/S0022377807006940`. [Online]. Available: `https://www.cambridge.org/core/journals/journal-of-plasma-physics/article/recent-theoretical-progress-in-understanding-coherent-structures-in-edge-and-sol-turbulence/8D63C9858F71611B114B7516FC4CF8EC` (visited on 11/27/2019).

[61] W Fundamenski, O. Garcia, V Naulin, R. Pitts, A. Nielsen, J. J. Rasmussen, J Horacek, J. Graves, and J. E. contributors, “Dissipative processes in interchange driven scrape-off layer turbulence”, *Nuclear Fusion*, vol. 47, no. 5, pp. 417–433, Apr. 2007. DOI: `10.1088/0029-5515/47/5/006`. [Online]. Available: `https://doi.org/10.1088%2F0029-5515%2F47%2F5%2F006`.

[62] A. H. Nielsen, J. J. Rasmussen, J Madsen, G. S. Xu, V Naulin, J. M. B. Olsen, M Løiten, S. K. Hansen, N Yan, L Tophøj, and B. N. Wan, “Numerical simulations of blobs with ion dynamics”, *Plasma Physics*

*and Controlled Fusion*, vol. 59, no. 2, p. 025 012, Jan. 2017. DOI: `10.1088/1361-6587/59/2/025012`. [Online]. Available: `https://doi.org/10.1088%2F1361-6587%2F59%2F2%2F025012`.

[63] O. E. Garcia, V. Naulin, A. H. Nielsen, and J. J. Rasmussen, “Computations of Intermittent Transport in Scrape-Off Layer Plasmas”, en, *Physical Review Letters*, vol. 92, no. 16, p. 165 003, Apr. 2004, ISSN: 0031-9007, 1079-7114. DOI: `10.1103/PhysRevLett.92.165003`. [Online]. Available: `https://link.aps.org/doi/10.1103/PhysRevLett.92.165003` (visited on 01/23/2020).

[64] D Moulton, P. Ghendrih, W Fundamenski, G Manfredi, and D Tskhakaya, “Quasineutral plasma expansion into infinite vacuum as a model for parallel ELM transport”, *Plasma Physics and Controlled Fusion*, vol. 55, no. 8, p. 085 003, May 2013. DOI: `10.1088/0741-3335/55/8/085003`. [Online]. Available: `https://doi.org/10.1088%2F0741-3335%2F55%2F8%2F085003`.

[65] J. R. Myra, D. A. D’Ippolito, and D. A. Russell, “Turbulent transport regimes and the scrape-off layer heat flux width”, en, *Physics of Plasmas*, vol. 22, no. 4, p. 042 516, Apr. 2015, ISSN: 1070-664X, 1089-7674. DOI: `10.1063/1.4919255`. [Online]. Available: `http://aip.scitation.org/doi/10.1063/1.4919255` (visited on 01/23/2020).

[66] L. Spitzer and R. Härm, “Transport Phenomena in a Completely Ionized Gas”, en, *Physical Review*, vol. 89, no. 5, pp. 977–981, Mar. 1953, ISSN: 0031-899X. DOI: `10.1103/PhysRev.89.977`. [Online]. Available: `https://link.aps.org/doi/10.1103/PhysRev.89.977` (visited on 01/23/2020).

[67] J. Gath and M. Wiesenberger, “Consistency in drift-ordered fluid equations”, *Physics of Plasmas*, vol. 26, no. 3, p. 032 304, Mar. 2019, ISSN: 1070-664X, 1089-7674. DOI: `10.1063/1.5081777`. [Online]. Available: `http://aip.scitation.org/doi/10.1063/1.5081777` (visited on 04/30/2019).

[68] E. Hirvijoki, M. Lingam, D. Pfefferlé, L. Comisso, J. Candy, and A. Bhattacharjee, “Fluid moments of the nonlinear Landau collision operator”, en, *Physics of Plasmas*, vol. 23, no. 8, p. 080 701, Aug. 2016, ISSN: 1070-664X, 1089-7674. DOI: `10.1063/1.4960669`. [Online]. Available: `http://aip.scitation.org/doi/10.1063/1.4960669` (visited on 01/24/2020).

[69] J.-Y. Ji and E. D. Held, “Full Coulomb collision operator in the moment expansion”, en, *Physics of Plasmas*, vol. 16, no. 10, p. 102 108, Oct. 2009, ISSN: 1070-664X, 1089-7674. DOI: `10.1063/1.3234253`. [Online]. Available: `http://aip.scitation.org/doi/10.1063/1.3234253` (visited on 01/24/2020).

[70] M. K. Srivastava, B. K. Sinha, and S. V. Lawande, “Ion front and ablation in a freely expanding two-ion, two-temperature, noncollisional plasma”, en, *Physics of Fluids*, vol. 31, no. 2, p. 394, 1988, ISSN: 00319171. DOI: `10.1063/1.866820`. [Online]. Available: `https://aip.scitation.org/doi/10.1063/1.866820` (visited on 01/24/2020).

[71] C. Sack and H. Schamel, “Plasma expansion into vacuum — A hydrodynamic approach”, en, *Physics Reports*, vol. 156, no. 6, pp. 311–395, Dec. 1987, ISSN: 03701573. DOI: `10.1016/0370-1573(87)90039-1`. [Online]. Available: `https://linkinghub.elsevier.com/retrieve/pii/0370157387900391` (visited on 01/24/2020).

[72] I. S. Elkamash and I. Kourakis, “Multispecies plasma expansion into vacuum: The role of secondary ions and suprathermal electrons”, en, *Physical Review E*, vol. 94, no. 5, p. 053 202, Nov. 2016, ISSN: 2470-0045, 2470-0053. DOI: `10.1103/PhysRevE.94.053202`. [Online]. Available: `https://link.aps.org/doi/10.1103/PhysRevE.94.053202` (visited on 01/24/2020).

[73] Y. Saad, *Iterative Methods for Sparse Linear Systems.* Society for Industrial and Applied Mathematics, Jan. 2003. DOI: `10.1137/1.9780898718003`. [Online]. Available: `https://doi.org/10.1137/1.9780898718003`.

[74] M. Wiesenberger, “Gyrofluid computations of filament dynamics in tokamak scrape-off layers”, Available from INIS: http://inis.iaea.org/search/search.aspx?or Available from INIS in electronic form. Also available from Library of the University of Innsbruck, Innrain 50, 6020 Innsbruck (AT) and available from http://permalink.obvsg.at/AC11359321, PhD thesis, 2014. [Online]. Available: `http://inis.iaea.org/search/search.aspx?orig_q=RN:47078906`.

[75] B. Cockburn and C.-W. Shu, “Runge–kutta discontinuous galerkin methods for convection-dominated problems”, *Journal of Scientific Computing*, vol. 16, no. 3, pp. 173–261, Sep. 2001, ISSN: 1573-7691. DOI: `10.1023/A:1012873910884`. [Online]. Available: `https://doi.org/10.1023/A:1012873910884`.

[76] C.-W. Shu, “Discontinuous galerkin methods: General approach and stability”, *Numerical Solutions of Partial Differential Equations*, Jan. 2009.

[77] D. A. Kopriva, *Implementing Spectral Methods for Partial Differential Equations*. Springer Netherlands, 2009. DOI: `10.1007/978-90-481-2261-5`. [Online]. Available: `https://doi.org/10.1007/978-90-481-2261-5`.

[78] B. Shizgal, *Spectral Methods in Chemistry and Physics*. Springer Netherlands, 2015. DOI: `10.1007/978-94-017-9454-1`. [Online]. Available: `https://doi.org/10.1007/978-94-017-9454-1`.

[79] R. J. LeVeque, *Finite Difference Methods for Ordinary and Partial Differential Equations*. Society for Industrial and Applied Mathematics, Jan. 2007. DOI: `10.1137/1.9780898717839`. [Online]. Available: `https://doi.org/10.1137/1.9780898717839`.

[80] U. M. Ascher and L. R. Petzold, *Computer Methods for Ordinary Differential Equations and Differential-Algebraic Equations*. SIAM: Society for Industrial and Applied Mathematics, 1998, ISBN: 0898714125. [Online]. Available: `https://www.amazon.com/Computer-Ordinary-Differential-Equations-Differential-Algebraic/dp/0898714125?SubscriptionId=AKIAIOBINVZYXZQZ2U3A&tag=chimbori05-20&linkCode=xm2&camp=2025&creative=165953&creativeASIN=0898714125`.

[81] C. T. Kelley, *Iterative Methods for Linear and Nonlinear Equations*. Society for Industrial and Applied Mathematics, Jan. 1995. DOI: `10.1137/1.9781611970944`. [Online]. Available: `https://doi.org/10.1137/1.9781611970944`.

[82] P. R. Brune, M. G. Knepley, B. F. Smith, and X. Tu, “Composing scalable nonlinear algebraic solvers”, *SIAM Review*, vol. 57, no. 4, pp. 535–565, Jan. 2015. DOI: `10.1137/130936725`. [Online]. Available: `https://doi.org/10.1137/130936725`.

[83] D. G. Anderson, “Iterative procedures for nonlinear integral equations”, *Journal of the ACM*, vol. 12, no. 4, pp. 547–560, Oct. 1965. DOI: `10.1145/321296.321305`. [Online]. Available: `https://doi.org/10.1145/321296.321305`.

[84] H. Walker, “Anderson acceleration: Algorithms and implementations”, *Worcester Polytechnic Institute Mathematical Sciences Department Research Report MS-6-15-50*, Jun. 2011. [Online]. Available: `http://users.wpi.edu/~walker/Papers/anderson_accn_algs_imps.pdf` (visited on 01/27/2020).

[85] N. C. Henderson and R. Varadhan, "Damped anderson acceleration with restarts and monotonicity control for accelerating EM and EM-like algorithms", *Journal of Computational and Graphical Statistics*, vol. 28, no. 4, pp. 834–846, May 2019. DOI: `10.1080/10618600.2019.1594835`. [Online]. Available: `https://doi.org/10.1080/10618600.2019.1594835`.

[86] H. F. WALKER and P. NI, "Anderson acceleration for fixed-point iterations", *SIAM Journal on Numerical Analysis*, vol. 49, no. 3/4, pp. 1715–1735, 2011, ISSN: 00361429. DOI: `10.2307/23074353`. [Online]. Available: `http://www.jstor.org/stable/23074353`.

[87] H. ren Fang and Y. Saad, "Two classes of multisecant methods for nonlinear acceleration", *Numerical Linear Algebra with Applications*, vol. 16, no. 3, pp. 197–221, Mar. 2009. DOI: `10.1002/nla.617`. [Online]. Available: `https://doi.org/10.1002/nla.617`.

[88] B. Dudson, M. Umansky, X. Xu, P. Snyder, and H. Wilson, "BOUT++: A framework for parallel plasma fluid simulations", *Computer Physics Communications*, vol. 180, no. 9, pp. 1467–1480, Sep. 2009. DOI: `10.1016/j.cpc.2009.03.008`. [Online]. Available: `https://doi.org/10.1016/j.cpc.2009.03.008`.

[89] D. Knoll and D. Keyes, "Jacobian-free newton-krylov methods: A survey of approaches and applications", *Journal of Computational Physics*, vol. 193, pp. 357–397, Jan. 2004. DOI: `10.1016/j.jcp.2003.08.010`.

[90] A. H. Baker, E. R. Jessup, and T. Manteuffel, "A technique for accelerating the convergence of restarted GMRES", *SIAM Journal on Matrix Analysis and Applications*, vol. 26, no. 4, pp. 962–984, Jan. 2005. DOI: `10.1137/s0895479803422014`. [Online]. Available: `https://doi.org/10.1137/s0895479803422014`.

[91] G. L. G. Sleijpen, "BICGSTAB ( L ) FOR LINEAR EQUATIONS INVOLVING UNSYMMETRIC MATRICES WITH COMPLEX", 1993.

[92] J. Olsen, J. Madsen, A. H. Nielsen, J. J. Rasmussen, and V. Naulin, "Temperature dynamics and velocity scaling laws for interchange driven, warm ion plasma filaments", *Plasma Physics and Controlled Fusion*, vol. 58, no. 4, p. 044011, Feb. 2016, ISSN: 0741-3335. DOI: `10.1088/0741-3335/58/4/044011`. [Online]. Available: `https://doi.org/10.1088%2F0741-3335%2F58%2F4%2F044011` (visited on 10/23/2019).

[93] M. Held, M. Wiesenberger, J. Madsen, and A. Kendl, “The influence of temperature dynamics and dynamic finite ion larmor radius effects on seeded high amplitude plasma blobs”, *Nuclear Fusion*, vol. 56, no. 12, p. 126 005, Sep. 2016. DOI: `10.1088/0029-5515/56/12/126005`. [Online]. Available: `https://doi.org/10.1088%2F0029-5515%2F56%2F12%2F126005`.

[94] H. Hasegawa and S. Ishiguro, “Study of self-consistent particle flows in a plasma blob with particle-in-cell simulations”, en, *Physics of Plasmas*, vol. 22, no. 10, p. 102 113, Oct. 2015, ISSN: 1070-664X, 1089-7674. DOI: `10.1063/1.4933359`. [Online]. Available: `http://aip.scitation.org/doi/10.1063/1.4933359` (visited on 01/24/2020).

[95] P. W. Gingell, S. C. Chapman, R. O. Dendy, and C. S. Brady, “Transport and evolution of ion gyro-scale plasma blobs in perpendicular magnetic fields”, *Plasma Physics and Controlled Fusion*, vol. 54, no. 6, p. 065 005, May 2012. DOI: `10.1088/0741-3335/54/6/065005`. [Online]. Available: `https://doi.org/10.1088%2F0741-3335%2F54%2F6%2F065005`.

[96] M. Wiesenberger, J. Madsen, and A. Kendl, “Radial convection of finite ion temperature, high amplitude plasma blobs”, en, *Physics of Plasmas*, vol. 21, no. 9, p. 092 301, Sep. 2014, ISSN: 1070-664X, 1089-7674. DOI: `10.1063/1.4894220`. [Online]. Available: `http://aip.scitation.org/doi/10.1063/1.4894220` (visited on 01/24/2020).

[97] M Bessenrodt-Weberpals, F Wagner, O Gehre, L Giannone, J. Hofmann, A Kallenbach, K McCormick, V Mertens, H. Murmann, F Ryter, B. Scott, G Siller, F. Soldner, A Stabler, K.-H Steuer, U Stroth, N Tsois, H Verbeek, and H Zoohm, “The isotope effect in ASDEX”, *Nuclear Fusion*, vol. 33, no. 8, pp. 1205–1238, Aug. 1993. DOI: `10.1088/0029-5515/33/8/i09`. [Online]. Available: `https://doi.org/10.1088%2F0029-5515%2F33%2F8%2Fi09`.

[98] N. Bonanomi, C. Angioni, P. Crandall, A. D. Siena, C. Maggi, P. Schneider, the ASDEX Upgrade Team, the EUROFusion MST1 Team, and the JET Contributors, “Effect of the isotope mass on the turbulent transport at the edge of l-mode plasmas in ASDEX upgrade and JET-ILW”, *Nuclear Fusion*, vol. 59, no. 12, p. 126 025, Oct. 2019. DOI: `10.1088/1741-4326/ab3ecc`. [Online]. Available: `https://doi.org/10.1088%2F1741-4326%2Fab3ecc`.

[99] J. J. Rasmussen, A. H. Nielsen, J Madsen, V Naulin, and G. S. Xu, “Numerical modeling of the transition from low to high confinement

in magnetically confined plasma", *Plasma Physics and Controlled Fusion*, vol. 58, no. 1, p. 014031, Jan. 2016. DOI: `10.1088/0741-3335/58/1/014031`. [Online]. Available: `https://doi.org/10.1088/0741-3335/58/1/014031`.

[100] N. Li, J. Sun, Z. Wang, X. Xu, Z. Sun, L. Wang, J. Hu, and D. Wang, "Numerical investigation on lithium transport in the edge plasma of EAST real-time- Li-injection experiments in the frame of BOUT++", en, *Nuclear Materials and Energy*, vol. 12, pp. 119–123, Aug. 2017, ISSN: 23521791. DOI: `10.1016/j.nme.2016.12.009`. [Online]. Available: `https://linkinghub.elsevier.com/retrieve/pii/S2352179116301363` (visited on 01/24/2020).